UNIVERSIDADE
BEIRA INTERIOR

Numerical and Physical Characterization of a Two-Way Coupling Approach for the Simulation of Fluid Flows under Cryogenic Conditions
(versão corrigida após defesa)

Rúben Diogo Silva Oliveira Meireles

Dissertação para obtenção do Grau de Mestre em
Engenharia Aeronáutica
(mestrado integrado)

Orientador: Prof. Doutor André Resende Rodrigues da Silva

abril de 2021

Dedication

To my grandparents Maria Emília da Silva Nora Gomes, Fernando Alberto Rodrigues Baiona, Maria Emília Oliveira da Silva and António de Oliveira Meireles.

All that I am and all that I will ever be is inevitably due to what you have taught me and the example that you gave me during your lives.

Vocês são a minha pátria!

Acknowledgements

"In life, if you want to understand, seriously understand how things are in the world, at least once you must die. And so, given that this is the law, it is better to die when you are young, when you still have so much time before you in which to pick up yourself up and recover."

Giorgio Bassani, The Garden of the Finzi-Continis

Foremost, I would like to thank my advisor Professor André Silva for allowing me the opportunity of working in a scientific environment and rediscover my interest in science. Additionally, I want to express my deep gratitude to Leandro Magalhães for all his wise advice, support, and guidance on the course of this work. Furthermore, I thank you for sharing with me your insights relative to the scientific world and aspects that nothing had to do with this dissertation.

I big thank you to Emanuel Camacho for the interesting and enlightening conversations, the mutual exchange of experiences, and the share of knowledge during my stay at AEROG. I obviously extend my gratitude to my colleagues at the office with whom I had the opportunity of sharing this experience.

I want to thank my team of AEROUBI & AS Covilhã during the term 2017-2018. It was an extraordinary privilege to work alongside people that shared the same love, vision, and joy for associativism that I do, which certainly facilitated my job as President. It was really an enriching experience.

I also take this opportunity to especially thank my friends, which helped me along these past five years, encouraging me to be the best. Thank you for pushing forward with me in this psychological and scientific journey of seeking knowledge on differentiated levels.

More importantly, in the end, I want to acknowledge and thank my family for the combined sacrifice that did to ensure me the possibility of achieving professional and personal success. To my father, which instilled in me the sense of responsibility, integrity, and duty. To my mother, which redefined my concept of determination and relentlessness by following her dream, obtaining a BSc in Mechanical Engineering and, currently studying to obtain an MSc degree in the same area. And to my sister for her support, unconditional love, and headaches during this process. Thank you for believing in me.

Thank you all, you will not be forgotten.

Resumo

A cristalização de gotas de água é um fenómeno omnipresente que desempenha um papel fundamental em inúmeros processos naturais e artificiais. Este fenómeno ganhou um interesse particular na indústria aeronáutica devido à acumulação de gelo em superfícies sustentadores e na admissão dos motores. Adicionalmente, o setor aeroespacial também utiliza este fenómeno no desenvolvimento de combustíveis criogénicos para motores foguete.

O objetivo desta dissertação é estudar o arrefecimento de gotas de água, com diâmetros e razões de humidade do ar distintos, readaptando uma ferramenta computacional pré-existente para esse propósito. Deste modo, e tirando partido de um modelo de acoplamento em duas fases, utilizado para prever o comportamento de partículas discretas, já implementado nessa mesma ferramenta, adicionou-se um modelo matemático que considera a física por detrás do arrefecimento de gotas de água em estado líquido. Para prever os efeitos convectivos, a que as gotas estão sujeitas, foram usadas duas correlações distintas: a formulação clássica de Ranz-Marshall e uma formulação transiente que empiricamente corrige a anterior. Os resultados obtidos foram comparados com um estudo numérico onde um modelo de acoplamento em uma só fase foi implementado e dados experimentais disponíveis na literatura. Adicionalmente, para compreender a forma com que estes resultados são integrados num processo completo de congelamento por superarrefecimento, fez-se um estudo analítico utilizando um modelo de quatro fases e, posteriormente, compararam-se esses resultados com dados experimentais.

Os resultados numéricos demonstram que para elevadas razões de humidade a interação entre a partícula e o meio envolvente ganha predominância e necessita de ser contabilizada. Quando consideradas baixas razões de humidade, esta interação pode ser desprezada, tendo em conta que o modelo de acoplamento em uma só fase apresenta maior proximidade com os resultados experimentais. Adicionalmente, foi concluído que o modelo de mistura completa, que não contabiliza as vibrações e deformações na gota, é uma aproximação válida quando considerando razões de humidade baixas ou elevadas e que, para razões de humidade intermédias, o modelo de mistura, que contabiliza essas mesmas perturbações, apresenta maior proximidade com os dados experimentais. O modelo analítico implementado para o superarrefecimento completo de gotas de água foi capaz de prever o fenómeno.

Palavras-chave

Transferência de calor e massa, acoplamento em duas fases, formulação Lagrangiana, formulação Euleriana

Abstract

The crystallization of water droplets is a ubiquitous phenomenon, which plays a fundamental role in many natural and artificial processes. This phenomenon gained particular interest in the aeronautical industry due to ice accretion on lifting surfaces and engine intakes. Additionally, the aerospace sector also uses this phenomenon for the development of cryogenic rocket engines.

This dissertation aimed at studying the cooling of water droplets, at different diameters and air humidity ratios, through the conversion of a pre-existent in-house computational tool for that purpose. In order to predict the behavior of discrete particles, a mathematical model that accounted for the physics behind the cooling phenomenon of liquid water droplets was incorporated into the existing code. To predict the convective effects experienced by the droplets two correlations were used: the Ranz-Marshall classical formulation and an empirical transient formulation that corrects the first one. The results obtained were compared with a numerical study that used a one-way coupling model and experimental data available in the literature. To understand how these results are integrated into a complete freezing process, an analytical study of a full-scale four-stage freezing model was performed and further compared with experimental data.

The numerical results showed that for, high humidity content, the interaction between the particle and the surrounding environment becomes predominant and needs to be accounted for. When considering low humidity content, this interaction can be neglected since the one-way coupling resembles the experimental data in a better way. Additionally, it was concluded that the complete mixing model, which does not account for deformations and vibrations of droplets, is an acceptable assumption when considering low or high humidity ratios and that for intermediate humidity content, the mixing model assumption, which accounts for those effects, shows close agreement with experimental data. The analytical model implemented for the full-scale supercooling freezing of water droplets was able to predict the phenomenon.

Keywords

Heat and mass transfer, two-way coupling, Lagrangian formulation, Eulerian formulation

Contents

List of Figures

List of Tables

Nomenclature

$C_\mu, C_{\varepsilon 1}, C_{\varepsilon 2}, C_{\varepsilon 3}, \sigma_\varepsilon, \sigma_\varepsilon$	Turbulence model constants	–
A	Surface area	m^2
a	Eddy lifetime scale constant	0.2
b	Characteristic eddy size constant	0.164
C	Coefficient	–
c	Specific heat capacity	$\mathrm{J\,kg^{-1}\,K^{-1}}$
D	Mass diffusivity	$\mathrm{m^2\,s^{-1}}$
d	Droplet diameter	m
e	Emissivity	–
G	Turbulence kinetic energy production term	$\mathrm{kg\,m^{-1}\,s^{-3}}$
g	Gravity acceleration on Earth	$9.806\,65\,\mathrm{m\,s^{-2}}$
h_h	Convective heat transfer coefficient	$\mathrm{W\,m^{-2}\,K^{-1}}$
h_m	Convective mass transfer coefficient	$\mathrm{m\,s^{-1}}$
HR	Humidity ratio	–
K	Basset force constant	$3/2$
k	Turbulence kinetic energy	$\mathrm{m^2\,s^{-2}}$
L	Specific latent heat	$\mathrm{J\,kg^{-1}}$
l	Characteristic eddy size	m
M	Virtual mass force constant	$1/6$
m	Mass	kg
N	Number of particles	–
n	Unit vector in the direction of particle angular momentum	–
p	Pressure	$\mathrm{N\,m^{-2}}$
Q	Rate of heat transfer	$\mathrm{J\,s^{-1}}$
q	Heat flux per unit area	$\mathrm{kg\,s^{-3}}$

RM	Relative humidity	–
S	Source Term	–
SH	Specific humidity	–
T	Temperature	K
t	Time	s
U	Velocity	$\mathrm{m\,s^{-1}}$
u, v, w	Velocity coordinates	$\mathrm{m\,s^{-1}}$
V	Volume	$\mathrm{m^3}$
X	Position	m
x, y, z	Cartesian coordinates	m

Greek Symbols

α	Thermal diffusivity	$\mathrm{m^2\,s^{-1}}$
Δ	Time increment	s
δ	Kronecker delta function	–
ε	Dissipation rate of turbulence kinetic energy	$\mathrm{m^2\,s^{-3}}$
Γ	Effective diffusion coefficient	$\mathrm{kg\,m^{-1}\,s^{-1}}$
λ	Conductive heat transfer coefficient	$\mathrm{W\,m^{-1}\,K^{-1}}$
μ	Dynamic viscosity	$\mathrm{kg\,m^{-1}\,s^{-1}}$
ν	Kinematic viscosity	$\mathrm{m^2\,s^{-1}}$
ω	Angular momentum	$\mathrm{kg\,m^2\,s^{-1}}$
ϕ	General property per unit volume	$\mathrm{m^{-3}}$
ρ	Specific mass	$\mathrm{kg\,m^{-3}}$
σ	Stefan–Boltzmann constant	$5.6704 \times 10^{-8}\,\mathrm{W\,m^{-2}\,K^{-4}}$
T	Relaxation time	s
τ	Eddy lifetime scale	s
Υ	Mass fraction	$\mathrm{kg\,kg^{-1}}$

v	Eddy transit time	s
ξ	Third-order tensor	–

Superscripts and subscripts

0	Initial instant
∞	Far-field region
ϕ	General property per unit volume
a	Dry air
c	Cooling
D	Drag
d	Particle properties (liquid or solid)
$drift$	Drift
e	Eddy
g	Gas
h	Convective heat transfer
i	i^{th} coordinate direction, coordinate velocity, time interval
int	Interaction
ipt	Inter-phase transport
j	j^{th} coordinate direction, coordinate velocity, time interval
k	k^{th} coordinate direction, coordinate velocity, time interval
kol	Kolmogorov
l	Liquid
m	Convective mass transfer
n	Nucleation
NEW	Next time step
OLD	Current time step
p	Isobaric

ph	Phase change
r	Thermal radiation
rec	Recalescence
ref	Reference
rel	Relative
s	Solid
sat	Saturated
t	Turbulent
$total$	Total
$v-g$	Vapor-gas
wv	Water vapor

Acronyms and abbreviations

ADREP	Accident/Incident Data Reporting
CFD	Computational Fluid Dynamics
FAA	Federal Aviation Administration
FVM	Finite Volume Method
ICAO	International Civil Aviation Organization
ICTS	Icing Contaminated Tail Stall
IMS	Ice Management System
IPS	Ice Protection System
MVD	Median Volumetric Diameter
NACA	National Advisory Committee for Aeronautics
NASA	National Aeronautics and Space Administration
NTSB	National Transportation Safety Board
OW	One-way coupling model
PDF	Probability Density Function
QUICK	Quadratic Upstream Interpolation for Convective Kinematics

RANS	Reynolds-averaged Navier–Stokes equations
RM	Ranz-Marshall classical formulation
RMcf	Ranz-Marshall corrected formulation
SIMPLE	Semi-Implicit Method for Pressure Linked Equations
SIS	Smart Icing System
SLD	Supercooled Large Droplet
SSF	Stochastic Separated Flow
TDMA	Tridiagonal Matrix Algorithm
TW	Two-way coupling model
UAM	Urban Air Mobility
UAV	Unmanned Aerial Vehicle
VTOL	Vertical Take-Off and Landing

Dimensionless Numbers

Bi	Biot number	$\mathrm{Bi_d} = \dfrac{h_h d}{2\lambda_d}$
Le	Lewis number	$\mathrm{Le_d} = \dfrac{\alpha_{v-g}}{D_{v-g}}$
Nu	Nusselt number	$\mathrm{Nu_d} = \dfrac{h_h d}{\lambda_g}$
Pr	Prandtl number	$\mathrm{Pr_d} = \dfrac{c_{p,g}\mu_g}{\lambda_g}$
Re	Reynolds number	$\mathrm{Re_d} = \dfrac{\rho_g \parallel \overrightarrow{U}_{rel} \parallel d}{\mu_g}$
Sc	Schmidt number	$\mathrm{Sc_d} = \dfrac{\mu_g}{\rho_g D_{v-g}}$
Sh	Sherwood number	$\mathrm{Sh_d} = \dfrac{h_m d}{D_{v-g}}$
Ste	Stefan number	$\mathrm{Ste_d} = \dfrac{c_{p,d}\,(T_d - T_{ph})}{L_{ph}}$

Chapter 1

Introduction

Considering that the crystallization of water droplets has a key role in many natural and artificial processes (Meng and Zhang [2020]), a better understanding of this phenomenon is of interest to several areas. According to Khalil and Sobhi [2020] one of the food supply chain's most energy-consuming activities, taking up to thirty-five percent of the power used by the food industry, is refrigeration. Air conditioning is a widely recognized problem concerning the low efficiency and, therefore, the increased energy consumption of devices. Moreover, the freezing of sprayed water droplets onto exposed surfaces, and above-deck ice build-up on ships, which, consequently, alters the center of gravity of vessels, reduces their stability, and increases the fuel consumption, constitutes a great danger to daily operations (Samuelsen and Graversen [2019]).

Additionally, Fakorede et al. [2016] described the increased popularity of wind energy projects in cold climates due to the high wind potential and the availability of land, taking into account that ice decreases the optimal performance of wind turbines. Additionally, ice leads to aeolian plants shut down due to a heightened load, stress, increased vibration, and turbulence. Increased knowledge about the crystallization phenomenon would also benefit the cryogenic preservation of cells, the development of medicines, and vaccines conservation. Besides, Yancheshme et al. [2020] stated that accidents on roads and highways, during freezing rain events, the structural deformation of power and communications transmission towers, conductors, and insulators exposed to ice and snow accumulation, offshore structures that collapse due to the accretion of high quantities of sea-spray droplets, also constitute examples of negative consequences on the performance of equipment, facilities, and infrastructure due to ice accumulation.

A particular case in which the cooling and freezing of water droplets has a considerable impact is on the aeronautical and aerospace sectors. For instance, ice accretion on lifting surfaces has a major impact on aircraft performance resulting, ultimately, in the irrecoverable loss of the vehicle. Ice formation in aircraft fuel systems (Murray et al. [2011]) is also a problem. Furthermore, cryogenic fuels or oxidizers also constitute an important area of interest in the aerospace sector.

All in all, different areas would benefit from a better understanding of the freezing and cooling phenomena. Through better control of the heat and mass transfer process, it would be possible to increase the overall performance and efficiency of different systems, mitigate structural and mechanical failures, enlarge the lifetime of devices, reduce economic

damage, via the loss of millions of euros in services and products, and, ultimately, prevent the loss of human lives. Albeit, with potential impacting effects in several industries, during the present document, the focus lies in the aerospace industry, as described next.

1.1 The effect of icing-related effect in the aerospace industry

Considering now statistical data, the Federal Aviation Administration (FAA), the governmental body of the United States with powers to regulate all aspects of civil aviation, reported that if the current accident rate holds constant and airline transportation continues at the current rate, there will be more than 4500 air travel fatalities per year worldwide by 2025, as mentioned by Caliskan and Hajiyev [2013].

Other international organizations, governmental institutions, and third parties, which built accidents and incidents (potential precursors to accidents) databases, came to similar conclusions. For instance, and focusing in our subject of study, Zeppetelli and Habashi [2012] collected data from the International Civil Aviation Organization (ICAO) accident and incident data-reporting database (ADREP) between 1970 and 2010. In total, during this period were registered 323 events related to ice accretion. Concerning this study, it is important to bear in mind that aircraft accidents/incidents under $2250\,\mathrm{kg}$ are not required to be reported to ICAO. Furthermore, ground icing related events were not accounted for. Figure 1.1 presents, in a systematic way, the data gathered by this study.

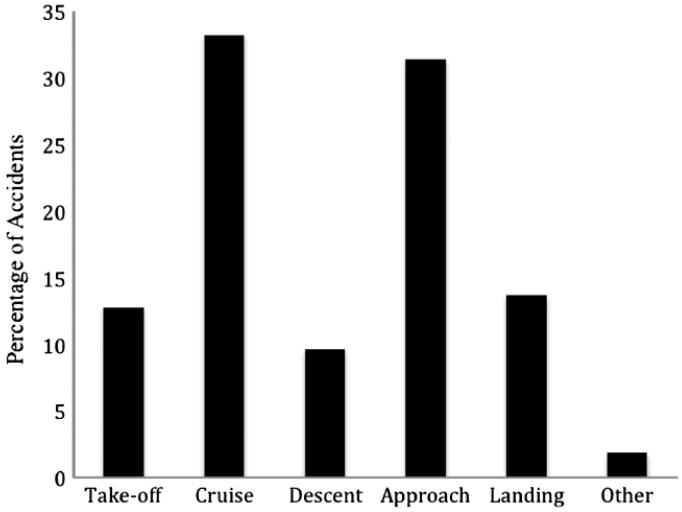

Figure 1.1: Percentage of occurrences by phase of flight, from Zeppetelli and Habashi [2012].

Analyzing Figure 1.1, it is possible to determine in which phase of flight an aircraft is most vulnerable to the aerodynamic penalties due to ice accretion. A substantial number of accidents were reported during two particular phases: cruise and approach. The two stages make up more than $60\,\%$ of the occurrences. On these phases, it is important to notice that any angle of flap or control input, by the pilot, has a significant impact on the flight resulting in a higher instability and, consequently, a catastrophic end. Even though, the phase of flight in which the incidents occur and the phase in which ice is accreted do not

need to be the same, bearing in mind that accidents were examined based on the flight phase at the time in which ice was found.

In 2015, Green, on behalf of the FAA, published the icemaster database and an analysis of aircraft aerodynamic icing accidents and incidents. In this report were aggregated accidents and incidents databases between 1982 and 2010 on the United States. This report was divided into two datasets, one concerning in-flight icing, which comprised 308 events, and another ground icing, which comprised 248 events. Apart from what was already explained, Green [2015] also examined historical trends, awareness by the pilot-in-command, license, total hours of flight, and the influence of introducing airworthiness certifications and its consequences on the prevention of events.

Similarly to what was concluded by Zeppetelli and Habashi [2012], Green [2015] stated that the phases where an aircraft is more susceptible to in-flight icing occurrences are the cruise, approach, and landing which, correspond, respectively, to 34 %, 27 % and 17 % of the occurrences. Furthermore, it is seen, when examining Figure 1.2, that stall is the main occurrence responsible for incidents/accidents, leading to more than 50 % of the events stated in this report.

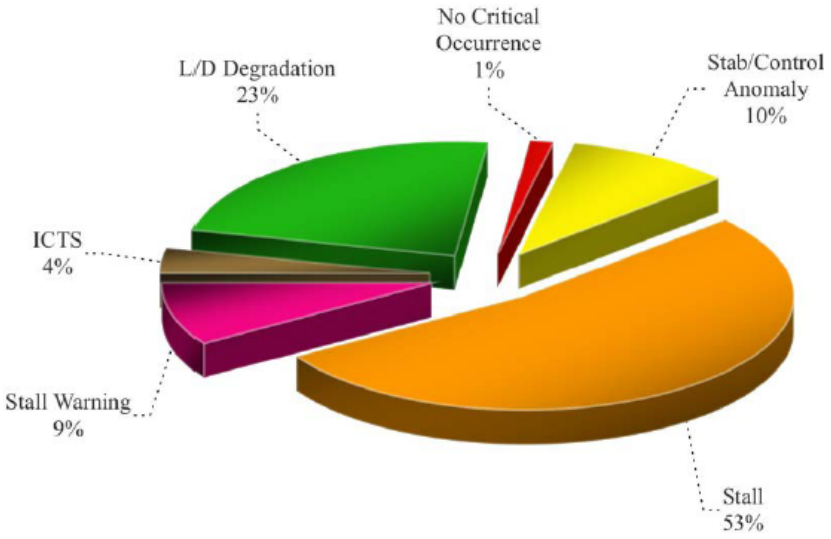

Figure 1.2: Percentage of critical occurrences that lead to an event, from Green [2015].

In what concerns the type of aircraft that is more affected due to ice, according to Green [2006], which studied the United States in-flight icing accidents and incidents between 1978 and 2002, smaller-scale reciprocating engine aircraft, which, commonly, are not equipped with Ice Protection Systems (IPSs), experience the significant majority of events that involve performance degradation resulting in accidents. This study was reinforced later by Jones et al. [2008] on a subsonic aircraft safety icing study on behalf of NASA. Further information was compiled by Dillingham [2010], where icing and winter weather related incident reports, for large commercial aircraft, by category of the incident, between 1998 and 2007, were presented. NASA Funding and Staffing for Icing-Related R&D between 2005 and 2013 were also presented and commented.

In these studies different causes are attributed as the source of the accidents or incidents. For example, wing stall, Icing Contaminated Tail Stall (ICTS) which translates the loss of pitching control when the tailplane angle of attack exceeds the stall angle of attack, icing contaminated roll upset (which particularly contributes to a reduction on control efficiency), icing on flap leading edge (usually causes the air separation in advance on the flap surfaces and slump in the flap efficiency), engine and air intake icing (resulting in engine flameout), carburetor icing, propeller icing, static and dynamic port blockage, probe icing, windshield icing and asymmetric air separation (due to asymmetric icing) only constitute a small portion of the factors reported in the previous studies. These examples, if not taken into account, and mitigated, can affect, apart from the performance figures, both the longitudinal and directional stability, making the aircraft uncontrollable and, in the long run, irrecoverable.

However, even with the studies and conclusions previously referred, as claimed by Cao et al. [2018], lessons usually learned by one generation, with aspect to the various serious consequences of aircraft icing, have not been well disseminated or accepted by the latest generations. Those difficulties have resulted in many ice-induced accidents, which could have been avoided if enough attention had been paid.

1.2 Objectives

The final aim of this work is to obtain a computational tool capable of simulating different icing formation regimes considering distinct lifting surfaces, such as a wing, allowing to conclude the impact of ice accretion on the aerodynamic performance of an aircraft. However, this constitutes a huge challenge and, therefore, it requires to be divided into distinct steps. The first of those steps consists of obtaining the temperature profile for a cooling water droplet.

As a consequence of dealing with problems related to droplet's dynamics and their heat and mass transfer with the surrounding environment, our research group had available an in-house code, which could be adapted to predict the cooling of water droplets. To understand the available capabilities of the pre-existent tool is presented a brief resume of the publications, which resulted in the direct application of this tool.

A fully three-dimensional computational method to study turbulent two-phase flows was implemented and tested by Barata et al. [2002] for the case of an array of droplets through a cross-flow. This method was based on the solution of Reynolds-averaged Navier-Stokes equations (RANS) and a Stochastic Separated Flow (SSF) model to the problem of an array of droplets through a cross-flow. Barata et al. [2002] examined the influence of the droplet sizes on the dispersion phenomenon. The exchange of momentum, and turbulence energy, was discovered to play a decisive role in changing the gaseous flow velocities. In 2008, Barata and Silva performed a numerical study of a spray impinging on a surface

through a cross-flow, comparing the predictions with measurements and calculations of other authors. Three spray impinging models were combined into the same three-dimensional computational method based on solving the RANS for the gas phase and a SSF model, based on eddy lifetime, for the particle phase, as previously used.

More recently, Rodrigues et al. [2016] addressed the macroscopic atomization characteristics of liquid-fuel droplets when subjected to the influence of a high-velocity air cross-flow, obtaining a reasonable agreement between measurements and predictions in both the qualitative and quantitative outcomes evaluated. A year after, Rodrigues et al. [2017] presented a numerical study on evaporating droplets impinging onto a solid surface through a cross-flow. In this study, a readjustment to the previously built tool allowed us to infer the influence of two distinct initial temperatures on the outcome of spray impingement.

After examining the history of an available in-house computational tool, was concluded that the mathematical models for the droplet motion and the interaction between the particles and the surrounding environment are the same for liquid-fuel and water droplets. However, the mathematical models on the existing tool account for the evaporation phenomenon of liquid-fuel droplets and, for that reason, need to be changed to account for the physics behind the cooling of liquid water droplets. Consequently, this tool can be used to fulfill the first step stated before although, it requires some adjustments.

Therefore, the main objective of this dissertation is to numerically predict the cooling of water droplets by readapting a pre-existent computational tool. To do so, it was necessary to interpret and comprehend the physics and mathematics already implemented on the existing tool, mathematically model the mechanisms behind the cooling and freezing of water droplets, identify and make the necessary changes to the computational tool, and, finally, numerically simulate the phenomenon. Additionally, to provide insights about this phenomenon and guarantee that the model selected can describe the process, the numerical predictions were compared to the results obtained with experimental and numerical studies gathered by other researchers.

1.3 Outline

The present dissertation is organized into seven distinct chapters. The current chapter, Chapter 1, provides the general scope of this dissertation, its motivation, and objectives behind the research. Chapter 2 addresses the icing phenomenon by detailing the work performed in this area during the last years and presenting a theoretical review. Chapter 3 presents the available capabilities at disposal and the methods applied to the computational tool that was adapted for this dissertation. Chapter 4 describes the physical phenomenon behind the freezing of water droplets, resorting to a four-stage freezing model, and states the mathematical methodology used. Chapter 5 presents a comparison between two

distinct methodologies considering, or not, the mutual interaction between the droplet and the surrounding environment. The effect of the air humidity ratio and the droplet diameter is also analyzed. In Chapter 6, the results of an analytical full-scale four-stage freezing study are presented and compared with experimental data. Finally, Chapter 7 summarizes the most important conclusions of this research and presents future work suggestions.

Chapter 2

State of the art: from physical systems to thermodynamic formulations

This chapter presents a theoretical review of the physical processes inherent to the cooling and freezing of water droplets. Section 2.1 introduces the phase-change problems and addresses the difference between normal cooling and supercooling. In Section 2.2, the ice formation phenomenon is addressed and briefly described. Section 2.3 reviews the typical morphologies that ice accretion causes on aircraft, particularly on wings. Section 2.4 reviews the de-icing and anti-icing systems available nowadays, addressing problems and new solutions to the ice accretion danger. Section 2.5 presents the work performed on this subject during the last years by presenting a bibliographic review of this phenomenon, specifically on the ice accretion of lifting surfaces and engine intakes. Section 2.6 reviews the numerical efforts achieved along the years discussing, some of the computational tools used to predict ice accretion on aircraft.

2.1 Introduction to phase-change problems

2.1.1 The Classical Stefan Problem

As a consequence of what was previously seen, the interest of researchers in physically and mathematically model the ice formation phenomenon increased, resulting in new theories and explanations. The traditional formulation for solidification or melting problems is The Classical Stefan Problem. This problem constitutes the simplest physical and mathematical model used to comprehend the phase-change phenomenon. This problem is a primary model on which, progressively, more complex models were, and can be, built on, incorporating effects initially left out. An extensive approach to this problem can be found on Alexiades and Solomon [1993] and Gupta [2017]. These authors present a detailed view of this phenomenon, including different approaches that are frequently applied in other industries. Metallurgical manufacturing, temperature-sensitive devices for medical purposes, supercooling, superheating, or extended classical formulations of n-Phases constitute some applications of this phenomenon.

Generically, phase-change problems are mainly characterized by the temperature field and the location of the interface between the different phases (propagation of ice-water phase front, in the case of freezing droplets), which are difficult to predict or usually unknown. In the case of water, we are in the presence of a two-phase Stefan problem since we have a

mixture of two distinct phases. Stefan problems are associated with free boundary problems[1] or moving boundary problems which, in this case, can be called a phase-change boundary or a freezing front, where two boundary conditions have to be considered to obtain a well-posed problem.

To evaluate if a given method is appropriate, researchers usually resort to a dimensionless number called Stefan Number, $\mathrm{Ste_d}$. This number relates sensible heat to latent heat and is a key number when solving solidification or melting problems. Therefore, small values of this number indicate that the temperature in the phase change process is, at any time, essentially at its steady-state (quasi-stationary), because of the quickness of the response of temperature relative to the movement of the phase change front. This dimensionless number is given by Eq. (2.1), where the subscript d denotes the particle properties (liquid or solid), the subscript ph indicates that a propriety is obtained during the phase-change process, $c_{p,d}$ is the droplet specific heat capacity at constant pressure, T_d the droplet temperature, and L is the specific latent heat.

$$\mathrm{Ste_d} = \frac{c_{p,d}\,(T_d - T_{ph})}{L_{ph}} \quad (2.1)$$

Considering that the number of problems with an explicit solution is extremely low and, in most cases, does not have relevance in real-life situations, to easily find a solution to the phase-change processes, it is necessary to simplify the problem formulation. Therefore, different assumptions can be made, attending to the physical factors involved in the phase-change processes. Yet, it is crucial to carefully apply these assumptions when modeling this phenomenon, considering that a model can be at best as good as its underlying physical assumptions.

Different analytical and numerical approximations are used to obtain a result for the problem. Analytical models consist of a closed-form mathematical solution to the governing transport equations subjected to the initial and boundary conditions. On the other hand, numerical models are based on a numerical procedure, such as finite differences or finite elements. Examples of these two approaches consist of quasi-stationary approximation, Megerlin method, heat balance integral method, perturbation method, or the enthalpy formulation, as attested by Alexiades and Solomon [1993] and Gupta [2017].

[1] Problems in which the geometry of the domain, on which an equation has to be solved, is, a priori, unknown. As a consequence, if a partial differential equation has to be solved in a domain, from which a part of the boundary is unknown, that problem is characterized as a free boundary problem.

2.1.2 Supercooling versus normal cooling

The process of freezing water droplets, in a simple manner, consists of a nucleation [2] phase followed by crystal growth, where tiny crystal structures grow and aggregate with others until the entire substance is solidified. During this process, molecules arrange themselves into more ordered, lower energy states, and in the process, release latent heat. On a normal cooling, this process occurs at the phase-change temperature, and consequently, the freezing and melting temperatures are almost the same. This process is more common in fluids with irregularities, impurities, or vibrating fluids.

In contrast to a normal cooling, many liquids, especially for pure substances that lack nucleation agents, crystallization can begin at temperatures that lie far below the material's freezing point, T_{ph}. In this case, the phenomenon is called supercooling or undercooling. It consists of a thermodynamically metastable state, which is a local state of minimal energy and not global, where the liquid is placed out of equilibrium state, meaning that the free energy [3] is higher than the real stable state, which is solid. Thus, it is easy to describe it as the process of lowering the temperature below its usual freezing point without the phase change solidification (formation of ice crystals) occurring. The subsequent solidification process is also referred to as flash-freezing.

To easily comprehend the two distinct cooling processes, cooling curves for normal freezing and supercooling are shown schematically in Figure 2.1. Figure 2.1a represents a normal cooling process, considering that the freezing stage, and consequently the crystallization, occurs, always, at the same temperature. Otherwise, in Figure 2.1b, it is possible to see that temperature goes below melting temperature and eventually rapidly rises back, suggesting that crystallization does take place. This fact only occurs if the latent heat released upon freezing is sufficient to raise the temperature back to melting temperature, indicating that the liquid was not overcooled originating, another process which is hypercooling.

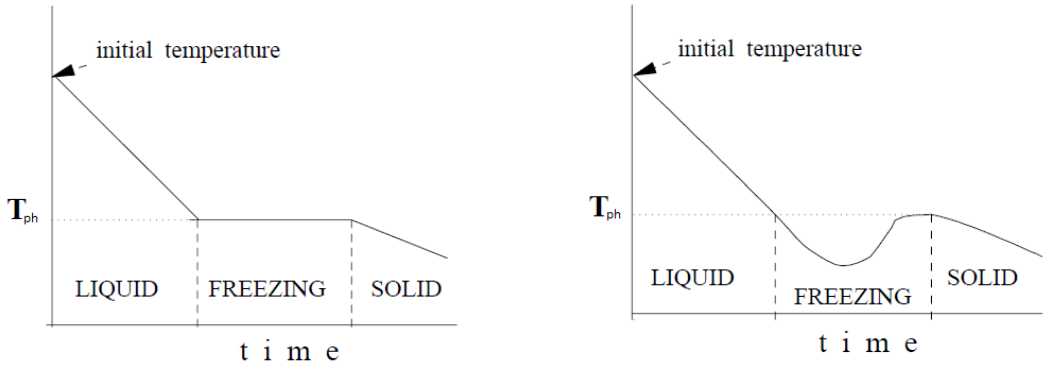

(a) Normal cooling process

(b) Supercooling process

Figure 2.1: Cooling curves considering a material sample for normal cooling and supercooling, adapted from Alexiades and Solomon [1993].

[2] The initial process that occurs in the formation of a crystal from a solution, a liquid, or a vapor, in which a small number of ions, atoms, or molecules become arranged in a pattern characteristic of a crystalline solid.

[3] Maximum amount of work that a thermodynamic system can perform in a process at a constant temperature.

2.1.3 Supercooled large droplets - SLDs

The impingement of water droplets in the form of freezing rain, freezing drizzle, or snow particulates and its accumulation on aircraft lifting surfaces and engine intakes constitute what is commonly known as ice accretion. Supercooled water droplets, which typically have a Median Volumetric Diameter (MVD) of less than $50\,\mu\mathrm{m}$, are the most common cause of ice accretion on aircraft, impacting the surface and consequently freezing upon contact near the stagnation line of the wing. According to Cao et al. [2018], supercooled water droplets are unstable, which makes them freeze once they are disturbed and in a wide range of atmospheric conditions. Numerous parameters, such as droplet size, atmospheric conditions, airfoil and surface geometry, aircraft velocity, or the angle of attack contribute directly to ice accretion, as reported by Parent and Ilinca [2011]. Additionally, the aircraft's geographic location has a huge influence on some of the parameters presented before.

Nevertheless, one particular type of supercooled water droplets causes abnormal icing, leading to complex ice geometries and, consequently, more serious effects on aircraft performance. Supercooled large droplets (SLDs), which are typically larger than $50\,\mu\mathrm{m}$ (maximum water droplet diameter in the range of $100\,\mu\mathrm{m}$ to $500\,\mu\mathrm{m}$ for freezing drizzle icing condition, and greater than $500\,\mu\mathrm{m}$ for freezing rain icing condition), freeze upon contact like other types of supercooled water droplets. However, the release of their latent heat during the phase-change phenomena melts them back into the liquid phase and, with the flow induced by the movement of the aircraft, refreeze further back on the wing, where the IPSs do not take action. Thereby, this phenomenon strongly indicates that the thermal effects during the impact process of SLDs cannot be neglected and constitute a significant research subject, as noticed by Zhang and Liu [2016].

Furthermore, SLDs icing is significantly different when comparing its behavior with conventional supercooled water droplets, differing on the water droplet spatial motion pattern, droplet-wall collision process, effects on the wall boundary layer flow, and other parameters. Since the diameter of SLDs is larger, when comparing this type of droplets with the conventional supercooled water droplets, SLDs have greater inertia and, consequently, more energy. This fact contributes to a stronger accretion in areas where conventional icing does not accrete. For these reasons, many assumptions considered in many icing cases do not apply to SLD icing conditions.

2.2 Ice formation phenomenon

Relatively to the regimes in which SLDs are formed, it is possible to characterize two distinct types: rime ice and glaze ice. Although these regimes are predominant and frequently seen separately, some authors consider that aircraft are often exposed to both regimes simultaneously with characteristics of glaze and rime ice with no fixed ice shape, as stated by Cao et al. [2018]. This originates a third regime called mixed ice, which consists of a mixture of the previous two, and, consequently, is formed in the middle of the freezing

range.

The concentration of SLDs and ice crystals inside clouds varies according to diverse factors, for instance, altitude, air temperature, pressure, or density. For a better understanding, in Figure 2.2 the predominant zones of icing formation regimes are represented according to altitude and air temperature.

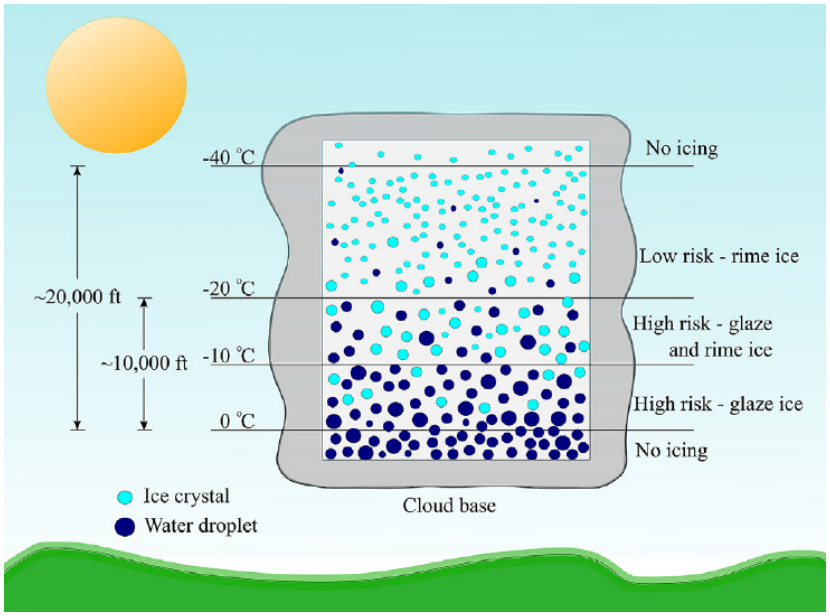

Figure 2.2: Ice formation regimes within a cloud and the resulting probability of aircraft icing, from Stebbins et al. [2019].

Generally, rime ice occurs at the coldest conditions (e.g., below -20 °C) in stratiform clouds in which, consequently, water drops freeze almost immediately upon impingement on lifting surfaces, having a white opaque appearance with a hemispherical shape (three-dimensional shape that is half of a sphere with one flat, circular side). Therefore, rime ice consists mostly of frozen SLDs. This type of ice is generated from smaller water droplets, considering the size range of SLDs, which cannot coalesce and, as a result, freeze in place. This regime is characteristic of clouds with low liquid water content [4] (LWC). This type of ice has a rough texture, although it is fragile and easily shattered. Rime ice, according to Cao et al. [2018], may increase the total drag by as much as 100 % reducing the aircraft aerodynamic performance and increasing the fuel consumption.

On the other hand, glaze ice occurs at warmer conditions, ranging from -10 °C to 0 °C, and, for that reason, water droplets tend to spread and run downstream before freezing on the wing surface. Glaze ice has, generally, a clear or translucent appearance consisting of partially frozen supercooled water droplets with large size. This regime is formed just below the freezing temperature of water in mostly cumulus type clouds. Glaze ice is difficult to

[4]Liquid water per unit volume. Liquid water content is closely related to the types of clouds. This propriety widely varies attending the conditions in which these clouds are formed. High liquid water content clouds have, predominantly, liquid water droplets and are found in low altitudes. On the other hand, cloud with a low liquid water content are usually found at higher altitudes and incorporate ice crystal

remove as the supercooled water droplets exist mostly in the liquid state, due to the clouds high LWC, being able to coalesce, and, consequently, form a sheet with a continuous bond to the surface.

Additionally, Figure 2.2 represents a region that is discriminated as ”No icing”. As the temperature decreases, the amount of water vapor the air can hold, also known as saturated vapor density, decreases contrarily to the probability for the freezing of droplets, which increases, leading to a reduced icing probability. Between -10 °C and -20 °C the aircraft is on a high risk mixed ice zone. The altitude range presented for each zone is merely representative of where that type of temperature is usual. According to Cao et al. [2018] glaze ice is likely to increase the drag by 200 % to 300 %.

In addition to the icing formation regimes presented previously, it is important to enhance that icing also occurs below the cloud level in freezing rain conditions. Two regimes usually studied are the hoar frost and snow. Hoar frost is formed while the aircraft is on the ground or in-flight when descending from below freezing conditions to an altitude with warm and moist air. It has a particular impact on pilot's visibility and aircraft performance since it fixes on rough surfaces. On the other hand, snow accumulates commonly on the ground and is a mixture of ice and water.

2.3 Ice accretion on aircraft

Taking into account that SLDs have greater inertia and energy when compared to the conventional water droplets, different shapes are excpected since the icing severity upon accretion is different. Generally, ice accretion on aircraft occurs on the upper and lower wing surfaces, fuselage, propellers, engine nacelles, and sensor ports, as it was observed by Huang et al. [2019]. In the particular case of engines, in accordance with Gurevich et al. [2020], which examined the impact of control methods on turbofan engine performance in ice crystal conditions, if large pieces of ice shed into the engine core flow-path, the compressor might be damage, a surge may occur, the combustion chamber may flame out, and the engine may fail.

These different types of geometries are explained with the quantification of energy for each droplet. When considering SLDs, low energy droplets are quickly frozen on the aircraft surface due to low temperature. On the other hand, SLDs with higher energy are not immediately frozen, flowing along the surface until their energy is depleted and froze. This phenomenon is translated into different geometries. It is possible to identify four major types of accretion geometries that occur during various icing conditions: ice roughness, streamwise ice, horn ice, and spanwise ridge ice.

Rime ice tends to be associated with streamwise ice and roughness ice, while horn and ridge ice tend to be associated with glaze ice. For a better understanding, Figure 2.3 shows the different types of iced-airfoil flow fields, the icing conditions in which they are formed on the

aircraft and their effect on aerodynamic performance.

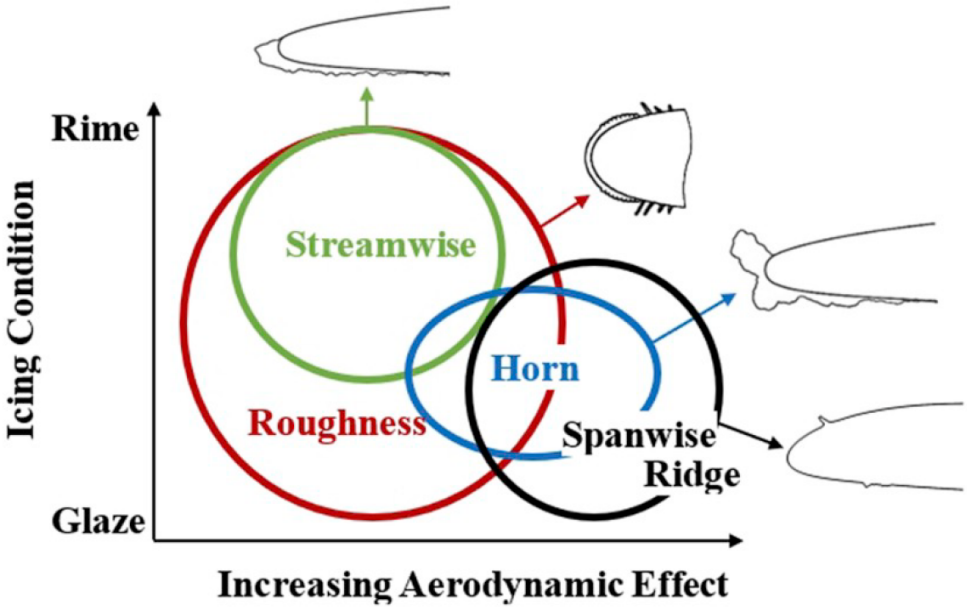

Figure 2.3: Qualitative description of aerodynamic effects for various iced-airfoil flow fields, in terms of icing conditions and typical impact on aerodynamic performance, from Stebbins et al. [2019].

Concerning ice roughness, this type of geometry tends to occur when the icing exposure is short-lived or during the initial stages of ice accretion. Ice roughness has a wide range of aerodynamic impacts being formed under a whole range of icing conditions. This type of shape is characterized for having two main zones: smooth and rough. The smooth zone has, normally, little aerodynamic effect. On the other hand, for the rough area, a premature transition of the boundary layer, from laminar to turbulent conditions, may appear, increasing the drag and diminishing the aerodynamic efficiency. This morphology type is usually documented in the literature since it has a wide range of actuation, resulting in complex three-dimensional forms, making it very difficult to modulate computationally.

Streamwise ice develops from ice roughness and is usually formed under cold temperatures, justifying the fact of being characteristic in rime icing conditions. This ice shape, in resemblance to ice roughness, has a moderate aerodynamic impact since accreted ice follows the contour of the airfoil surface keeping, almost always, the flow locally attached, minimizing the impact on the pressure distributions. Even though, separation tends to occur near the junction of the ice shape with the airfoil and may fluctuate depending on the angle of attack and the boundary layer conditions.

Horn ice also develops from ice roughness and usually appears when the wing is already exposed to glaze or mixed icing conditions. Horn ice form is characterized by the horn height, the angle that the horn makes with the chord line, and its location. Usually, the horn tip holds the flow separation location, fixed for most angles of attack, causing a large separation bubble downstream of the horn. This separation is highly unsteady and

three-dimensional due to the turbulent nature of the separation, causing a pronounced redistribution of pressure, which results in pitching moment changes, decreased lift, and increased drag. According to Stebbins et al. [2019], horn ice is one of the most examined ice shapes since it has a strong impact on aerodynamics.

Finally, regarding spanwise ridge geometry, this type of ice shape forms downstream of the leading edge being, generally, associated with SLDs conditions, albeit it can occur for all droplet sizes. One of the biggest problems associated with this type of ice, making it particularly dangerous, is that anti-icing systems that are not fully evaporative, may prevent freezing in leading-edge areas, where heat is added but, the liquid water can run back past the heated zone and form ridge ice accretion downstream. This phenomenon is prone to form what is called run-back ice. A similar result can occur for a pneumatic de-icer. In terms of location, spanwise ridge ice tends to occur just downstream of the airfoil suction peak, where there is a strong adverse pressure gradient. On that point, the boundary layer is more susceptible to flow separation making it more likely to cause a premature stall.

It is important to notice that, for all these types of ice shapes, the aerodynamical impact, was found to become, generally, more profound at higher angles of attack, where it impacts significantly the stall behavior, as it is noticed on Stebbins et al. [2019]. Even though the classification of these ice forms may seem compartmentalized. Nevertheless, these geometries may occur simultaneously at different wing locations, making it very difficult to modulate or study separately.

At last, after describing the accretion phenomena on regular aircraft, is important to consider another type of vehicle which is also susceptible to ice, helicopters. Though ice accretion is less dangerous to helicopters compared with snow, slush, or visibility factors, it still constitutes a great hazard factor making it interesting to study. According to Cao and Chen [2010], which summarizes the icing effects on helicopter's performance, ice accretion on the main rotor has terrible effects affecting the total lift, power available, and structural integrity.

Furthermore, the effects of ice accretions on the inlets, cooling bay inlets, tail rotor, and others are also disadvantageous. This topic becomes highly relevant when thinking about Urban Air Mobility (UAM) new concepts since the number of unmanned aerial vehicles (UAVs) in operation is rapidly growing. These solutions usually consist of tilting-wing aircraft or another type of Vertical Take-Off and Landing (VTOL) aircraft, which have similarities with helicopters and regular aircraft simultaneously.

2.4 Physical systems

Traditionally, aircraft were equipped with icing sensors, which only recognized the danger when the aircraft was already subjected to ice accretion. These sensors would not quantify the effect of ice on the overhaul performance or activate the protective systems. During the

last two decades, devices evolved into what are now called Smart Icing Systems (SISs). These types of systems account for the ice accretion in iced lifting surfaces, the consequences that it imposes on aircraft performance, and how fast the degradation of flying capabilities occurs.

The data is gathered on an Ice Management System (IMS), which consists of a software center that further evaluates the data obtained and determines the appropriate response, communicating it to the pilot and the aircraft automatic systems. After the information is interpreted is then transmitted to the IPS, characterized based on the physical principle used to remove the ice (pneumatic, chemical, thermal, or mechanical). Thereby, this philosophy is closely related to the concept of flight envelope protection which is based on the actual, real-time ice accretion experienced by the aircraft, as introduced by Hossain et al. [2003].

Through Figure 2.4, it is possible to comprehend the theoretical functioning of the SISs. Firstly, these systems sense the presence of ice accretion and classifies its effect on aircraft performance, stability, and control. Hereinafter, the SIS automatically activates and manages the IPS. This provides the pilot feedback on the system status and behavior of both the aircraft and the IPS. If the performance degradation becomes significant, it modifies the aircraft flight envelope using the flight control system to avoid conditions in which the aircraft is potentially uncontrollable. Furthermore, it notifies the pilot of this action, and its implications for the original flight envelope, adapting the control system to maintain safe flight.

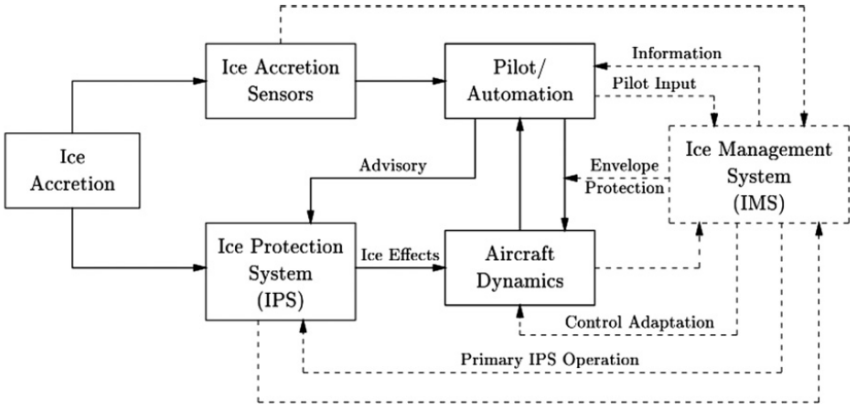

Figure 2.4: Generic scheme of the functions performed by a SIS, adapted from Bragg et al. [2002].

Generally, IPSs can be of two natures: active (heating elements, mechanical actuators, surface acoustic wave actuators, piezoceramic actuators, or others) or passive (nano-textured hydrophobic coating or any other system that does not need any power supply). Two distinct philosophies, de-icing and anti-icing, are used to overturn snow, ice, or frost accumulation on lifting surfaces or engine intakes.

De-icing refers to the removal of ice from aircraft surfaces. Its methods include heating, vibration (contact or non-contact), mechanical means, as inflated boots on aircraft leading edges, and sprayed-icing fluids to remove any ice accretion. Thereby, de-icing is aimed at

detaching already established ice accumulation. On the other hand, anti-icing consists of a preventive process that delays or reduces ice accretion on surfaces so that, subsequently, the de-icing process is not needed or less time/energy is required during the de-icing process. Frequently, aircraft are sprayed with anti-freezing agents or subjected to hydrophobic or icephobic permanent coatings. This process delays and prevents freezing and ice adhesion.

Nevertheless, many de-icing fluids used for de-icing and anti-icing purposes have a severe environmental impact, as stated by Huang et al. [2019]. Although, among the most popular of these systems, thermal IPSs are well-suited for aircraft surfaces prone to ice accretion. Even being widely used, these systems require relatively huge quantities of energy. Moreover, the energy requirements are strongly affected by the outside temperature and are maximized when the IPS is on running-wet mode[5]. Additionally, according to Strobl et al. [2018], the action of this system is confined only to a small area around the heat source.

As consequence, the actual demand is for a permanent long-lasting solution that is effective and, at the same time, lightweight, low in power consumption, maintenance time, manufacturing costs and on its environmental impact.

In the particular case of helicopters, which are especially subjected to a harsh vibratory environment, most of the solutions presented before are maladjusted. Anti-ice systems for helicopters consist, mainly, of heating elements inside the blades. However, this requires an electrical power generation plant, and, consequently, derivation of energy, loss of engine performance, and an increased fuel consumption. Nevertheless, systems such as rotary transformers have the potential of transferring the electrical power by magnetic induction and, therefore, without contact. Brunetti et al. [2020] introduced a rotary transformer assisted by switching power electronics.

2.5 Physical description

Researchers first began looking into the icing phenomenon on aircraft in the 1920s, when, at the time, the National Advisory Committee for Aeronautics (NACA) published several technical reports, as for instance Carroll and McAvoy [1928], Carroll and McAvoy [1929], and Noth and Polte [1936], which addressed the ice formation and the expose of certain parts of an aircraft, in flight, to ice. Consequently, methodologies to bypass or mitigate this factor were developed, being possible to date the first anti-ice system, though very simple, during the 1930s.

[5]Thermal ice protection systems are classified according to three principals being the running-wet anti-icing system one of them. In this principle, energy is only provided to prevent freezing in the heated surface. Beyond the heated surface of a running-wet system, the water can freeze, resulting in run-back ice which constitutes a great danger.

However, it was only in the 1940s that aircraft icing research became increasingly important due to a significant number of icing incidents/crashes in World War II related to military aircraft. After the war, Hardy [1947] made several suggestions concerning ice protection systems for aircraft, identifying ice as an unsettling phenomenon. In 1953, Grey and von Glahn studied the effects of run-back icing and frost formations on the drag of a NACA $651-212$ airfoil section over a range of angles of attack from 20 to 80 degrees and airspeeds up to 260 miles per hour, pretending to simulate the flying conditions of an aircraft. Bowden [1956] presented measurements of lift, drag, and pitching moment of a NACA 0011 airfoil in icing using two types of pneumatic de-icers, one with spanwise inflatable tubes and the other with chordwise tubes, studying the effects of these systems.

After those studies and incidents, researchers identified that the primary problem, resulting in catastrophic events, was the impact of ice accretion on aircraft performance, especially on aerodynamics. This was contrary to what was believed at the time since the weight accumulated on the aircraft, due to ice accretion, was seen as the main cause of the accidents. Actually, even by modern standards, the extent of the drag increase is far larger than what is acceptable.

Therefore, having noticed that ice accretion had an adverse effect on aerodynamic performance, during the 1970s and 1980s there was a push to experimentally characterize its effects through wind tunnels and flight tests. To study ice accretion on a wing, Lozowski et al. [1983a] performed a simulation and later on accomplished a wind tunnel experiment, Lozowski et al. [1983b], in a cylinder, concluding that rotating cylinder icing is fundamentally different of no-rotating cylinder icing as there is not rotational symmetry of the ice accretion about the axis of rotation. This study also characterized dry and wet accretion in a cylinder. In the same year, MacArthur [1983] developed a mathematical model capable of predict, with some level of accuracy, especially for low speed situations, the shape of several glaze and rime ice accretions. Additionally, Olsen and Walker [1986] through close-up movies, that were taken of the icing process at several positions along the surface of a small airfoil for a range of airspeeds, air temperatures, and cloud conditions, concluded that, at the time, the physical model available for ice accretion needed significant modification at different aircraft airspeeds.

With the studies presented, it was concluded that the airfoil/wing parameters such as pressure, lift, drag, pitching moment coefficient and the stall behavior were directly affected by ice accretion. This implied that due to the increased drag, caused by icing, it was necessary more thrust to maintain a certain flight level, increasing fuel consumption, and reducing the cruising speed at certain altitude since the aircraft was flying out of its optimal point. However, this was not the pretended solution for obvious reasons. Therefore, the necessity of accounting either for the geometry of the ice shape or the airfoil/wing geometry, when examining the icing phenomenon became obvious.

Even so, several gaps in the knowledge of how dangerous ice actually was, were found in

the mid-1990s. This was directly related to the 1994 ATR-72 accident in Roselawn, Indiana, of American Eagle Flight 4184, which initiated much of the effort towards the prevention of future accidents, as noticed on NTSB [1996] [6]. As a consequence, the icing community began to realize that studying simple airfoil geometries was not enough to ensure a comprehensive understanding of the phenomena. For instance, Hansman et al. [1993] performed a close-up analysis of aircraft ice accretion in which various ice formation regimes were studied by examining high magnification video observations. Taking advantage of the computational evolution, Kind et al. [1998] performed an experimental and computational simulation of in-flight icing phenomenon. In this study, a considerable number of recommendations, for future works, was outlined.

At the beginning of the century, the scientific community started synthesizing icing research and increased the investigation developed in this area. Hossain et al. presented in 2003 the concept of envelope protection. This work was based in a open and closed loop envelope protection algorithm to ensure the safe operation of an iced aircraft during both manual and autopilot modes of flight. Fortin et al. [2006] presented a thermodynamic model in which a numerical simulation of ice accreted on an airfoil surface, in wet and dry regimes, with an improved roughness model was suggested. In 2008, Cao et al. carried out a numerical simulation of rime ice accretion on an airfoil using an Eulerian method, in which several conclusions were drawn, about ice shapes from the investigation on a NACA 0012 airfoil. For instance, the most important conclusion was that ice shapes vary depending on the angle-of-attack and that ice accretion time, and the MVD of the droplets has considerable effects on the ice accretion.

To study ice adhesion, at the droplet scale, Blake et al. [2015] suggested a model that simulated the impact and solidification of a supercooled water droplet on a cooled substrate. This study assumed that the nucleation phase occurred instantaneously. In the same year, Bilodeau et al. [2015] presented a conservative Eulerian numerical approach for modeling post-impact SLDs undergoing splashing and bouncing on aircraft surfaces and concluded that, even on simple geometries, the re-impingement of splashing and bouncing droplets was not negligible. In 2016, Cao et al. presented insights into rime ice accretion on an aircraft wing and its corresponding effects on the aerodynamic performance, having concluded that an Eulerian approach based on the two-phase flow theory has an advantage in droplet impingement calculation over the Lagrangian one, especially for a three-dimensional complicated configuration.

Liu et al. [2019] presented a three-dimensional aircraft ice accretion model based on the numerical solution of the unsteady Stefan problem for a NACA 0012 airfoil and a GLC-305 swept wing. This study revealed good results when compared with other numerical results

[6] Other accidents such as the Martinair Flight 633 in Ardmore, Oklahoma of a Cessna 208B Caravan on March 2, 1995 (NTSB [1995]), the Comair Flight 3272 in Monroe, Michigan on January 9, 1997 (NTSB [1998]) and the Comair Flight 5054 in West Palm Beach, Florida on March 19, 2001 (NTSB [2002]), strongly contributed to a major awareness of the in-flight icing.

and experimental data existent in the literature. An extensive review of computational methods for aerodynamic analysis of iced lifting surfaces was accomplished by Stebbins et al. [2019]. This study also presented a review for this thematic in which a considerable amount of articles on this topic were addressed.

Nowadays, researchers are observing flow characteristics (i.e., separation and reattachment locations) to possibly manipulate the flow around each wing section and take advantage of its effects, rather than just studying ice formation conditions and its accretion on different geometries. During these last two decades, efforts to develop technologies that prevent ice accumulation, mainly on lifting surfaces, and minimize the negative impacts on aircraft performance, were accomplished. However, according to Zhang and Liu [2016], this process has not received yet, sufficient attention, bearing in mind that most of the actual ice research is uniquely focused on the analysis of lifting surfaces icing.

Gurevich et al. [2020] constitutes an opposite example of the previous statement since it addresses the effect of ice crystals[7] (a different and recently identified type of ice) on engine performance. Ice crystal icing has a dangerous external impact on gas turbine engines, which leads to engine failure. In most cases, ice crystals accumulate in the middle and last stages of the engine booster, changing the geometry of the blades and narrowing the engine core flow-path. Additionally, this study indicates that the best control method under ice crystal icing conditions consists of controlling the engine pressure ratio. Nevertheless, most of the thermodynamic mathematical engine models still need to be improved.

Concerning the behavior of cooling or freezing water droplets, the first studies that addressed this problem remote to the 18th century, being consensual that Fahrenheit [1724] was the one who made the first reference about supercooling. Taylor [1922] made one of the first attempts to mathematically described the dispersion of a fluid particle in stationary subjected to homogeneous turbulence, and understand the relationship between turbulent motion and its dispersive power.

Concerning the dynamics of droplets and their heat and mass transfer, the first studies found in the literature are the ones performed by Ranz and Marshall [1952a,b]. On these articles, through studying the evaporation of droplets, the confirmation of the analogy between heat and mass transfer was achieved, as well as the definition of a correlation between the Nusselt and Sherwood numbers in terms of Reynolds, Schmidt, and Prandtl numbers, for the convective heat and mass transfer coefficients. In the same year, Hughes and Gilliland [1952] developed correlations considering the effect of acceleration on drag, equilibrium distortion, or oscillations, from prolate to oblate spherical shapes. This study emphasized the internal circulation phenomenon caused by skin friction.

In the following year, Messinger [1953] presented a complete analysis for the temperature

[7]Ice crystal icing of a gas turbine engine, in contrast to classical icing, can occur in a cruise at an ambient temperature 10 °C to 20 °C.

of an unheated surface in icing conditions considering several significant regimes as a function of airspeed, altitude, ambient temperature, and liquid water content. In the same research line, Langham and Mason [1958] performed an extensive review about the heterogeneous and homogeneous nucleation of supercooled water. In the same year, Mason [1958] reported some considerations about the supercooling and nucleation of water and addressed heterogeneous nucleation, considering foreign particles in the water.

A computational study of the evaporation rates of pure liquid droplet sprays was performed by Dickinson and Marshall Jr. [1968]. This study drawn up three distinct relations: the droplet's mean diameter versus size distribution, initial drop velocity versus air temperature, and, finally, air velocity versus droplet temperature.

A study of heat and mass transfer of freely falling droplets was performed by Yao and Schrock [1976] in which, based on the assumption of negligible internal thermal resistance, an empirical transient correction factor was applied to the Ranz-Marshall studies (1952a and 1952b). In the following year, Chen and Trezek [1977] studied the influence of the heat transfer coefficient, local wet bulb temperature, and the droplet size distribution function on the thermal performance of sprays by applying a weighting factor to account for local temperature and humidity variations within a field of a spray. Zarling [1980] performed a theoretical and numerical analysis of a system of droplets in free fall to evaluate the variations in the humidity ratio, enthalpy, and temperature of the surrounding air and the droplets.

In 1989, Miyawaki et al. proposed a three-step freezing model applied to semi-infinite and finite cases, covering the effects of supercooling and the temperature-dependence of the fraction of frozen water present. This work created a universal numerical model for the freezing of food materials. In 1993, Epstein and Fauske proposed an integral method to study the combined effects of interface solidification kinetics and heat conduction on the solidification rates within highly supercooled refractory material droplets losing their heat by surface radiation and convection. These two papers constituted a great effort to physically modulate the phenomenon of supercooled water droplets. In the same year, Alexiades and Solomon [1993] systematized the numerical modeling of melting and freezing processes.

Elghobashi [1994], considering the advances on computational power, performed an overview of the challenges and progress associated with the task of numerically predict particle-laden turbulent flows. Shirolkar et al. [1996] studied fundamental aspects of modeling turbulent particle dispersion in dilute flows. Additionally, Gouesbet and Berlemont [1999] reviewed Eulerian and Lagrangian approaches for predicting the behavior of discrete particles in turbulent flows. A comparison between theoretical results and experimental data was also performed, being possible to conclude that both approaches were suitable for the modeling purpose.

An experimental study and numerical modeling for the crystallization process of water droplets was performed by Strub et al. [2003], obtaining a close agreement between numerical data and experimental data. Similarly, Hindmarsh et al. [2003] performed an experimental analysis for the temperature transition of a suspended freezing water droplet and developed a numerical model that predicted a four-stage supercooling process. With similar objectives, Tabakova et al. [2009] developed an analytical and numerical model (based on a three step model) to estimate the freezing time of a suspended supercooled droplet in airflow on a two-step freezing process. In this study, the droplet was assumed to be spherical and, an asymptotic solution was developed for small Stefan numbers. For arbitrary Stefan numbers, a numerical solution based on the enthalpy method was implemented.

Tanner [2011] performed a droplet freezing and solidification study in which a four-stage freezing model was presented. Additionally, a three-stage model validation was accomplished considering a single cocoa butter droplet and a cocoa butter spray. Zhang and Liu [2016] carried out a study about the effect of droplet size and the impact on thermodynamics for a supercooled large droplet in aircraft icing. This study concluded that the droplet size plays an important role in the rapid-freezing characteristics during the impact process, having described parameters that influence this phenomenon. Gupta systematized in 2017 the basic concepts, modeling and analysis with quasi-analytical solutions and methods of The Classical Stefan Problem.

In 2018, Janjua et al. developed a simple one-dimensional energy balance model to show how the freezing fraction parameter of a droplet increases with a decrease in atmospheric temperature. This method incorporated both rime and glaze ice and showed a promising comparison with experimental data available in the literature.

Meng and Zhang [2020] carried out a study that considers the dynamic propagation of ice-water phase front in a supercooled water droplet. In this article, a three-dimensional theoretical model was proposed accounting for crystallization kinetics during heat transfer, which allowed to detail the entire freezing process of a supercooled water droplet, including a phase that usually is neglected (recalescence stage). In the same year, Akhtar et al. [2020] developed and validated a semi-analytical framework for freezing of droplets considering heterogeneous nucleation and non-linear interface kinetics. Myers et al. [2020] addressed a Stefan problem with variable thermophysical properties and phase change temperature for a water droplet on a standard one-dimensional problem.

In addition to what was presented and, considering other areas of interest, like the ones referenced in Chapter 1, a fundamental study of spray freezing and frozen droplets on foods—microstructure was performed by Hindmarsh et al. [2007], accounting for the microstructure of frozen food droplets. This study suggested different means of manipulating the droplet microstructure produced during a spray-freezing process. Samuelsen and Graversen [2019] carried out a study in which ship-icing events off

the coast of Northern Norway were observed concluding that the necessity of developing models that account for the icing on ships. In the pharmaceutics area, Wanning et al. [2015] presented a review on pharmaceutical spray-freeze drying, a technique that requires the generation and freezing of a spray of water droplets. Son and Kim [2020] developed a three-dimensional icing numerical tool for rotating wind turbines since it is an area with recent high interest.

2.6 Numerical modeling efforts

Several approaches have been used to study ice formation and its accretion on aircraft. The most intuitive methods to evaluate aircraft resiliency to ice accretion are wind tunnel and flight testing. Flight tests are the most direct and reliable approach for acquiring iced-aircraft aero-dynamic data, especially, when analyzing various accretion regimes and aircraft locations. According to the nature of ice accretion, flight tests can be classified as natural icing conditions or artificially simulated ice shape conditions. However, the costs of these approaches are relatively high when compared to other methodologies and, it is very difficult to perform some tests in specific aircraft. For example, according to Cao and Chen [2010], in the case of helicopters, it is extremely dangerous and expensive trying to perform flight tests on icing conditions.

Relatively to wind tunnel experiments, the main difficulty is on the dependency of experimental capabilities as, for instance, on reaching a specific Reynolds number. Besides, the complexity of natural icing conditions is difficult to replicate. Apart from that, establishing wind tunnel facilities dedicated to ice investigation requires a substantial investment even considering that after the facilities are laid, the overall cost per test is low. One of the big advantages of this approach is on lowering the risks associated when comparing other methodologies. Similarly with flight tests, wind-tunnel tests are also performed in natural icing conditions or artificially simulated ice shapes.

According to the reasons presented before, it is very difficult, to comprehensively analyze the aircraft flight dynamic characteristics, in all different cases, performing flight tests or wind tunnel experiments. Hence, with technology innovation, computational simulations became a necessary, and eventually essential, tool for the analysis of iced-aircraft flight dynamics. Through these years, especially the most recent decade, numerical simulations turned into a good solution, considering that this method enables the investigation of the entire icing envelope of an aircraft. Since it has a short experimental cycle, it allows to perform different studies maintaining the economical efficiency. The accuracy of the results only depends on the procedures implemented computationally. This numerical methodology only received considerable attention during the last 20 years, even so, it is being implemented, on predicting ice accretion, since the 1980s, as seen in Section 2.5.

The computational tools that model ice accretion, usually, have two main philosophies:

simulate ice accretion and, the ice shapes on any aircraft surface exposed to icing conditions or simulate icing effects and their influence on aircraft performance. Nowadays, several centers are heavily skilled in studying ice accretion and its effects on aircraft. As a consequence of their knowledge, these centers develop software packages that simulate, according to the philosophies presented, the icing phenomenon. In Table 2.1, different examples of computational tools, and the entities responsible for their development, are presented. Moreover, other tools were and are being developed by individual researchers, trying to address small problems that sometimes are not contemplated on other packages or need to be detailed, as seen in Section 2.5.

Nevertheless, numerical modeling still faces numerous challenges. It is known that glaze ice is much more complex than rime ice and, thus, much more difficult to simulate computationally, as observed by Cao et al. [2018]. Kind et al. [1998] claimed that this situation is possibly explained because of the unfrozen water present in the impingement zone. On the contrary, rime ice is reasonably well understood and can be adequately simulated for most practical purposes. Besides, according to Kind et al. [1998], analytical icing simulation has been based on a combination of correlations, computational tool, and theoretical models of the icing process and its consequences, being, therefore, a limited cognitive level process that is associated with errors. Therefore, further work in this area needs to be accomplished.

Table 2.1: Computational tools developed, by distinct entities, to simulate the effect of ice accretion on aircraft aerodynamic performance.

Tool	Developer	Country	Reference
LEWICE	NASA's Glenn Research Center's Icing Research Tunnel	USA	Ruff and Berkowitz [1990]
CANICE	The Bombardier Aeronautical Chair at École Polytechnique	Canada	Brahimi et al. [1994]
TRAJICE	DRA - Defence Research Agency (Defence Science and Technology Laboratory, nowadays)	UK	Gent [1990]
MULTIICE-CIRA	CIRA - Italian Aerospace Research Center	Italy	Mingione et al. [1997]
CAPTA-ONERA 2D/3D	ONERA - The French Aerospace Lab	France	Hedde and Guffond [1995]
2D CIRAMIL	CIRA and AMIL - Anti-Icing Materials International Laboratory	International Cooperation	Fortin et al. [2003]
FENSAP-ICE	Ansys, Inc.	USA	Beaugendre et al. [2003]

Chapter 3

Analysis of existing numerical resources

Considering the objectives of this dissertation, it is necessary to evaluate the available capabilities and the existing numerical resources. Section 3.1 briefly introduces the thematic of fluid dynamics and the models used to predict the behavior of discrete particles. Section 3.2 presents the formulation for the continuous phase of the existent computational tool, whereas Section 3.3 presents the formulation for the dispersed phase. The interaction between distinct phases and the procedure to obtain the final solution is addressed in Section 3.4. The discretization of the mathematical model equations and the grid properties are presented in Section 3.5. Section 3.6 discusses the pressure-velocity coupling and presents the method used for this purpose. Section 3.7 clarifies the iterative method used for the resolution of the algebraic systems that were already programmed into the existent tool.

3.1 Introduction

Fluid dynamics is totally defined by the conservation of three quantities (mass, momentum, and energy) inside a fixed control volume, anywhere in a flow domain, with any arbitrary shape and size. These quantities are represented, in total, by five equations which are, consequently, written in the form of a conservation law. These equations determine the behavior of a system without any additional dynamical law. To completely describe all flow phenomena, these equations are supplemented by empirical laws, for the dependence of viscosity and thermal conductivity with other flow variables, and by a constitutive law, defining the fluid nature.

First of all, it is necessary to detail the difference between a fluid particle and a discrete particle, to completely comprehend how the interaction between a water droplet and the surrounding environment is achieved. A fluid particle consists of a macromolecular volume of fluid which is small enough to have average properties equal to the local properties all over its volume. Consequently, any property of the fluid particle is very well represented by a single value for each instant of time and preserves its internal properties longer than the characteristic time of the turbulent flow in which it is immersed.

On the other hand, a discrete particle or contaminant particle has properties that may differ from those of the carrier fluid. Thus, if, for example, the density of the discrete particle is different from that of the fluid, consequently, the particle will not follow all the velocity fluctuations of the carrier fluid because of its different inertia, as will be explained in

Section 3.3. In this dissertation, every time that particle is refereed, the definition of a discrete particle is being used.

To predict the behavior of discrete particles through a reference frame, sometimes on turbulent flows, two different approaches have been reported in the literature as capable of describing the phenomenon. Those formulations are the Eulerian and Lagrangian approaches. Sometimes, these formulations have small variants, however, they usually share the same fundamental principles when used in the field of modeling turbulent particle dispersion. The Lagrangian approach is usually treated as a non-continuum model since the particle is treated discretely, while the Eulerian approach can be denominated as a continuum model.

From a simple point of view, the Lagrangian representation tracks one particle, or a spray, as it moves through the flow field, creating a path in each time step, having as reference the origin and the time elapsed since it started. Therefore, the Lagrangian perspective follows fluid particles, or material points, as they move through the computational domain, resorting to a movable reference frame and considering the instantaneous position and velocity of the particle as functions. Eulerian perspective focuses on a particular point in space recording properties of the fluid elements passing through that point. Hence, the reference frame is stationary, and the particles pass through fixed differential control volumes. The characteristics of the particulate phase are obtained by solving partial differential equations in a given coordinate system.

When dealing with low mass-loading ratio particles, the influence of these particles on the surrounding environment is small and, for that reason, it is not necessary to account for that interaction. Therefore, from the mathematical point of view, this phenomenon can be approached as a one-way coupling methodology. However, when the particle's mass-loading ratio increases, it is necessary to consider the mutual influence between the particles on the surrounding environment. Usually, and according to Gouesbet and Berlemont [1999], we mathematically resort to a two-way coupling model, which considers that the properties of the carrier fluid are modified by the presence of the dispersed phase, accounting for the exchange of mass, momentum, and energy between the two phases. The transport of particles, which are distinguishable from the phase in which are involved (which can exhibit turbulent motion), is described as turbulent particle dispersion. Most of the time, and if the problem requires, turbulence modeling is simultaneously implemented to the models described previously.

When there is more than one distinct phase of interest involved in a problem, for instance, in water droplets on a free fall, it is necessary to consider a multiphase system. In the previous example, two distinct phases are observed: the surrounding gas, which can be dry or humid air, and the water droplets. These phases are usually denominated as the dispersed phase or the particle phase; and the continuous or carrier phase.

In accordance with Shirolkar et al. [1996], for a dilute concentration of particles, the continuum assumption, in which the particles are considered as a continuum mean and under an Eulerian reference frame formulation, is used. However, as mentioned by the same author, this methodology has its limitations in modeling such flows. Hence, in dilute two-phase flows, it is common to follow the particle trajectory in a Lagrangian reference frame and solve the surrounding environment resorting to an Eulerian reference frame. This was the methodology that was already implemented on the in-house computational tool.

3.2 Continuous or carrier phase

Being mindful that in this particular case, considering a macroscopic length scale, the molecular structure of matter and molecular motion are ignored, the fluid will be regarded as a continuum mean justifying the phase name. Eqs. (3.1), (3.2) and (3.3) represent the mathematical statements of the conservation laws of physics, which state that the mass of fluid is conserved, the momentum change rate equals the sum of the forces on a fluid particle, Newton's second law of motion, and energy is also conserved.

Therefore, these equations are written for a stationary, viscous, Newtonian fluid, incompressible flow under a conservative form, to include source terms that consider mass, momentum, and energy. These consist of scalar functions that are added to the conservation laws to account for certain interactions. Apart from the continuity, momentum and energy, the vapor mass fraction is also represented as a mean flow property. The turbulent quantity equations (turbulence kinetic energy and the dissipation rate of turbulence kinetic energy) are, as well, considered. Eq. (3.1) represents the continuity equation, Eq. (3.2) the momentum equation, and Eq. (3.3) the energy equation. This set of equations constitute the RANS.

$$\frac{\partial}{\partial X_i}\left(\rho \overline{U}_i\right) = \overline{S}_\rho \quad (3.1)$$

$$\frac{\partial}{\partial X_j}\left(\rho \overline{U}_i \overline{U}_j\right) = -\frac{\partial \overline{p}}{\partial X_i} + \frac{\partial}{\partial X_j}\left(\mu \frac{\partial \overline{U}_i}{\partial X_j} - \rho \overline{U_i' U_j'}\right) + \overline{S}_{U_i} \quad (3.2)$$

$$\overline{U}_j \frac{\partial}{\partial X_j}\left(\rho \overline{U}_j \overline{T}\right) = \frac{\partial}{\partial X_j}\left(\frac{\mu}{\mathrm{Pr}} + \frac{\mu_t}{\mathrm{Pr_t}}\right)\left(\frac{\partial \overline{T}}{\partial X_j}\right) + \overline{S}_T \quad (3.3)$$

Regarding the nomenclature previously used, it is important to notice that $\overline{U_i' U_j'}$ constitute additional turbulent stresses, usually called Reynolds stresses. $\overline{S}_\rho$ represents the mass source term produced by the cooling process, $\overline{S}_{U_i}$ the momentum source term, and $\overline{S}_T$ the energy source term. $\mathrm{Pr_t}$ and μ_t correspond, respectively, to the turbulent Prandtl number and the turbulent dynamic viscosity.

Considering the momentum source term, to exemplify how source terms are structured, this term has two distinct contributions, as seen in Eq. (3.4). The first contribution, $\overline{S}_{U_i,g}$ is a result of gas momentum flux. The second contribution, $\overline{S}_{U_i,d}$, results from the interaction between the two phases, without any phase change, and depends on the interaction forces between the fluid and the particles. These source terms account for the influence of the gas phase over the particles in the dispersed phase.

$$\overline{S}_{U_i} = \overline{S}_{U_i,g} + \overline{S}_{U_i,d} \quad (3.4)$$

Regarding the transport physics of a certain quantity in a fluid flow, it is necessary to consider the definition of flux and how it is generated. By definition, a flux consists of a fundamental quantity associated with a conserved flow variable. This parameter is translated as the amount of a quantity crossing the unit of surface per unit of time, being, therefore, a directional quantity with a direction and an amplitude.

The fluxes are generated from two contributions: a contribution due to the advective transport of the fluid and a contribution due to the molecular agitation (diffusion), which is present even when the fluid is at rest. Advection expresses the transport of the considered quantity by the flow, having a directional behavior and, as a consequence, does not exist in a fluid at rest. On the other hand, diffusion translates the effects of molecular collisions and has an isotropic behavior existing even in a fluid at rest. Advection is generally non-linear when the flow velocity depends on the transported variable, whereas diffusion is generally linear for constant fluid velocities.

To generalize the mean flow and turbulent quantity equations, for all variables, it was considered a general variable property per unit volume, ϕ, which can stand for all the scalar variables, enabling the reduction to a generic advective-diffusive conservation equation. Eq. (3.5) is the result of the process explained previously, where Γ corresponds to the effective diffusion coefficient for quantity ϕ. This equation is usually called transport equation.

$$\frac{\partial\left(\rho\phi U_i\right)}{\partial X_i} = \frac{\partial}{\partial X_i}\left[\Gamma_\phi \frac{\partial \phi}{\partial X_i}\right] + \overline{S}_\phi \quad (3.5)$$

In Eq. (3.5), $\overline{S}_\phi$ represents the general source term which, can be divided into two distinct contributions. The first term, $\overline{S}_{\phi,g}$, represents the gas contribution and, the second one, $\overline{S}_{\phi,d}$, the source term of the particle. Eq. (3.6) clarifies the terms that constitute the general source term.

$$\overline{S}_\phi = \overline{S}_{\phi,g} + \overline{S}_{\phi,d} \quad (3.6)$$

To predict the turbulent particle dispersion, several factors have to be taken into account. The particle size with respect to the length scales of turbulence (eddy sizes) in the fluid, the relative density between the particle and the fluid, the fluctuating fluid velocity surrounding the particle, the particle relaxation time, which depends on the particle density, diameter, and Reynolds number, as well as the fluid viscosity and the drag coefficient and, at last, the crossing trajectory effect phenomena, which depends on the characteristic eddy size, eddy lifetime, and particle drift velocity require careful attention. Current popular methods for predicting the fluid phase and its turbulence properties include algebraic formulas, such as the constant eddy viscosity, the mixing-length models, or other turbulence models.

An eddy-viscosity model, known as the $k-\varepsilon$ model and initially developed by Launder and Spalding [1974], is used to model turbulence in this computational tool. This model is solved by resorting to the time-averaged (Reynolds average) Navier-Stokes equations, with several modeling assumptions. As a consequence of this method, which separate turbulent fluctuations from the mean-flow, a non-linearity appears and these new variables create a Turbulence Closure Problem.

In order to approximate $\overline{U_i' U_j'}$, Eq. (3.7) gives a linear relationship between the Reynolds stresses and the rate of strain, for an incompressible flow. This equation resorts to the Boussinesq eddy viscosity assumption, which states that the momentum transfer caused by turbulent eddies is modeled with an eddy viscosity. The closure to the Reynolds stresses problem is obtained by developing transport equations for the turbulent kinetic energy, k and its dissipation rate, ε.

$$\overline{\rho}\,\overline{U_i' U_j'} = -\mu_t\left(\frac{\partial \overline{U}_i}{\partial X_j} + \frac{\partial \overline{U}_j}{\partial X_i}\right) + \frac{2}{3}\overline{\rho} k \delta_{ij} \quad (3.7)$$

Eqs. (3.8), (3.9), (3.10) and (3.11) represent, respectively, the Kronecker delta, the turbulent kinetic energy of the flow, the turbulent dynamic viscosity, which is a space and time-dependent quantity, that depends entirely upon the local turbulent characteristics of the flow, and the turbulent kinetic energy production term.

$$\delta_{ij} = \begin{cases} 1, & \text{if } i = j, \\ 0, & \text{if } i \neq j. \end{cases} \quad (3.8)$$

$$k = \frac{1}{2} \times \left(u'^2 + v'^2 + w'^2 \right) \quad (3.9)$$

$$\mu_t = C_\mu \rho \frac{k^2}{\varepsilon} \quad (3.10)$$

$$G = \mu_t \left[\frac{\partial \overline{U}_i}{\partial X_j} + \frac{\partial \overline{U}_j}{\partial X_i} \right] \frac{\partial \overline{U}_i}{\partial X_j} \quad (3.11)$$

By replacing ϕ, on Eq.(3.5), for the corresponding variable for the continuity, momentum, enthalpy, vapor mass fraction, turbulent kinetic energy, and its dissipation, it is possible to obtain special forms of the partial differential equations, which consist on elliptic differential transport equations. Table 3.1 systematically represents these equations.

Table 3.1: Terms in the general form of the elliptic differential equation, adapted from Gouesbet and Berlemont [1999] and Sommerfeld [1998].

ϕ	$\overline{S}_{\phi,g}$	$\overline{S}_{\phi,d}$	Γ_ϕ
1	-	$\overline{S}_{\rho,d}$	-
U_i	$-\frac{\partial}{\partial X_i}\left(p+\frac{2}{3}k\right)-\frac{\partial}{\partial X_j}\frac{2}{3}\mu_t\frac{\partial \overline{U}_j}{\partial X_i}+\rho g_i$	$\overline{S}_{U_i,d}$	$\mu+\mu_t$
T	0	$\overline{S}_{T,d}$	$\frac{\mu}{\mathrm{Pr}}+\frac{\mu_t}{\mathrm{Pr_t}}$
Υ	0	$\overline{S}_{\Upsilon,d}$	$\frac{\mu}{\mathrm{Sc}}+\frac{\mu_t}{\mathrm{Sc_t}}$
k	$G-\rho\varepsilon$	$\overline{S}_{k,d}$	$\mu+\frac{\mu_t}{\sigma_k}$
ε	$C_{\varepsilon 1}\frac{\varepsilon}{k}G-C_{\varepsilon 2}\frac{\varepsilon^2}{k}G$	$\overline{S}_{\varepsilon,d}$	$\mu+\frac{\mu_t}{\sigma_\varepsilon}$

Launder and Spalding [1974], after examining free turbulent flows, suggested several constants to model turbulence. These constant are presented in Table 3.2 and were determined by comprehensive data fitting for a wide range of turbulent flows. As observed previously, an obvious limitation of this eddy-viscosity model is that it is based on the underlying assumption that μ_t is isotropic and, consequently, the ratio between Reynolds stress and mean rate of deformation is the same in all directions.

Table 3.2: Values of the constants for the eddy-viscosity model $k-\varepsilon$, from Launder and Spalding [1974].

C_μ	$C_{\varepsilon 1}$	$C_{\varepsilon 2}$	$C_{\varepsilon 3}$	σ_ε	σ_ε	$\mathrm{Pr_t}$	$\mathrm{Sc_t}$
0.09	1.44	1.92	1.1	1.0	1.3	0.6	0.85

3.3 Dispersed or particle phase

As stated previously, when using a Lagrangian particle dispersion model, particles are treated as discrete objects, and their motion is tracked as they move through the flow field. Consequently, and according to Shirolkar et al. [1996], it is possible to account for the non-continuum behavior of particles and particle history effects. When resorting to the Lagrangian model, two different approaches are used to obtain the particle trajectory, which is one of the biggest problems of this approach.

The first methodology consists of developing a stochastic model for Lagrangian velocities by assuming that particles behave like fluid particles and the molecular diffusion can be neglected. However, its application is limited to passive particles, which behave like the surrounding fluid, in high Reynolds number flows. On the other hand, in the second methodology, the particle trajectories of representative samples are obtained by solving the particle momentum equation through the Eulerian fluid velocity field, which is acquired by solving the averaged Navier-Stokes equations.

The existent computational tool has implemented the second methodology due to drastic differences between the two phases selected. Therefore, a particle trajectory is determined by solving its equation of motion. This equation is obtained resorting to Newton's Second Law of Motion considering that all the forces acting on a particle immersed in a turbulent flow are mathematically quantified. These forces are described into four distinct categories:

- Forces that act on a particle due to the motion of particle;
- Forces that act on a particle due to the motion of the surrounding fluid;
- Forces that act on a particle irrespective of the particle motion or immersion in a flowing fluid (body forces; for example, gravity or electromagnetic forces);
- Forces that act on any object immersed in fluid irrespective of the particle or fluid motion (for example, the buoyancy forces).

Considering a spherical particle that accounts for all the four types of forces, the mathematical expression for the equation of motion is given by Eq. (3.12). Concerning the nomenclature involved on Eq. (3.12), it is important to notice that K stands for the Basset force constant, M to the virtual mass force constant, and ω to the angular momentum of the particle. ξ_{ijk} consists in a third-order tensor and it is defined by Eq. (3.13). $n_{1;j}$ is a unit vector in the direction of the particle angular momentum vector. The term on the left represents the inertia force. On the right, by order, are represented the steady-state draft force, the Basset force, the virtual mass force, the Magnus force, the body force due to gravity, and the bouncy force.

$$\begin{aligned} m_d \frac{dU_{i,d}}{dt} =& 3d\pi\mu_g \frac{\mathrm{Re_d}}{24} C_D \left(U_{i,g} - U_{i,d}\right) + Kd^2\sqrt{\pi\rho_g\mu_g} \int_{t_0}^{t} \frac{\frac{d}{dt}\left(U_{i,g} - U_{i,d}\right)}{\sqrt{t-t'}}\, dt' \\ &+ M\rho_d \frac{\pi}{6} d^3 \frac{d}{dt}\left(U_{i,g} - U_{i,d}\right) + \frac{\pi}{8}\rho_g d^3 \omega_d \xi_{ijk} n_{1;j} \left(U_{i,g} - U_{i,d}\right) \\ &+ m_d g_i - \rho_g \frac{\pi}{6} d^3 g_i \end{aligned} \tag{3.12}$$

$$\xi_{ijk} = \begin{cases} 1, & \text{if } ijk = 123, 231 \text{ or } 312, \\ -1, & \text{if } ijk = 132, 213 \text{ or } 321, \\ 0, & \text{for all other cases.} \end{cases} \tag{3.13}$$

Concerning the forces involved, the Basset force results from the transitory nature of the

particle's boundary layer and is mainly influenced by the history of the particle trajectory. The virtual mass force is a consequence of the difference in acceleration between the fluid and the particle, being usually present when there is a significant difference in the fluid and particle densities. The Magnus force results when a rotating particle is subjected to a non-rotating fluid. An additional force due to the lift force experienced by a small spherical particle moving in a very viscous liquid, called Saffman force, could be considered. However, according to Shirolkar et al. [1996], its effect is only known in uniform shear flows and, for that reason, it is not considered in this case. The steady-state force is the most important force acting on a particle and, different functions involving the relative velocity are used to model it. The one used on Eq. (3.12) reflects the variation of the drag coefficient with the relative velocity.

Relatively to the particle's nature, and their transport on flows, it is possible to subdivide this phenomenon into three distinct subclasses: suspensions, bubbly flows, and droplet flows. For this specific case, droplet flows was the subclass chosen considering that the dispersed phase is assumed as a dilute particle laden flow problem. This approach allows us to consider that various particle-particle interactions, such as collisions and coalescence, can be neglected. In addition to these simplifications, only steady-state mechanisms for particle dispersion are considered, neglecting the contributions of unsteady large-eddy phenomena to the turbulent dispersion of small particles. The simplified particle motion equations for a three-dimensional Cartesian coordinates system, which neglects the Basset, virtual mass, Magnus, Saffman, and buoyancy forces, is written in terms of the particle relaxation time and its differential form on Eqs. (3.14) and (3.15).

$$\frac{dX_{i,d}}{dt} = U_{i,d} \quad (3.14)$$

$$\frac{dU_{i,d}}{dt} = \frac{1}{\mathrm{T}_d}\left(U_{i,g} - U_{i,d}\right) + g_i \quad (3.15)$$

Opting for a dispersion model based on eddy lifetime concept, which is later explained, and after recognizing that Eqs. (3.14) and (3.15) are first order, non-homogeneous, non-linear differential equations it is possible to obtain Eqs. (3.16) and (3.17). These equations correspond to the new particle location and the velocity, respectively, and result of analytically solving the differential equations presented before over small time steps, Δt, in which the instantaneous fluid velocity and the droplet relaxation time are assumed to be constant. In this way, a three-dimensional trajectory of the particle for each time step is obtained. These expressions are commonly used in Lagrangian models to generate particle

trajectories.

$$X_{i,d}^{NEW} = X_{i,d}^{OLD} + \frac{\Delta t}{2}\left(U_{i,d}^{NEW} + U_{i,d}^{OLD}\right) \quad (3.16)$$

$$U_{i,d}^{NEW} = U_{i,g} + \left(U_{i,d}^{OLD} - U_{i,g}\right)\exp^{-\frac{\Delta t}{\mathrm{T}_d}} + g_i \mathrm{T}_d \left(1 - \exp^{-\frac{\Delta t}{\mathrm{T}_d}}\right) \quad (3.17)$$

Analyzing Eqs. (3.16) and (3.17), it is possible to determine the existence of two unknown variables: Δt and T_d (particle relaxation time).

To find the particle relaxation time, when examining the motion of particles inside a carrier fluid is necessary to account for two distinct parameters: the particle inertia and the particle free-fall velocity. The droplet inertial effect justifies why a dense particle has a less fluctuating velocity relative to the fluid fluctuations since it does not have a passive behavior. Hence, this effect characterizes the reduction in the particle root mean square fluctuating velocity and is characterized by a time scale. Eq. (3.18) represents the particle relaxation time, defining the response rate of a particle acceleration to the relative velocity between the particle and the carrier fluid.

$$\mathrm{T}_d = \frac{24\rho_d d^2}{18\mu C_D \mathrm{Re_d}} \quad (3.18)$$

The droplet drag coefficient is represented by Eq. (3.19). This parameter was estimated according to experimental data fitting reported by Crowe et al. [2011] and uses the Reynold number (described in Eq. (4.8)), which is widely accepted for dilute flows or a single particle in a turbulent flow.

$$C_D = \begin{cases} \dfrac{24}{\mathrm{Re_d}} \times \left(1 + 0.15\mathrm{Re_d}^{0.687}\right), & \text{if } \mathrm{Re_d} < 1000 \\ 0.44, & \text{if } \mathrm{Re_d} \geq 1000 \end{cases} \quad (3.19)$$

Therefore, it is now necessary to find the integration time step needed for Eqs. (3.16) and (3.17). This parameter is considered in the literature as the key element when resorting

to Lagrangian particle dispersion models. Firstly, it is important to consider that turbulence models, such as the $k-\varepsilon$ model, provide the time-averaged Eulerian fluid velocity, whereas the particle momentum equation requires the instantaneous fluid velocity at the particle location. To estimate the fluctuating component of the fluid velocity at every particle location, as it moves in discrete time steps through the computational domain, it is necessary to resort to stochastic methods. In this dissertation, a SSF model was used. This technique involves random sampling of the fluctuating fluid velocity from certain known distributions.

Knowing that turbulence is an inherent phenomenon when examining the motion of particles inside a carrier fluid, it is imperative to understand how eddy-particle interactions work. The SSF model estimates the fluctuating component of fluid velocity, considering a concept which states that the particle interacts with a succession of eddies as it moves along the computational domain. To fully characterize an eddy, it is necessary to evoke three distinct parameters: a velocity (fluctuating), a time scale (lifetime), and a length scale (size). The eddy size and lifetime are obtained from the local turbulence properties (k and ε) along the particle trajectory. The fluctuating fluid velocity that corresponds to a particular eddy is randomly sampled from a Probability Density Function (PDF) obtained from local turbulence properties. This fluctuating fluid velocity PDF, at each particle location, is assumed to be Gaussian, having a zero mean value and standard deviation of $\sqrt{2k/3}$.

Relatively to the eddy size and the eddy lifetime, needed at each particle location to determine the next interaction time, these are obtained, as previously said, resorting to the local turbulence properties using the Kolmogorov time and length scales for isotropic flows. These scales correspond to the smallest eddy size found in a given turbulent flow and the time scale associated with this eddy, being represented by Eqs. (3.20) and (3.21), respectively. However, for some particular cases, is possible, resorting to isotropic SSF models, to use different expressions for these two turbulence scales. Eq. (3.22) represents a general expression for the turbulent eddy lifetime time scale and, Eq. (3.23) represents a general expression for the turbulent length scale or the characteristic eddy size, where a and b are two dependent constants and the ratio between them, respectively, equals $\sqrt{1.5}$. These constants were determined, either by scaling analysis or experimental data and, can be found in the literature. Shirolkar et al. [1996] summarized the time and length scales used in isotropic SSF models.

$$\tau_{kol} = \left(\frac{\nu_t^3}{\varepsilon}\right)^{1/4} \quad (3.20)$$

$$l_{kol} = \left(\frac{\nu_t}{\varepsilon}\right)^{1/2} \quad (3.21)$$

$$\tau_e = a\frac{k}{\varepsilon} \approx 0.2\frac{k}{\varepsilon} \quad (3.22)$$

$$l_e = b\frac{k^{3/2}}{\varepsilon} \approx {C_\mu}^{3/4}\frac{k^{3/2}}{\varepsilon} \quad (3.23)$$

Another parameter that will ultimately affect the time step chosen is a consequence of the crossing trajectory effect. This is translated by the eddy transit time, which is represented by Eq. (3.24). This parameter is interpreted as the minimum time a particle would take to cross an eddy with a characteristic dimension, l_e.

The necessity of accounting for this parameter arises from the possibility of a particle remaining trapped inside an eddy for the entire lifetime of that eddy or prematurely migrate from one eddy to another before the decay, due to turbulence of the original eddy. This premature migration usually is due to the significant free-fall velocity of the particle under consideration. In conclusion, if the minimum crossing time calculated is smaller than the eddy lifetime, the particle would jump to another eddy. The parameter U_{drift} represents the particle drift velocity and, is used to determine the time a particle would take to cross a given eddy.

$$\upsilon_e = \frac{l_e}{\parallel \overrightarrow{U}_{drift} \parallel} \quad (3.24)$$

It is important to notice that the drift velocity, during the next time step, needed in Eq. (3.24) is not known in advance, being, for that reason, necessary a different equation to obtain υ_e. A different expression for the eddy transit time, based on a simplified and linearized equation of motion for a particle in a uniform flow, is also recommended on the literature and, for that reason, presented in Eq. (3.25).

$$\upsilon_e = -\mathrm{T}_d \ln\left(1 - \frac{l_e}{\mathrm{T}_d \parallel U_{i,g} - U_{i,d} \parallel}\right) \quad (3.25)$$

Examining mathematically Eq. (3.25), it is concluded that there is no solution when the characteristic eddy size is greater than the fluid-particle relative velocity multiplied by the relaxation time. This fact is a consequence of the linearized stopping distance of the particle being smaller than the eddy size and, for that reason, the particle is trapped by the eddy. In this case, the interaction time will be the eddy lifetime. Therefore, the particle will interact with a particular eddy for a time, which is the minimum of the eddy lifetime and the eddy transit time, considering that the fluctuating velocity associated with a particular eddy is assumed to be constant over the interaction time. The time step selected is the eddy-particle interaction time (t_{int}) and is represented by Eq. (3.26).

$$t_{int} \approx \Delta t = \min\left(\tau_e, \upsilon_e\right) \quad (3.26)$$

Therefore, ultimately, it is said that through knowing the interaction time and randomly sample the fluctuating fluid velocity, assuming it to be constant over this time, it is possible to solve Eqs. (3.16) and (3.17) to obtain the particle trajectory. At the end of each time step, a new fluctuating fluid velocity is sampled from a new PDF, generated by using the local turbulence properties. Consequently, the next interaction time is determined by the local properties at the new particle location.

The contribution of the dispersed phase to complete the terms, in the general form, of the elliptic differential equation, Eq. (3.5), is given by the particles source terms $\overline{S}_{\phi,d}$. These terms are calculated for each Eulerian cell of the continuous phase and can be divided into two parts, as shown in Eq. (3.27). $\overline{S}_{\phi,ipt}$ specifies the source term due to inter-phase transport, while $\overline{S}_{\phi,c}$ deals with the transfer caused by the cooling phenomenon.

$$\overline{S}_{\phi,d} = \overline{S}_{\phi,ipt} + \overline{S}_{\phi,c} \quad (3.27)$$

Table 3.3 presents both terms, which, when summed, constitute the particle source terms. When these terms are attached to the data of Table 3.1, complete the terms, in the general form, of the elliptic differential equation, Eq. (3.5).

Table 3.3: Terms in the general form of the elliptic differential equation, adapted from Gouesbet and Berlemont [1999] and Sommerfeld [1998].

ϕ	$\overline{S}_{\phi,d}$	$\overline{S}_{\phi,ipt}$	$\overline{S}_{\phi,c}$
1	$\overline{S}_{\rho,d}$	0	$\sum_k \frac{\dot{m}_k N_k}{V_{ij}}$
U_i	$\overline{S}_{U_i,d}$	$-\sum_k \frac{\dot{m}_k N_k}{V_{ij}} \left[\left(U_{i,k}^{t+\Delta t} - U_{i,k}^{t}\right) g_i \Delta t\right]$	$\sum_k \frac{\dot{m}_k N_k U_{i,k}}{V_{ij}}$
T	$\overline{S}_{T,d}$	$-\sum_k \frac{N_k}{V_{ij}} \left(L_{ph}\dot{m}_k + Q_{rel}\right)$	$\sum_k \frac{\dot{m}_k N_k}{V_{ij}} c_{p,d}\left(T_k\right) T_k$
Υ_a	$\overline{S}_{\Upsilon_a,d}$	0	0
Υ_w	$\overline{S}_{\Upsilon_w,d}$	0	$\frac{\sum_k \dot{m}_k N_k}{V_{ij}}$
k	$\overline{S}_{k,d}$	$\overline{U_j S_{U_j,ipt}} - \overline{U}_j \overline{S}_{U_j,ipt}$	$\overline{U_j S_{U_j,c}} - \overline{U}_j \overline{S}_{U_j,c} + \frac{1}{2}\overline{U}_j \overline{U}_j \overline{S}_\rho - \frac{1}{2}\overline{U_j U_j S_\rho}$
ε	$\overline{S}_{\varepsilon,d}$	$C_{\varepsilon 3}\frac{\varepsilon}{k}\overline{S}_{k,ipt}$	$C_{\varepsilon 3}\frac{\varepsilon}{k}\overline{S}_{k,c}$

3.4 Solution procedure - interaction between the continuous and dispersed phases

As reported by Shirolkar et al. [1996], the most popular method for modeling dilute two-phase flows is to consider two single-phase events occurring simultaneously, with or without accounting for the interaction with the other phase. To consider the exchange of mass, momentum, and energy between the two phases in dilute flows, both phases have to be coupled and, for that reason, the effects between the continuous and dispersed phases are included.

The iterative procedure used on the existent computational tool, to obtain the numerical results pretended, is divided into four distinct modules. The implemented procedure follows the presented line-up to obtain a converged solution for both phases. Additionally, this iterative procedure is schematized in Figure 3.1, where it is possible to see the four distinct modules and their sub-consequent submodules.

1. Establishment of the initial conditions by resetting all projects previously executed and the source terms used on the transport equations.

2. Mesh generation to represent the computational domain of the problem.

3. Definition of the droplets, or spray, characteristics.

4. Initialization of the continuous phase calculated disregarding the source terms of the dispersed phase (source terms of the discrete phase equal to zero), obtaining a converged solution for the gas flow field.

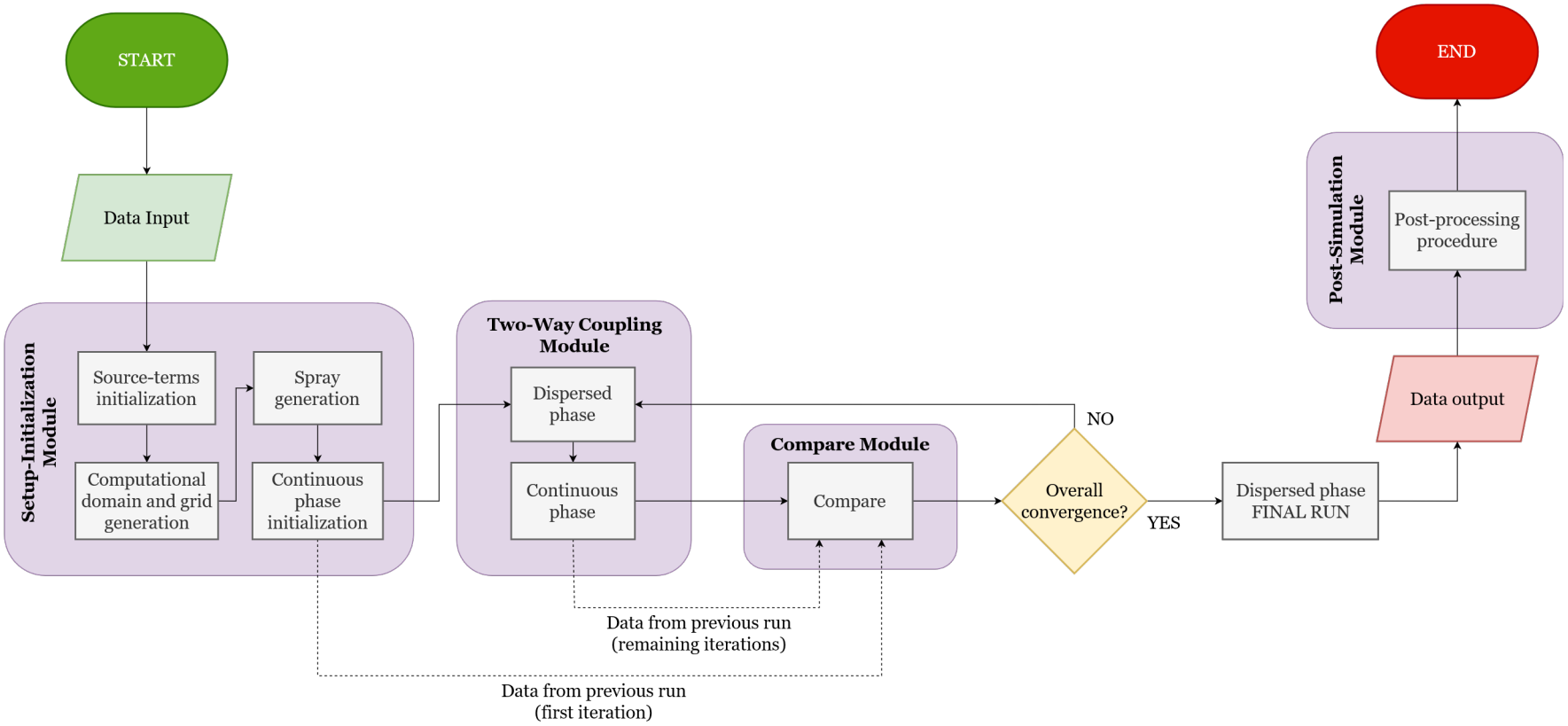

Figure 3.1: Flowchart of the iterative procedure.

5. Run the dispersed phase. In this phase, the particles are tracked through the flow field and, the values for the source terms are obtained.

6. Recalculation of the continuous phase considering the new source terms of the dispersed phase and obtain a converged solution for the gas flow field.

7. Compare the solutions for the continuous phase obtained previously, to the actualization of the new particle source terms by calculating the equations residues and verify if they are smaller than what is pretended.

8. If not, repeat steps five, six and seven until the overall convergence is obtained. Otherwise, calculate one last time the dispersed phase with the values obtained from the continuous phase.

After the sequence of events previously described, a post-processing of the data obtained is required to analyze the results and further discuss them, with the intention of drawing conclusions.

3.5 Discretization methodology

The discretization model for the mathematical phase is a crucial step when considering a CFD simulation system. This phase involves the discretization of the space domain and the consequent discretization of the mathematical model equations. As stated by Hirsch [2007], space discretization consists of setting up a mesh, or a grid, by which the continuum of space is replaced by a finite number of points in which the numerical values of the variables will have to be determined. Once a mesh has been defined, the equations can be transformed from differential or integral equations to discrete algebraic operations involving unknown values related to the mesh points. On the current work, to favor simplicity a Cartesian grid with uniform cell sizes was chosen.

Considering that the Finite Volume Method (FVM) has a great advantage of the automatically satisfy the conservation at the discrete level, this was the method chosen. The Quadratic Upstream Interpolation for Convective Kinematics (QUICK) was the discretization scheme that was implemented on the existent computational tool.

The QUICK scheme was proposed by Leonard [1979] and uses, a three-point upstream-weighted quadratic interpolation for cell face values. Systematically, the face value for a cell is obtained from a quadratic function passing through two bracketing nodes, on each side of the face and a node on the upstream side. Usually, the QUICK scheme is typically more accurate on structured meshes aligned with the flow direction.

In the literature, it is customary to write the cell-face values under the form known as the k-scheme as mentioned by Hirsch [2007]. To explain this scheme, a systematic approach

considering the quadratic profiles used in the QUICK scheme is used resorting to Fig. 3.2. Eq. (3.28) represents the one-dimensional control volume QUICK-type schemes formulation. These schemes are based on a weighted average of second-order-upwind and central interpolations of a variable.

In Eq. (3.28), it is assumed that the flow comes from left to right, considered a general variable property per unit volume. If $C = 1$ the result is a central second-order interpolation. For $C = 0$ a second-order upwind value is obtained. The QUICK scheme is obtained for $C = 1/8$.

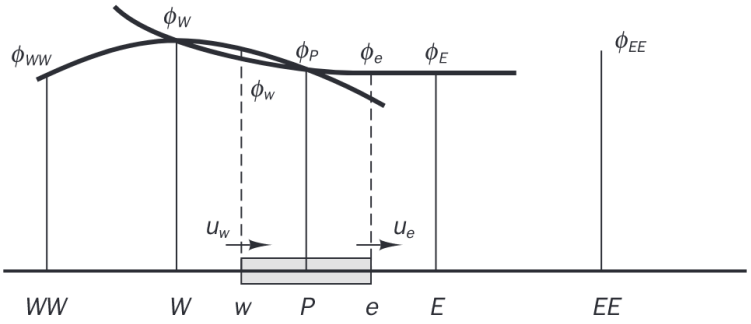

Figure 3.2: Quadratic profiles used in the QUICK scheme, from Versteeg and Malalasekera [2007].

$$\begin{aligned}\phi_e = C\left[\frac{\Delta x_{e,EE}}{\Delta x_{w,e}+\Delta x_{e,EE}}\phi_P + \frac{\Delta x_{w,e}}{\Delta x_{w,e}+\Delta x_{e,EE}}\phi_E\right] + \\ (1-C)\left[\frac{\Delta x_{WW,w}+2\Delta x_{w,e}}{\Delta x_{w,e}+\Delta x_{WW,w}}\phi_P - \frac{\Delta x_{w,e}}{\Delta x_{w,e}+\Delta x_{WW,w}}\phi_W\right]\end{aligned} \tag{3.28}$$

3.6 Pressure-velocity coupling

The pressure-velocity coupling problem is a consequence of several difficulties when solving the Navier-Stokes equations. When examining those equations, there is an equation for solving u, v, and w but no equation for the pressure field, p. The computed velocity field is obtained from the momentum equation and must satisfy the continuity equation. Furthermore, the advective term in the momentum equations is non-linear. Therefore, to numerically solve the Navier-Stokes equations, it is necessary to couple the pressure and velocity using an algorithm.

The Semi-Implicit Method for Pressure Linked Equations (SIMPLE), which was reported in the literature by Patankar and Spalding [1972], was the algorithm that was implemented on the existent tool. Systematically, this algorithm derives an equation for pressure from combining the momentum and continuity equations. Consequently, it derives a corrector for the velocity field that satisfies the continuity equation. On this algorithm, the discretized momentum and pressure correction equations are solved implicitly, whereas the velocity

correction is solved explicitly, justifying the denomination of the semi-implicit method.

Simply, this algorithm is based on a guess-and-correct procedure. A pressure guessed field is used to solve the momentum equations and determine a velocity field which, is a consequence of that assumption. Hereinafter, a pressure correction equation, which has been deduced from the continuity equation, is solved to obtain a pressure correction field. This new field is used to update the velocity and pressure field in each distinct iteration. The steps of the SIMPLE are briefly presented:

1. Guess the pressure field;

2. Solve the momentum equation with the guessed pressure field to obtain the velocity field. The velocity solution obtained does not satisfy the continuity equation;

3. Solve the pressure corrected formulation;

4. Calculate the new pressure field by adding the corrected formulation to the guessed pressure field, in a manner that this field obeys the continuity equation;

5. Calculate the new velocity field using the velocity correction formulas. This velocity field, however, does not satisfy the continuity equation;

6. Solve the discretization equation for other parameters, $\phi's$, if they influence the flow field through fluid properties, source terms, and others. However, if a particular ϕ does not influence the flow field, it is better to calculate it after a converged solution for the flow field has been obtained;

7. Treat the corrected pressure as a new guessed pressure and return to the second step, repeating the whole process until a converged solution is obtained.

The SIMPLE algorithm is usually called a 'pressure-based' algorithm since a Poison equation for the pressure is solved. This algorithm is often used in steady-flow conditions since it consists of a simplistic form of obtaining the pressure-velocity coupling.

Having that in mind, a staggered grid consists of a grid where the scalar variables (pressure, density, total enthalpy, or others) are stored in the cell centers of the control volumes whereas, the velocity or momentum variables are located at the cell faces. The staggered grid ensures that the resulting discrete system will not be singular. Through a staggered grid, it is possible to avoid the odd-even decoupling between the pressure and velocity. This is a direct consequence of velocity and pressure not being defined in the same mesh points.

On a staggered grid, velocity is directly defined at the half mesh points, while the pressure remains defined at the central mesh point. On the other hand, the biggest disadvantage of

using staggered grids consists of different variables being stored at different places, hampering the computational performance. The staggered grid ensures that the resulting discrete system will not be singular. For instance, this decoupling is not present with compressible flows due to the density–velocity coupling in the continuity equation.

3.7 Iterative method for the resolution of algebraic systems

Thomas [1949] developed a technique for rapidly solving tridiagonal systems, the Tridiagonal Matrix Algorithm (TDMA), also known as the Thomas Algorithm. TDMA is a direct method for one-dimensional situations but, it can also be applied iteratively, in a line-by-line way, to solve multi-dimensional problems.

Objectively, the TDMA is a simplified form of Gaussian elimination used to solve a tridiagonal system of equations. Gaussian elimination procedure consists of two distinct phases: a forward elimination phase and a backward substitution phase. It is important to notice that this algorithm is only applicable to diagonally dominant matrices. This methodology is computationally inexpensive and has the advantage of requiring a minimum amount of storage, in contrast to the Jacobi and Gauss-Seidel methods that, although easily implementable, are considered for general-purposes and their convergence rate can be slow when the system of equations is large.

Chapter 4

Physical and mathematical models

After analyzing the existing numerical capabilities, it was necessary to physically interpret the cooling phenomenon, and consequent freezing, of liquid water droplets. This chapter presents the contribution of this dissertation in the conversion of the pre-existent in-house computational tool. Therefore, Section 4.1 overviews the phase-change phenomena from a generic perspective. Section 4.2 focuses on physically model the freezing process of liquid water droplets. Finally, a mathematical model of the process is presented in Section 4.3.

4.1 Overview of the phase-change phenomena

Attending the objectives of this dissertation, is necessary to physically comprehend and model the cooling process of a free-falling liquid water droplet. Thereby, the water droplet will be submitted to a complete phase transition between a liquid state and a solid state.

Phase transitions can be described as shifts between different physical states, or phases, of the same substance. These transitions involve heat and, often, mass transfer and are divided into two different orders. First-order phase transitions are known for, the temperature of a body or a thermodynamic system staying constant as energy is released or absorbed. The temperature in which the transformation occurs is the moment, when, the stability of one phase breaks down in favor of the other according to the available energy. This temperature is called the phase-change temperature. Otherwise, second-order transitions occur continuously as the temperature changes. The phase transition considered on the freezing of liquid water droplets is a first-order transition, taking into account that solidification happens through a crystallization process in which both the solid and liquid phases coexist. Additionally, the temperature at this point is constant (freezing temperature).

According to Tanner [2011], many pure substances, water particularly, experience supercooling. Examining the definition of supercooling, which was presented in Chapter 2, and considering that supercooling icing conditions are usual in the aeronautical context, it is possible to conclude that the definition of first-order phase transition can conflict with the concept of supercooling. However, it is important to notice that the period in which the temperature is not constant is too small and, for that reason, usually neglected. Consequently, we extend the standard treatment of a supercooling process as a first-order phase transition.

Bearing this in mind is essential to quantify the energy enclosed on a thermodynamic system to quantify the energy transfers between a certain body and the surrounding environment. The total energy of a system consists of kinetic energy, potential energy, and internal energy. Considering that mechanical energy, which is the sum of kinetic and potential energy, is usually neglected on heat transfer problems, due to its low variation, it is important to define internal energy. Internal energy consists of sensible, latent, chemical, and nuclear components. To study heat transfer, we focus on the sensible and latent components of the internal energy, which are, together, referred to as thermal energy.

The sensible component accounts for the translational, rotational, and/or vibrational motion of the atoms/molecules comprising the matter, being the portion that we associate mainly with temperature changes (although it can also be associated with pressure). This component has a macroscopic indicator which is the temperature variation. The latent component relates to intermolecular forces influencing phase change between solid, liquid, and vapor states. If no phase change is occurring, there is no change in latent energy, and therefore, its variation is zero. When phase changes occur to higher entropy levels (high molecular system disorder), for instance, melting or vaporization, the latent energy increases, otherwise, it decreases. In this particular case (phase-change between liquid and solid states), this component is called fusion latent heat.

Therefore, the solidification of a liquid requires removing the latent heat and structuring atoms into more stable lattice positions than they were in the liquid state. During that process, the thermophysical properties that, up to that point varied linearly with the temperature, may suffer a non-linear variation. For instance, according to Alexiades and Solomon [1993], typical density changes upon freezing or melting are in the range of 5% to 10% but can be as high as 30%.

The physical mechanisms which underlie the heat transfer mode can be of three distinct natures: conduction, convection, and radiation. Conduction is the transfer of energy from the more energetic to the less energetic particles of a substance due to interactions between those particles, in which there is no flow or mass transfer of the material. Convection occurs when energy transfers due to random molecular motion, diffusion, or macroscopic motion of the fluid. Radiation is the energy emitted by matter that is at a non-zero temperature.

Considering the cooling process of airborne droplets in a cold atmosphere, heat transfer occurs by three main mechanisms: convective heat transfer, convective mass transfer, and thermal radiation. Systematically, cooling can be described as the process in which heat is removed from a body that integrates a thermodynamic system to its surrounding environment. Usually, this process results in a lower temperature and/or phase change.

As stated before, a liquid has a higher level of microscopical disorder, and consequently, a higher entropy when compared with a solid, where molecules vibrate around fixed equilibrium positions. Thus, in a solid, particles are arranged in a high condensed matter

state. Concerning the disposal of its particles, a solid can be classified as amorphous if it is not organized in a definite lattice pattern (lack of long-range order) or as crystalline if the microscopic structure is highly ordered, forming a crystal lattice that extends in all directions. In nature, ice (solid phase of water) is considered crystalline.

Therefore, in the process of cooling water, until reaching a solid state, a phase transition region occurs where solid and liquid phases coexist, which is called the interface. During that moment, the crystallization process is occurring, and different microscopic structures may appear.

4.2 Physical modeling of the freezing process

As referred in Chapter 2, many authors reunited efforts on physically modeling the phenomenon behind supercooling. From the works presented in Section 2.5, Miyawaki et al. [1989], Epstein and Fauske [1993], Hindmarsh et al. [2003], and Tanner [2011] constitute good examples of those efforts.

Figure 4.1 represents an idealized temperature profile of a freezing water droplet subjected to supercooling, mainly based on the fundamentals considered in the previously literature. As it is seen, on the freezing process of a water droplet, initially, at room temperature, four distinct stages are identified: liquid stage, recalescence stage, solidification stage, and solid stage.

To develop a numerical model, each stage of the freezing process has to be described separately and carefully interpreted. Bearing this in mind, a detailed description of the four-stage freezing model is presented.

- **Pre-cooling, supercooling, or liquid stage**: a droplet cools from its initial temperature to the nucleation temperature, T_n, which lies below the equilibrium freezing temperature or phase change temperature, T_{ph}. When the droplet temperature reaches nucleation temperature, crystallization begins and, the supercooled droplet starts to crystallize and enters the recalescence stage.

- **Recalescence stage**: the droplet temperature jumps from subzero to the phase change temperature, T_{ph}, with partial water converted into ice, resulting in an ice-water mixture phase in the droplet (highly transient). At this stage, supercooling drives rapid crystallization kinetics, releasing latent heat, resulting in an increase of temperature and, consequently, the crystal growth from the crystal nuclei. This stage finishes when the supercooling is exhausted and the droplet has reached its equilibrium freezing temperature, T_{ph}. This stage contains two inner periods:

  - **Ice nucleation**: ice nucleus forms in the supercooled water droplet at crystallization temperature.

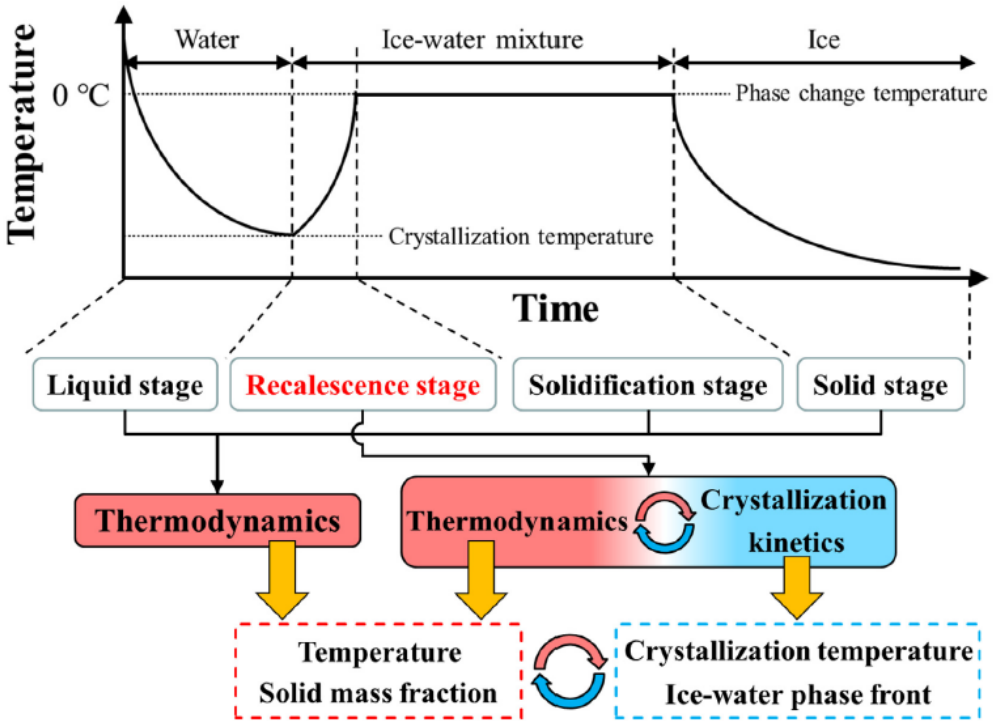

Figure 4.1: Schematic illustration of the four-stage theoretical model in the entire freezing process of water droplets from Meng and Zhang [2020]. Pure water under atmospheric pressure freezes at 273.15 K equivalent to 0 °C, being considered the phase-changing temperature.

  - **Crystal growth**: crystal growth spreading over the entire droplet. The solid water droplet mass fraction increases with the ice crystals growth. The temperature also drastically increases up to the T_{ph}.

- **Solidification stage**: the temperature of the ice-water mixture in the droplet remains at the phase change temperature, and the solid mass fraction increases continuously. Crystal growth is governed by the heat transfer rate from the droplet up to the point in which the liquid droplet is completely frozen. This constitutes, simultaneously, the moment in which this stage finishes.

- **Cooling, tempering, or solid stage**: the droplet is entirely frozen. The temperature of the ice droplet drops to near the ambient temperature.

The transition temperature of each stage, presented in Figure 4.1, was obtained by resorting to a theoretical balance for the droplet internal energy, against the heat loss to the environment. Therefore, it was possible to obtain the representation for the temperature curve/profile alongside the time.

Commonly, for a water droplet with a diameter of several millimeters, the recalescence stage, typically, has a time duration that can be less than 100 ms, as mentioned by Meng and Zhang [2020]. This fact imposes difficulties for both experimental and theoretical studies.

Results showed that, during this phase, ice crystals grow in a dendritic shape [1] for a supercooled water droplet, creating dendritic zones. As noticed by Wang et al. [2019], those zones are composed of an ice-water mixture. The same author stated that, during this phase, a propagating interface between the dendritic zone and supercooled water is usually observed. For instance, Figure 4.2 shows the propagating interface (in red) during the recalescence stage, in which, on certain conditions, took $10\,\mathrm{ms}$. Atomic diffusion through the liquid–solid interface plays a crucial role in the interface kinetics representation, as seen in Figure 4.1.

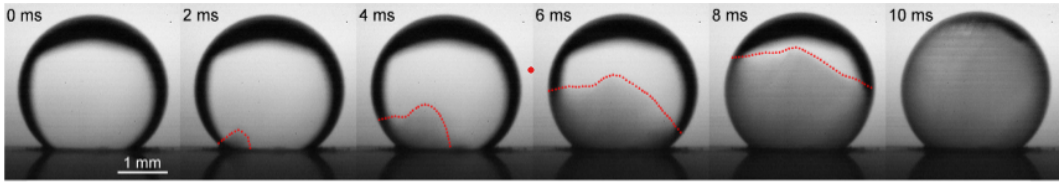

Figure 4.2: Example of dendritic ice growth after nucleation in deep supercooling regime. The temperature is $-21\,^{\circ}\mathrm{C}$, and the droplet volume is $15\,\mu\mathrm{L}$, from Wang et al. [2019].

Furthermore, the recalescence stage cannot be described, using only thermodynamics. To fully characterize this short stage, in specific the transient temperature jump from the nucleation temperature to the phase change temperature and the propagation of the ice-water phase front interface, it is necessary to pay attention to crystallization kinetics too. Therefore, crystallization kinetics dominates the recalescence stage, where the nucleation rate and ice growth velocity are highly temperature-dependent.

To model the internal heat transfer of a droplet, two distinct methodologies are used. Firstly, it is possible to solve the internal temperature profile by describing internal heat conduction by assuming a uniform temperature within the droplet, considering that the transient heat transfer of the droplet is predicted by simply balancing the heat flux on the surface, by heat and mass transfer, with the internal energy of the droplet. On the other hand, neglecting the internal spatial distribution profile of temperature can be a quicker solution. A simplistic balancing of the external heat transfer with the amount of latent heat required to be removed, to completely freeze the mass of water in the droplet, constitute a valid solution. However, it is necessary to validate its use in all stages of the freezing process to mitigate errors. This topic is reintroduced in Section 4.3.

To accurately apply the first methodology, it is necessary to explore the thermodynamic characteristics of chilling single-phase liquid and solid droplets, solidification of the two-phase ice-water mixture, and the crystallization phenomenon, including the temporal evolution of temperature and solid mass fraction of the droplet. On the other hand, in the second methodology, the crystallization kinetics are ignored and the thermodynamic characteristics of the chilling single-phase liquid and solid droplets are addressed. In this dissertation, the second methodology was used.

[1] Tree-like structure of crystals growing.

4.3 Mathematical modeling of the freezing process

Having presented the physical model behind the supercooling of water droplets resorting to a four-stage formulation, this section introduces the mathematical models for each of those stages. However, when presenting the following model, several considerations and assumptions were made to simplify the implementation.

Even when considering a simple balance between the droplet and the surrounding environment, it is necessary to consider the transport processes impact in the interior of the particle. Yao and Schrock [1976] proposed three models to represent these phenomena: complete mixing model, non-mixing model, and mixing model. The simplest model consists of assuming that the internal motion of the droplet is so vigorous that a complete mixing is achieved. This results in a temperature profile inside the droplet that is essentially flat. The non-mixing model assumes there is no internal motion and, the energy equation is reduced to a transient heat conduction equation. The mixing model appears after considering that neither the complete-mixing model nor the non-mixing model are realistic, since they are based on extreme situations experienced by the droplet. Therefore, this last model considers both the effects of oscillations and the internal circulation for the mixing inside the droplet.

To obtain the four-stage model equations, the following assumptions and considerations had to be made.

- The particle is assumed to be spherical.
- Spherical symmetry of the vapor boundary layer around the particle is assumed.
- Particle-particle collisions are neglected.
- The particle density is assumed to be much larger than the surrounding fluid density, considering a dilute particle-laden flow problem.
- The particle mass variation is neglected.
- Liquid/vapor equilibrium on the particle surface.
- A complete mixing model is assumed. This results in representing the internal motion of the droplet neglecting the internal heat transfer gradients.

Relatively to the convention used for the heat transfer between the droplet and the surrounding environment, Figure 4.3 represents a water droplet in a free fall surrounded by a humid air gas stream and the heat exchange inherent to the process. The heat fluxes due to the convective heat transfer and thermal radiation have an outward flux to the surrounding environment. However, since we are in the presence of a cooling process, the

heat flux due to convective mass transfer has an inwards movement. Since the temperature differences between the droplet and the far-field region of the gas are significant, a diffusive-convective region appears around the droplet. In this region the temperature is given by a combination between the droplet and gas temperatures, being described as a reference temperature (shown in Eq. (4.15)).

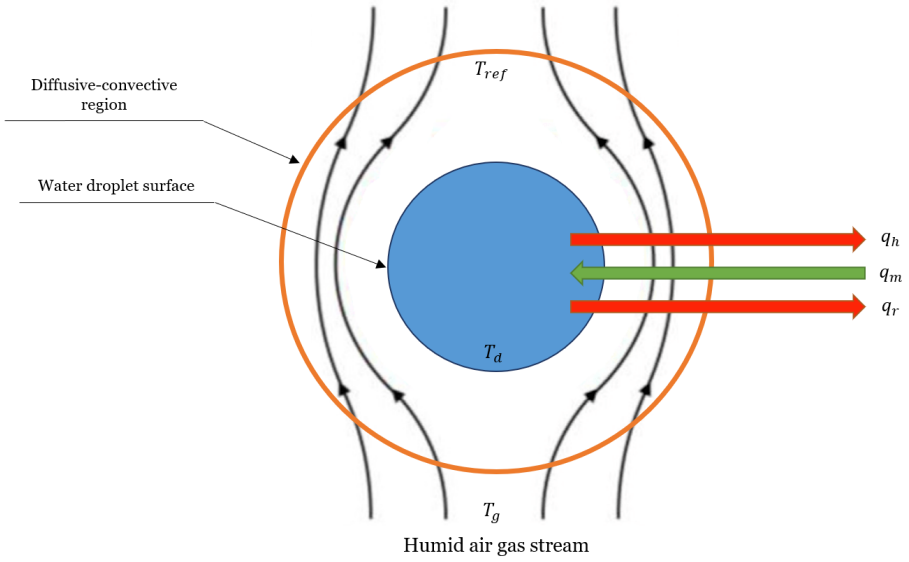

Figure 4.3: Schematic illustration of a droplet freezing in a cold humid air gas stream.

For the next equations, the convention used in Figure 4.3 is the one that was used to obtain the energy balances that describe the temperature profile of a water droplet over time.

4.3.1 Stage 1 - Pre-cooling, supercooling, or liquid stage

Assuming that particles have a uniform temperature distribution, and considering that the cooling of the liquid or solid particles, in stage one or stage four, is determined by the energy exchange of the particles with the surrounding environment, the rate of temperature change is described by Eq. (4.1).

$$\rho_d V_d c_{p,d} \frac{dT_d}{dt} = -A_d \left(q_h + q_m + q_r\right) \quad (4.1)$$

The subscript d denotes the particle properties (liquid or solid), $c_{p,d}$ is the specific heat capacity at constant pressure, ρ_d the specific mass, T_d the temperature, V_d the volume, and A_d the surface area. The parameters q_h, q_m, and q_r denote the heat fluxes (per unit area) due to the convective heat transfer, the convective mass transfer, and the thermal radiation, respectively.

The convective heat flux, q_h, from the particle surface to the ambient gas is given by Eq. (4.2),

where $T_{g\infty}$ is the temperature of the ambient gas in a far-field region and h_h is the convective heat transfer coefficient.

$$q_h = h_h \left(T_d - T_{g,\infty}\right) \quad (4.2)$$

The heat flux due to the convective mass transfer is given by Eq. (4.3), where L_{ph} is the specific latent heat of phase change, ρ_{wv} is the specific mass of water vapor, ρ_g the specific mass of the surrounding gas and h_m the convective mass transfer coefficient.

$$q_m = L_{ph} h_m \left(\rho_{wv} - \rho_{g,\infty}\right) \quad (4.3)$$

The heat flux due to thermal radiation is given by Eq. (4.4), where e is the emissivity for thermal radiation and σ is the Stefan–Boltzmann constant of radiation.

$$q_r = e\sigma \left(T_d^4 - T_{g,\infty}^4\right) \quad (4.4)$$

To obtain the values for the convective heat transfer coefficient, h_h, and the convective mass transfer coefficient, h_m, two dimensionless numbers, the Nusselt and Sherwood numbers are required. The Nusselt number $(\mathrm{Nu_d})$, which is represented in Eq. (4.5), is described as the ratio of convection to pure conduction heat transfer. The Sherwood number $(\mathrm{Sh_d})$, in Eq. (4.6), is described as the ratio of convective mass transfer to diffusive mass transfer.

$$\mathrm{Nu_d} = \frac{h_h d}{\lambda_g} \quad (4.5)$$

$$\mathrm{Sh_d} = \frac{h_m d}{D_{v-g}} \quad (4.6)$$

In terms of nomenclature, d is the drop diameter, λ_g the conductive heat transfer coefficient of the ambient gas, and D_{v-g} the vapor-gas diffusivity. To obtain the convective coefficients, as seen in Eqs. (4.5) and (4.6), it is necessary to use statistical correlations based on empirical results gathered in certain experimental conditions. Ranz and Marshall [1952a,b] developed a correlation for the case of steady-state heat transfer of solid spheres with the intuit of obtaining the convective heat and mass coefficients. This correlation is commonly known as the Ranz-Marshall classical formulation (RM).

However, on the heat and mass transfer study, performed by Yao and Schrock [1976], was concluded that for certain conditions, the vibrations and deformations of the falling droplets have an impact on heat and mass transfer coefficients and, for that, reason have to be accounted for. Therefore, the same authors presented a Ranz-Marshall corrected formulation (RMcf) has an attempt of accounting for those effects since the first formulation considers a complete mixing model.

Table 4.1 represents the correlations used to calculate the convective effects experienced by the droplets. The range in which these correlations are valid is stated in Eq. (4.7). Both correlations depend of dimensionless numbers such as the Reynolds number, $\mathrm{Re_d}$, the Prandtl number, $\mathrm{Pr_d}$, and the Schmidt number, $\mathrm{Sc_d}$.

Table 4.1: Correlations used to calculate the convective effects experienced by the droplets.

Designation	Assumption	Nusselt number $(\mathrm{Nu_d})$	Sherwood number $(\mathrm{Sh_d})$
RM	Complete mixing model	$2 + 0.6{\mathrm{Re_d}}^{1/2}{\mathrm{Pr_d}}^{1/3}$	$2 + 0.6{\mathrm{Re_d}}^{1/2}{\mathrm{Sc_d}}^{1/3}$
RMcf	Mixing model	$2 + 15{\mathrm{Re_d}}^{1/2}{\mathrm{Pr_d}}^{1/3}\left(\frac{z}{d}\right)^{-0.7}$	$2 + 15{\mathrm{Re_d}}^{1/2}{\mathrm{Sc_d}}^{1/3}\left(\frac{z}{d}\right)^{-0.7}$

$$3\,\mathrm{mm} \leq d \leq 6\,\mathrm{mm}; 10 \leq \left(\frac{z}{d}\right) \leq 600 \quad (4.7)$$

The Reynolds number $(\mathrm{Re_d})$, which indicates the ratio of the inertia and viscous forces, Prandtl number $(\mathrm{Pr_d})$, which represents the ratio of the momentum and thermal diffusivities, and Schmidt number $(\mathrm{Sc_d})$, which gives the ratio of the momentum and mass diffusivities, are obtained by Eqs. (4.8), (4.9) and (4.10), respectively. The characteristics of the dimensionless numbers are based on the droplet's diameter.

$$\mathrm{Re_d} = \frac{\rho_g \parallel \overrightarrow{U}_{rel} \parallel d}{\mu_g} \quad (4.8)$$

$$\mathrm{Pr_d} = \frac{c_{p,g}\mu_g}{\lambda_g} \quad (4.9)$$

$$\mathrm{Sc_d} = \frac{\mu_g}{\rho_g D_{v-g}} \quad (4.10)$$

The $\| \overrightarrow{U}_{rel} \|$ is the norm of the relative droplet-gas velocity, μ_g is the dynamic viscosity of the surrounding gas and $c_{p,g}$ the gas specific heat capacity at constant pressure. To calculate the dimensionless numbers presented before, Eqs. (4.11), (4.12), (4.13) and (4.14) are required. These equations were suggested by Lefebvre and McDonell [2017] on the process of droplets evaporation.

$$\rho_g = \left(\frac{[\Upsilon_a]_{ref}}{\rho_a} + \frac{[\Upsilon_{wv}]_{ref}}{\rho_{wv}} \right)^{-1} \quad (4.11)$$

$$\mu_g = [\Upsilon_a]_{ref}\, \mu_a + [\Upsilon_{wv}]_{ref}\, \mu_{wv} \quad (4.12)$$

$$c_{p,g} = [\Upsilon_a]_{ref}\, c_{p,a} + [\Upsilon_{wv}]_{ref}\, c_{p,wv} \quad (4.13)$$

$$\lambda_g = [\Upsilon_a]_{ref}\, \lambda_a + [\Upsilon_{wv}]_{ref}\, \lambda_{wv} \quad (4.14)$$

$[\Upsilon_a]_{ref}$ corresponds to the air mass fraction, $[\Upsilon_{wv}]_{ref}$ to the water vapor mass fraction, ρ_a specific mass of dry air, ρ_d specific mass of the droplet (liquid or solid), μ_a dynamic viscosity of dry air, μ_{wv} dynamic viscosity of water vapor, $c_{p,a}$ specific heat of dry air at constant pressure, $c_{p,wv}$ specific heat of water vapor at constant pressure, λ_a dry air thermal conductivity and λ_{wv} water vapor thermal conductivity. It is important to notice that the subscript ref indicates that the parameter was calculated resorting to a reference

temperature. This temperature combines the droplet temperature and the ambient gas temperature, pretending to represent a near droplet region in which the temperature of the droplet has great influence on the surrounding air (diffusive-convective region). The reference temperature is given by Eq (4.15).

$$T_{ref} = T_d + \frac{T_g - T_d}{3} \quad (4.15)$$

The water vapor-gas mass diffusivity, which is necessary to obtain the Schmidt number in Eq. (4.10), was obtained by Eckert and Drake [1959] for a temperature range between $223.15\,\mathrm{K}$ and $293.15\,\mathrm{K}$ and is given by Eq. (4.16).

$$D_{v-g} = 2.227 \times 10^{-5} \left(\frac{T_{ref}}{273} \right)^{1.81} \quad (4.16)$$

The relation between the dry air mass fraction, at reference conditions, and the water vapor mass fraction, at reference conditions, which is necessary to obtain the gas properties, is given by Eq. (4.17). However, to fully comprehend how this equation is obtained it is necessary to study concept of humidity.

$$[\Upsilon_a]_{ref} = 1 - [\Upsilon_{wv}]_{ref} \quad (4.17)$$

In accordance with Wallace and Hobbs [2006], considering a closed box containing pure water, at temperature T, and air, initially assumed completely dry, it is common sense that after a while, water will begin to evaporate and, as it does so, the number of water molecules in the air will increase. Therefore, the water vapor pressure inside the box will increase. Simultaneously, the rate at which the water molecules condense, from the vapor phase back to the liquid phase, will increase. While the condensation phenomenon is less than the evaporation rate, the air is said to be unsaturated. When the rate of condensation is equal to the evaporation rate, the air is said to be saturated. The moment at which the air becomes saturated is designated at the saturation point. To quantify the amount of water vapor or dry air in a certain volume of air and, the saturation point, different relations are used.

The amount of water vapor in a certain volume of air may be defined as the ratio between the water vapor mass, m_{wv}, and the mass of dry air, m_a. This ratio is designated as mixing ratio or as humidity ratio, HR, and is given by equation Eq. (4.18).

$$HR = \frac{m_{wv}}{m_a} \quad (4.18)$$

Equation (4.19) represents the saturation mixing ratio, $[HR]_{sat}$, which is defined with respect to the mass of water vapor, in a given volume of air, that is saturated, $[m_{wv}]_{sat}$.

$$[HR]_{sat} = \frac{[m_{wv}]_{sat}}{m_a} \quad (4.19)$$

The ratio between the water vapor mass and the air mass (dry air plus water vapor) is called the specific humidity, SH, and is represented by Eq. (4.20). Considering that the magnitude of HR is usually small, it can be concluded that the numerical values of HR and SH are nearly equivalent.

$$SH = \frac{m_{wv}}{m_{wv} + m_a} = \frac{HR}{1 + HR} \quad (4.20)$$

The relative humidity for water, RH, is the ratio between the actual mixing ratio of the air and the saturation mixing ratio concerning a plane surface of pure water at the same temperature and pressure, expressed as a percentage. This parameter is given by Eq. (4.21).

$$RH = \frac{HR}{[HR]_{sat}} \quad (4.21)$$

Therefore, it is possible to conclude that, when the humidity ratio is known, it is possible to obtain the specific humidity and, consequently, get the value for the water vapor mass fraction on Eq. (4.17).

4.3.2 Stage 2 - Recalescence stage

As presented in Figure 4.1, once the nucleation starts, the droplet experiences a rapid temperature increase until it reaches the equilibrium freezing temperature or phase-change temperature. Thereby, a solid mass fraction develops and grows, creating an ice-water

mixture that, on the next stage, continuously increases. The portion of the droplet volume that is solidified during this stage, V_{rec}, can be estimated from an heat balance equation as it is shown in Eq. (4.22). In terms of nomenclature, the nucleation temperature, T_n, is usually an empirical value, L_{ph} the specific latent heat due to crystallization, and ρ_s the solid particle specific mass.

$$V_{rec} = V_d \frac{\rho_l c_{p,d} \left(T_{ph} - T_n\right)}{\rho_s L_{ph}} \quad (4.22)$$

As stated in Section 4.2, the recalescence stage has a short duration, and for that reason, each droplet is assumed to change its temperature instantly and, consequently, the recalescence time is neglected.

4.3.3 Stage 3 - Solidification stage

After the recalescence stage, the remaining liquid becomes completely frozen due to the heat transfer phenomenon between the droplet and the surrounding gas at a constant equilibrium freezing temperature, T_{ph}, as represented in Figure 4.1. Assuming that the nucleation is uniformly spread throughout the droplet and the specific latent heat due to this phenomenon, L_{ph}, is removed by the external heat fluxes, Eq. (4.23) mathematically describes the physical phenomenon for this stage.

$$\rho_d V_d c_{p,d} \frac{dT_d}{dt} = -A_d \left(q_h + q_m + q_r\right) + L_{ph} \rho_s \frac{dV_s}{dt} \quad (4.23)$$

Yet, assuming that during the solidification stage, the temperature of the droplet stays constant with time, the rate at which the volume of solid is produced is given by Eq. (4.24). It is considered that the initial value for V_s at this stage is the last one registered on recalescence stage. It is important to enhance that to still allow mass transfer via evaporation it had to be assumed that the outer surface of the droplet remains liquid during this process otherwise, the phenomenon would occur due to sublimation.

$$L_{ph} \rho_s \frac{dV_s}{dt} = A_d \left(q_h + q_m + q_r\right) \quad (4.24)$$

Depending on the case, the assumption of a uniform droplet temperature during this stage is only justified after analyzing the Biot number, $\mathrm{Bi_d}$. The Biot number, in Eq. (4.25), is a dimensionless number that corresponds to the ratio between the internal thermal resistance

of a solid and the boundary layer thermal resistance. In terms of physical interpretation, as stated by Bergman et al. [2011], if $\mathrm{Bi_d} \ll 1$, for steady-state conditions, the resistance to conduction, within the solid, is much less than the resistance due to convection across the fluid boundary layer. Thereby, the assumption of a uniform temperature distribution within the solid is reasonable. Otherwise, the temperature profile within the particle should be accounted for as Hindmarsh et al. [2003] suggest.

$$\mathrm{Bi_d} = \frac{h_h d}{2\lambda_d} \quad (4.25)$$

Additionally, calculating the Lewis number is relevant for any situation involving simultaneous heat and mass transfer by convection. Similar to the Prandtl number, which correlates the momentum transport and the thermal transport properties of a fluid, and to the Schmidt number, which correlates the momentum transport and the mass transport of a fluid, the Lewis number correlates the mass transport with the thermal transport properties of the fluid. This number is given by Eq. (4.26). Usually, the Lewis number is considered equal to one, which means that thermal and mass diffusivities have the same significance to the process. As a consequence of this assumption, the D_{v-g} equals the α_{v-g}. However, in this work, D_{v-g} was calculated resorting to Eq. (4.26).

$$\mathrm{Le_d} = \frac{\alpha_{v-g}}{D_{v-g}} = \frac{\mathrm{Sc_d}}{\mathrm{Pr_d}} = \frac{\frac{\mu_g}{\rho_g D_{v-g}}}{\frac{c_{p,g}\mu_g}{\lambda_g}} \quad (4.26)$$

4.3.4 Stage 4 - Cooling, tempering or solid stage

The cooling stage is very similar to the pre-cooling stage, considering that the thermodynamics behind it are the same. At this stage, the temperature changing rate is given, similarly to the pre-cooling, by Eq. (4.1) in Section 4.3.1. It is important to notice that, at this stage, the droplet is totally solidified, and, for that reason, the d subscript which, in Eq. (4.1), corresponded to liquid water has to be changed to solid.

Chapter 5

One-way versus two-way coupling analysis

This chapter provides a comparison between the numerical results obtained by readapting the existent, in-house, computational tool and other studies, numerical and experimental, that were previously performed by other authors and are available on the literature. Section 5.1 briefly presents the studies which were used to compare with the two-way coupling results obtained in this dissertation. The computational domain setup, as well as the boundary conditions applied, are presented in Section 5.2. A study of grid independence, to guarantee that the solution obtained does not depend on the geometry or discretization method used, is presented in Section 5.3. Section 5.4 describes the influence of a variable humidity ratio on the cooling process of a water droplet, with a constant diameter. On the other hand, Section 5.5 analyses the same influence but for a variable droplet diameter with a constant humidity ratio. Finally, Section 5.6 presents a summary of the results obtained.

5.1 Introduction

Having interpreted the existent capabilities, comprehended and described the Eulerian-Lagrangian formulation in which it is based, and adapted the computational tool to the matter in discussion, it is now necessary to validate the changes that were made. This validation pretends to ensure that the readaptations to the existent tool, are coherent with the conclusions drawn, by different authors, on their experimental and computational studies. Additionally, and under the same reasoning of what was said in Chapter 3, it would be interesting to compare the results based on the two-way coupling model, with a model that does not account for the mutual influence between the particles and their surrounding environment, examining both results.

Magalhães et al. [2016] performed a numerical study of freezing droplets in which the computational results for the cooling of free-falling water droplets were obtained using a one-way coupling model. To determine the cooling rate of water droplets under several humidity conditions, Magalhães et al. [2016] used two distinct correlations, making it possible to calculate the heat and mass transfer coefficients. The Ranz-Marshall correlations were the same that were presented in Table 4.1. After obtaining the numerical results, Magalhães et al. [2016] compared those results with experimental data gathered by Yao and Schrock [1976] to validate the implemented model.

Briefly examining the experimental work performed by Yao and Schrock [1976] can be

understood that droplets, with distinct diameters and initial temperatures, were dropped from a droplet generator into a plastic column where an airflow with a certain humidity content and temperature was present. This study had the objective of providing accurate data for the relation between the mean temperature of the droplet and its position during the free fall, considering different droplet sizes and humidity ratios of the environment. Simultaneously, for control purposes, the initial droplet temperature, the environment temperature and the air humidity ratio were pointed out.

Four distinct droplet diameters and four different humidity ratios were used during this experiment. The air and initial droplet temperature were registered before letting each droplet fall. The initial conditions performed on the experimental study of heat and mass transfer of freely falling drops by Yao and Schrock [1976] are summarized in Table 5.1, where twelve distinct cases are present. For each droplet diameter, three distinct humidity ratios were used to represent a low, medium, and high humidity contents.

Table 5.1: Initial conditions performed on the experimental study of heat and mass transfer of freely falling droplets by Yao and Schrock [1976].

Case	Droplet diameter [mm]	Humidity ratio	Initial droplet temperature [K]	Environment temperature [K]
1	3	0.29	313.85	296.44
2	3	0.36	313.88	295.47
3	3	1.00	313.84	296.48
4	4	0.36	313.89	295.59
5	4	0.52	313.79	294.48
6	4	1.00	313.94	296.48
7	5	0.29	313.83	296.03
8	5	0.36	313.87	295.71
9	5	1.00	313.89	296.76
10	6	0.36	313.89	295.29
11	6	0.52	313.81	294.48
12	6	1.00	313.85	296.48

After understanding the conclusions obtained by Magalhães et al. [2016], it was possible to state that for lower humidity ratios, the numerical results showed a close agreement with the data gathered by Yao and Schrock [1976] suggesting that the cooling process followed a steady-state regime since the one-way coupling model was being used. However, for high humidity ratios, this work was not able to resemble the experimental data. This suggested the presence of a transient regime, where the mutual interaction between the droplet and the surrounding environment is predominant for these conditions.

5.2 Computational domain configuration

To compare the numerical results obtained by Magalhães et al. [2016], the ones that resulted from implementing the two-way coupling model and the experimental data gathered by Yao and Schrock [1976], it was necessary to consider a computational domain that resembles the experimental setup built by Yao and Schrock [1976].

This setup, in a simple manner, consisted of a plastic column of a squared base with $0.170\,\mathrm{m}$ of edge, $3\,\mathrm{m}$ of height, and a droplet generator. The droplet generator is set on the center of the upper face and, an air stream is injected downwards from the upper face into the lower face with the velocity of $0.03\,\mathrm{m\,s^{-1}}$. Figure 5.1 represents a three-dimensional scheme configuration of the computational domain used. Figure 5.2 represents also the computational domain configuration but considering two distinct cross-sections, for easier understanding.

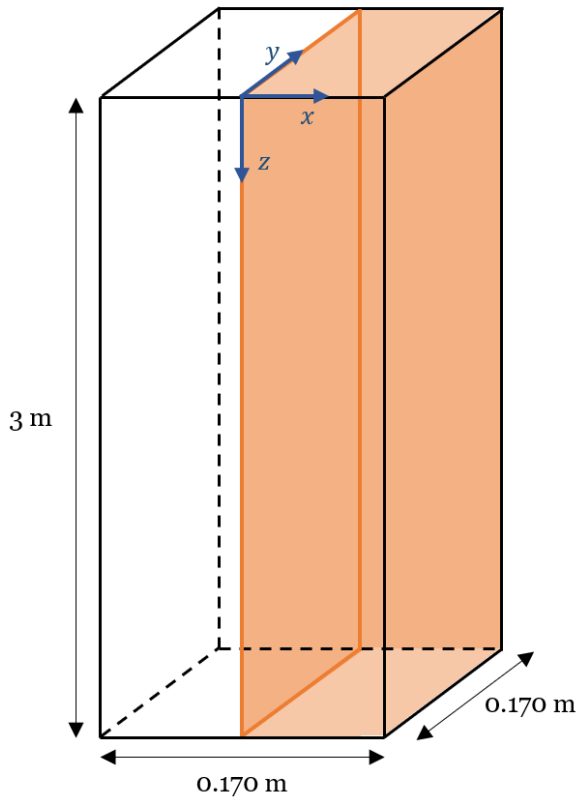

Figure 5.1: Three-dimensional configuration of the computational domain.

Besides, to speed up the numerical calculations, considering the existence of a symmetry plane for $x = 0$, only half of the column was effectively simulated, represented by the section in orange in Figures 5.1 and 5.2. Therefore, the numerical results which correspond to the full extent of the column are obtained by symmetry. The Cartesian reference frame has its origin on the upper face and is represented in blue. In this way, four distinct boundary conditions are present in this study: an inlet plane, an outlet plane, a symmetry plane, and three solid walls representing the distinct sides of the column.

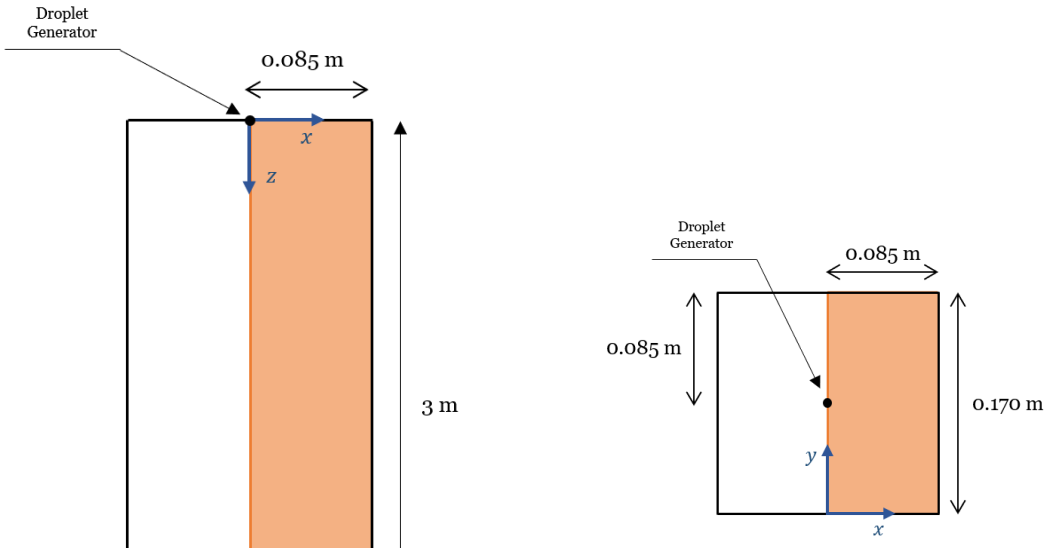

(a) Cross-section $y = 0$.

(b) Cross-section $z = 0$.

Figure 5.2: Computational domain configuration considering two distinct cross-sections.

5.3 Grid independence study

When using a discretized space, it is essential to obtain a solution that does not depend on the geometry or discretization method selected. Therefore, a grid independence study eliminates that possibility. Ideally, given a certain level of accuracy for a solution, the grid that is used has to be good enough to achieve that accuracy using the minimum possible computational power. To ensure that the numerical results do not depend on the discretized space a grid independence study was performed using three levels of refinement with 9660 (coarse mesh), 19200 (fine mesh), and 38000 (finest mesh) points in a structured orthogonal mesh of rectangular elements. The configuration of these grids is presented on Table 5.2.

Table 5.2: Grids used on the grid independence study.

x elements	y elements	z elements	Total number of elements
7	12	115	9660
8	16	150	19200
10	20	190	38000

Figure 5.3 shows the comparison between those three grids resorting to the conditions of the first case presented in Table 5.1. The X-axis represents the vertical component for the particle velocity normalized by the initial gas velocity and the Y-axis represents the droplet height normalized with the total vertical length of the computational domain.

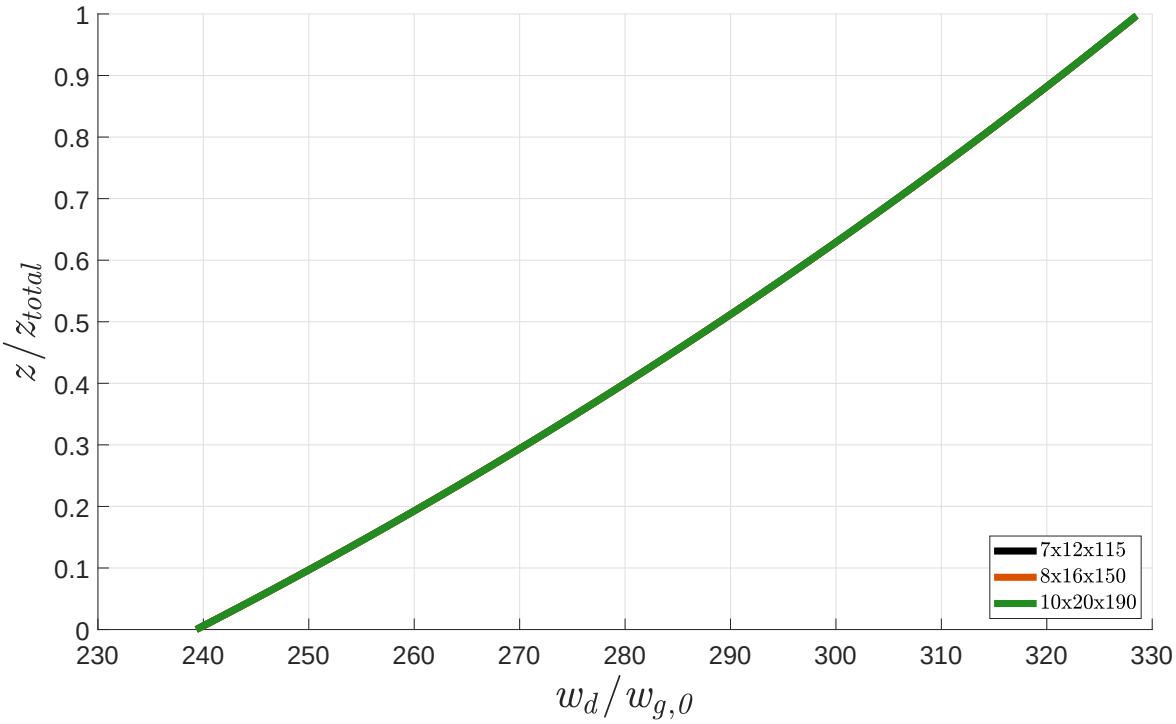

Figure 5.3: Grid independence study for three distinct grids.

Observing Figure 5.3, it becomes obvious that the grid independence was achieved since there is not a major deviation of the results presented, bearing in mind that they are all overlapping each other. The grid used for the space discretization, which ensures grid independence of this problem, was the one with 19200 points (fine mesh).

5.4 Influence of a variable humidity ratio with a constant droplet diameter

A comparison between two distinct Ranz-Marshall correlations is performed and examined in every case. The first one is the classical Ranz-Marshall formulation and the second one consists of a corrected formulation, as presented in Table 4.1. These formulations correspond to a complete mixture model assumption or a mixture model assumption, respectively.

To evaluate the cooling rate over time, two distinct parameters were monitored: the droplet temperature and its falling height. These parameters are presented in a non-dimensional way to enable a fair comparison of the phenomenon for different conditions. The droplet falling height was dimensionalized with the droplet diameter, and the temperature variation was dimensionalized considering the following formula: $(T_d - T_{d,0}) \,/\, (T_{g,\infty} - T_{d,0})$.

For every figure that follows, filled circles correspond to experimental data gathered by Yao and Schrock [1976], dashed lines to the numerical results obtained by Magalhães et al. [2016], and the solid lines to the numerical results obtained resorting to the mathematical and physical models presented in Chapter 3 and 4. In those figures, RM corresponds to the

Ranz-Marshall classical formation and, RMcf to the Ranz-Marshall corrected formation, developed by Yao and Schrock [1976]. The distinct colors for the lines do not have any particular meaning, apart from making it possible to distinguish them easily.

In Figure 5.4 is represented the temperature variation on a single water droplet, falling through the air, with a diameter of $3\,\mathrm{mm}$ and an air humidity ratio of 0.29 for both Ranz-Marshall correlations. Observing Table 5.1, it is possible to determine that Figure 5.4 represents the first case.

The data represented in Figure 5.4 states that the results obtained by Magalhães et al. [2016], using the classical formulation, are the ones that predict the phenomenon, generically, in a better way. However, up to a falling height of 80 diameters, the results obtained by the two-way coupling model, resorting to the Ranz-Marshall corrected formulation, are the ones that predict the cooling phenomenon more accurately even that underestimating it.

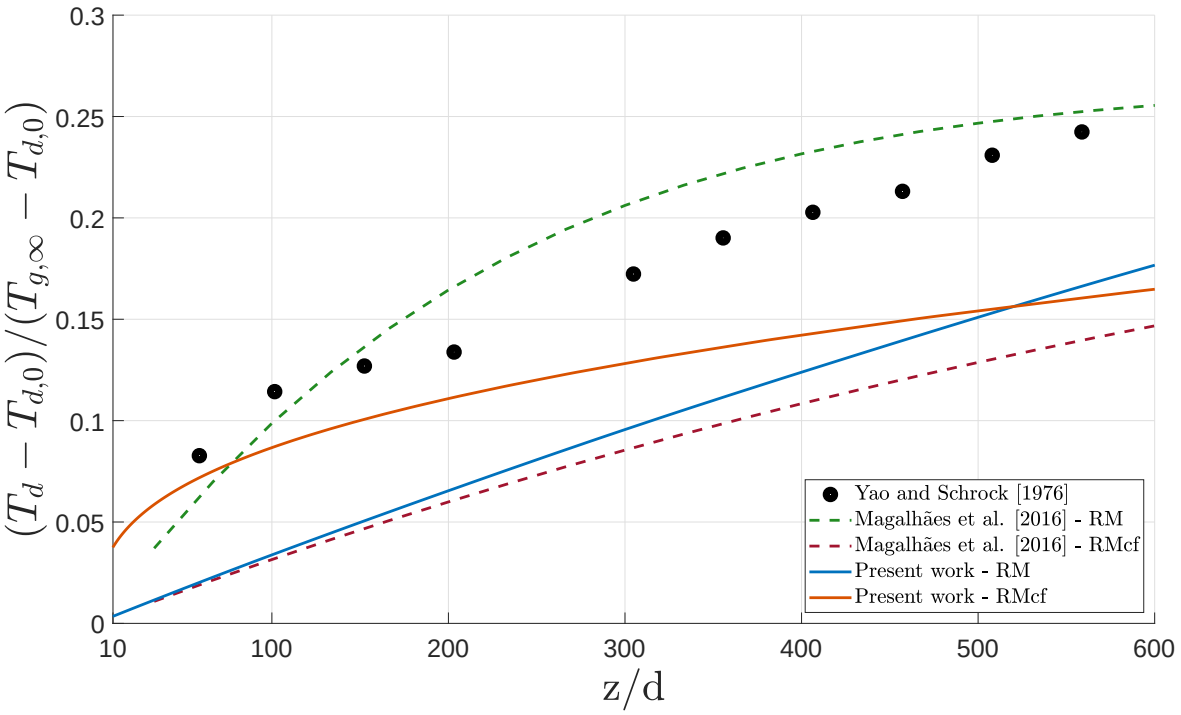

Figure 5.4: Variation on a single water droplet temperature, falling through the air, with a diameter of $3\,\mathrm{mm}$ and an air humidity ratio of 0.29 for both Ranz-Marshall correlations.

This suggests that for lower falling distances, up to 80 diameters, the mutual interaction between the droplet and the surrounding environment is predominant. The same happens for the vibrations and deformations of the droplet. However, from that falling height, that mutual interaction can be neglected and the complete mixing model is a valid assumption. The one-way coupling model results, using the corrected formulation, and the two-way coupling model resorting to the complete mixing model assumption, fails to predict the cooling phenomenon, underestimating it largely.

Having briefly described how figures are structured and how they should be analyzed, in this

section, the influence of a variable humidity ratio considering a constant droplet diameter on the cooling process of a free-falling water droplet is analyzed. On the other hand, Section 5.5 analyzes the influence on the temperature profile of a cooling droplet considering a constant air humidity ratio and a variable droplet diameter.

5.4.1 Diameter of 3 mm

Table 5.3 synthesizes the initial conditions performed on the experimental study, carried out by Yao and Schrock [1976], for the cases corresponding to a diameter of 3 mm. When comparing these cases, the principal characteristic that differs them consists of the different humidity ratios used, which vary from a low water vapor content up to the saturation point.

Table 5.3: Initial conditions performed on the experimental study of heat and mass transfer of freely falling droplets, for a 3 mm diameter droplet.

Case	Droplet diameter [mm]	Humidity ratio	Initial droplet temperature [K]	Environment temperature [K]
1	3	0.29	313.85	296.44
2	3	0.36	313.88	295.47
3	3	1.00	313.84	296.48

Figure 5.5 represents the temperature profile of a single droplet falling through the air with a diameter of 3 mm and a variable humidity ratio, using the Ranz-Marshall classical formulation. On the other hand, Figure 5.6 uses the Ranz-Marshall correlation with a correction factor.

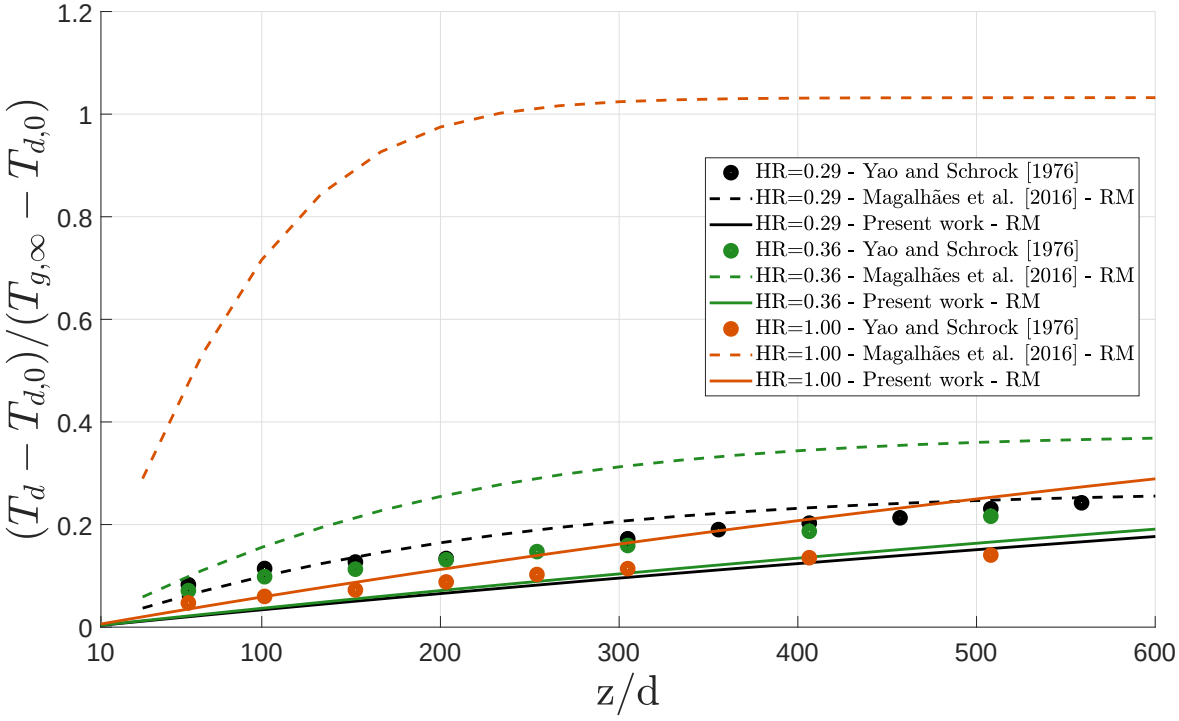

Figure 5.5: Variation on a single water droplet temperature, falling through the air, with a diameter of 3 mm and a variable air humidity ratio, resorting to the Ranz-Marshall correlation.

Analyzing Figure 5.5, for a humidity ratio of 0.29, the results obtained by resorting to the one-way coupling model show close agreement with the experimental data. For the same humidity ratio, the two-way coupling results are, as well, in agreement with the Yao and Schrock [1976] however, this methodology underestimates the cooling phenomenon.

When considering an intermediate level of humidity, 0.36, the results gathered by Magalhães et al. [2016] overestimate the cooling phenomenon for the entire experimental domain. However, when considering small falling heights up to 80 diameters, this method shows close agreement with experimental data. For the two-way coupling model, the numerical results underestimate the phenomenon for the entire domain. However, this second methodology shows, generically, better results when compared to the one-way coupling model results, bearing in mind that neither of the studies precisely predicts the phenomenon.

For the highest humidity ratio, 1.00, the results obtained when considering the one-way coupling methodology fails to predict the experimental data, overestimating it largely. Nevertheless, the model used in this study shows a close agreement with the data gathered by Yao and Schrock [1976], especially for a falling height up to 150 diameters, replicating the experimental data. From that point on this model overestimates the cooling phenomenon.

When analyzing Figure 5.6, for a humidity ratio of 0.29, it is seen that the one-way coupling model does not constitute a reliable way to predict the experimental data prediction when compared to the two-way coupling model. For this case, the method implemented in this study has a better agreement with the experimental data, especially for a falling height up to approximately 250 diameters. For the rest of the domain the phenomenon is underestimated.

At an intermediate level of humidity, 0.36, both models show close agreement when compared to the data obtained by Yao and Schrock [1976]. However, the two-way coupling model has better accuracy up to a falling height of 310 diameters. From that height on, the work performed by Magalhães et al. [2016], even underestimating the phenomena, outperforms the two-way coupling model.

For a humidity ratio of 1.00, the one-way coupling model fails to predict the cooling phenomenon. However, for this case, the two-way coupling model, even overestimating the phenomenon, follows the experimental data tendency.

When observing, together, Figures 5.5 and 5.6, it is possible to sense the influence of the droplet vibrations and deformations on the cooling phenomenon since a comparison between the complete mixing model and the mixing model assumption is made.

Considering Table 5.3 and the figures previously mentioned, it can be concluded that for the first case, resorting to the one-way coupling model combined with the Ranz-Marshall

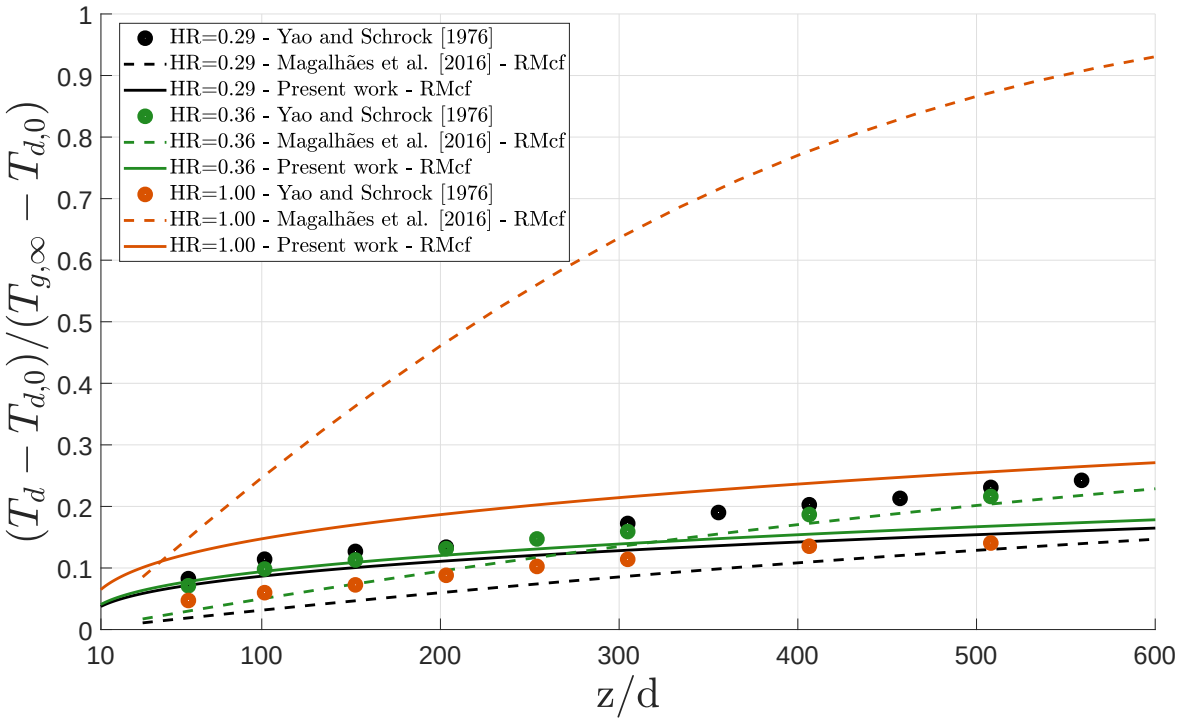

Figure 5.6: Variation on a single water droplet temperature, falling through the air, with a diameter of $3\,\mathrm{mm}$ and a variable air humidity ratio, resorting to the Ranz-Marshall correlation with the correction factor.

classical formulation and, consequently, assuming a complete mixing model, constitutes the best way of resembling the experimental data when considering a droplet of $3\,\mathrm{mm}$ and humidity ratio of 0.29. Nevertheless, up to a falling distance of 80 diameters the two-way coupling combined with the mixing model assumption predicts the cooling phenomenon in a better way.

For the second case, the mixing model formulation outperforms the numerical results obtained assuming a complete mixing model. Nevertheless, for a falling height up to 310 diameters the two-way coupling shows close agreement with data gathered by Yao and Schrock [1976], and from that point on the one-way coupling model shows to be a better option.

For the third case, the two-way coupling shows to be a better approach. For a falling height up to 510 diameters, the Ranz-Marshall classical formulation, which considers a complete mixing model, resembles the experimental results in a better way, however from that point on is the mixing model formulation that is closer to the experimental data.

5.4.2 Diameter of $4\,\mathrm{mm}$

On Table 5.4 are summarized the initial conditions performed, by Yao and Schrock [1976], for the cases corresponding to a diameter of $4\,\mathrm{mm}$. As previously the principal characteristic, when comparing the different cases, is on the different humidity ratios.

Considering Figure 5.7, which represents the temperature profile of a single water droplet,

Table 5.4: Initial conditions performed on the experimental study of heat and mass transfer of freely falling droplets, for a 4 mm diameter droplet.

Case	Droplet diameter [mm]	Humidity ratio	Initial droplet temperature [K]	Environment temperature [K]
4	4	0.36	313.89	295.59
5	4	0.52	313.79	294.48
6	4	1.00	313.94	296.48

on a free fall, with a diameter of 4 mm and a variable humidity ratio, using the classical formulation of Ranz-Marshall, it is seen that for the lowest humidity content, 0.36, the two-way coupling model, which accounts for the mutual interaction between the droplet and the surrounding environment, resembles the experimental data in a better way. However, this model underestimates the cooling phenomenon for the entire domain. The one-way coupling model, for this case, only shows proximity with the data gathered by Yao and Schrock [1976] for falling heights up 50 diameters. From that point on, the model fails to predict the phenomenon.

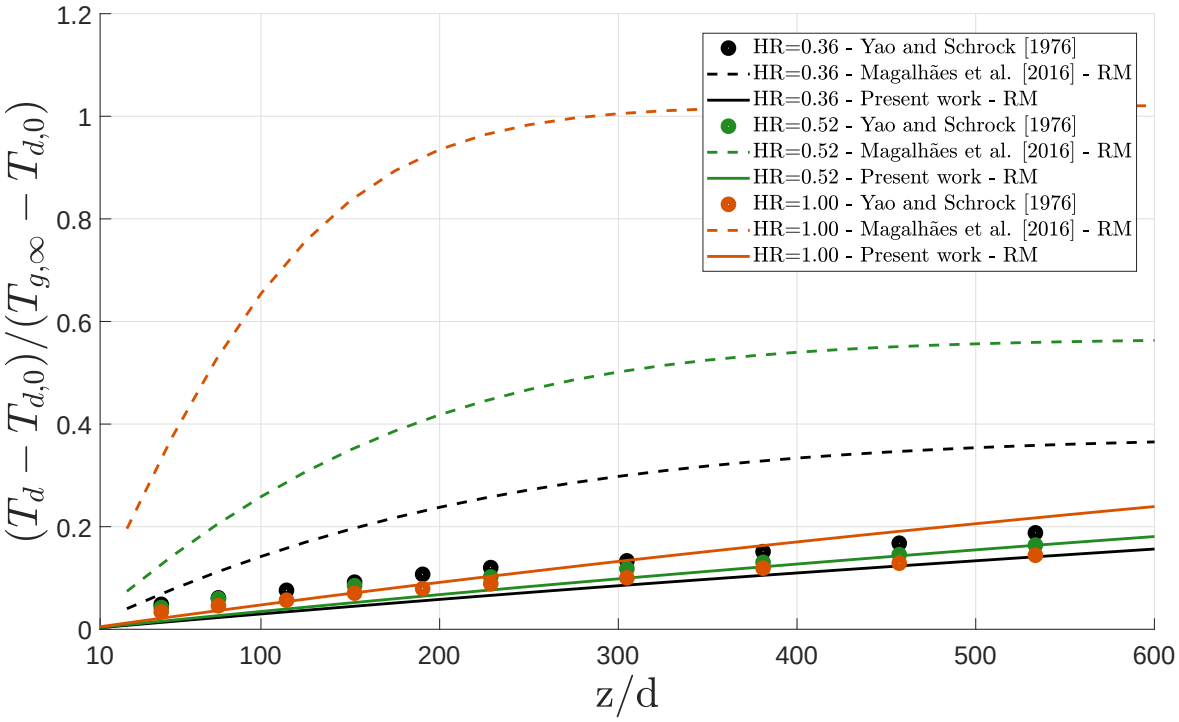

Figure 5.7: Variation on a single water droplet temperature, falling through the air, with a diameter of 4 mm and a variable air humidity ratio, resorting to the Ranz-Marshall correlation.

For a humidity ratio of 0.52, the one-way coupling model does not predict the cooling of water droplets, overestimating the phenomenon largely. Nevertheless, the two-way coupling shows a close agreement with experimental data, although underestimating it for small falling heights.

Considering a humidity ratio of 1.00, the results obtained by Magalhães et al. [2016] also

fails to predict the phenomenon and, the two-way coupling model generally resembles the experimental data, especially for heights up to 200 diameters. From that point on, this model, even maintaining close proximity, overestimates the phenomenon.

Figure 5.8 represents the variation on a single droplet temperature, with a diameter of 4 mm and three distinct humidity ratios (0.36, 0.52, and 1.00), resorting to the Ranz-Marshall correlation with the correction factor, which considers a mixing model formulation.

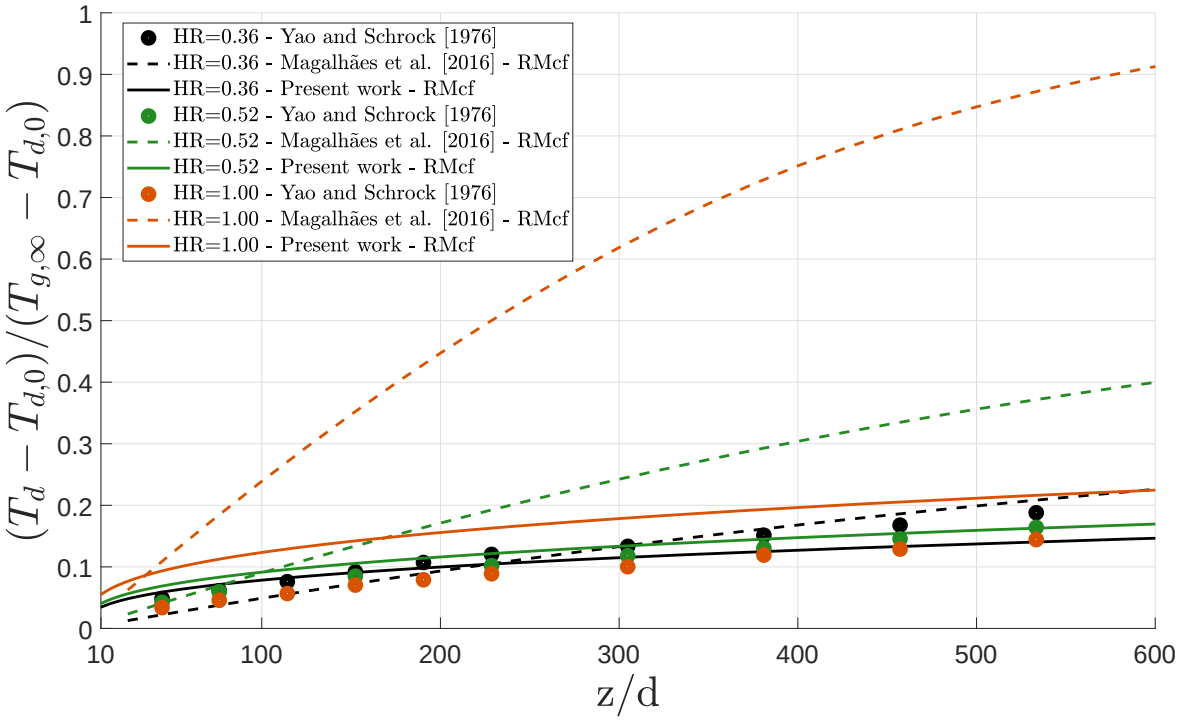

Figure 5.8: Variation on a single water droplet temperature, falling through the air, with a diameter of 4 mm and a variable air humidity ratio, resorting to the Ranz-Marshall correlation with the correction factor.

For a humidity ratio of 0.36, the results obtained by the two-way coupling model are in close agreement with experimental data for a falling height up to 230 diameters. From that point on, the work performed by Magalhães et al. [2016] outperforms the current one and, the one-way coupling model results resemble the experimental ones in a better way even overestimating the cooling phenomenon.

When examining the intermediate level of humidity, 0.52, it is seen that the one-way coupling model shows a close agreement with the experimental data for a falling height up to 100 diameters. From that point on this model overestimates the cooling phenomenon and the two-way coupling model resembles the data gathered by Yao and Schrock [1976] in a better way, outperforming the previous model. This second formulation follows precisely the experimental data tendency.

Finally, for a humidity ratio of 1.00, the two-way coupling model constitutes, generically, a reliable approach to predict the cooling of a water droplet on a free fall, although overestimating it. The one-way coupling model does not predict the phenomenon

accurately enough.

Figures 5.7 and 5.8 allow a comparison between the two formulations of the Ranz-Marshall correlations for the conditions presented in Table 5.4. Considering the fourth case, the mixing model assumption outperforms the numerical results obtained assuming a complete mixing model. However, for a falling height lower than 230 diameters, the two-way coupling model shows better agreement relative to experimental data. From that point on, the work developed by Magalhães et al. [2016] resembles that data in a better way.

For the fifth case, a combination of hypotheses happens. Considering a falling height lower than 100 diameters, the one-way coupling model resorting to the mixing model formulation shows better results relative to all formulations, indicating the predominance of the vibrations and distortions. From this point on, the interaction between the droplet and the surrounding environment appears to be a determinant factor since the two-way coupling model resembles the experimental data in a better way. Up to a falling height of 400 diameters, the numerical results obtained considering the mixing model formulation, which accounts for vibrations and deformations of droplets, can replicate the experimental data. From that point on, the complete mixing model predicts the experimental data in a better way, suggesting a steady-state condition.

Considering the sixth case, the two-way coupling methodology outperforms the predictions accomplished by Magalhães et al. [2016] suggesting the necessity of accounting for the mutual interactions between the droplets and the surrounding environment. Up to a falling height of 550 diameters, the complete mixing model resembles the experimental data in a better way. From that point on, droplet vibrations and distortions become predominant, since the Ranz-Marshall corrected formulation shows a close agreement with the experimental data indicating the presence of a transient regime.

5.4.3 Diameter of $5\,\mathrm{mm}$

Table 5.5 summarizes the initial conditions performed on the experimental study, accomplished by Yao and Schrock [1976], for the cases corresponding to a diameter of $5\,\mathrm{mm}$. As previously the principal difference, when comparing the cases, is on the different humidity ratios used.

Table 5.5: Initial conditions performed on the experimental study of heat and mass transfer of freely falling droplets, for a $5\,\mathrm{mm}$ diameter water droplet.

Case	Droplet diameter [mm]	Humidity ratio	Initial droplet temperature [K]	Environment temperature [K]
7	5	0.29	313.83	296.03
8	5	0.36	313.87	295.71
9	5	1.00	313.89	296.76

Figure 5.9 represents the variation on a single water droplet temperature, falling through the

air, with a diameter of $5\,\mathrm{mm}$ and a variable air humidity ratio, resorting to the Ranz-Marshall correlation. On the other hand, the results in Figure 5.10 use the corrected Ranz-Marshall correlation.

As it is seen in Figure 5.9, for the lowest humidity ratio, 0.29, the two-way coupling model underestimates the cooling phenomenon and fails to predict it. Nevertheless, the one-way coupling model shows a good agreement with experimental data, especially for heights up to 120 diameters predicting the phenomenon precisely. For the rest of the experimental domain, this model overestimates the phenomenon, but still follows the experimental data tendency.

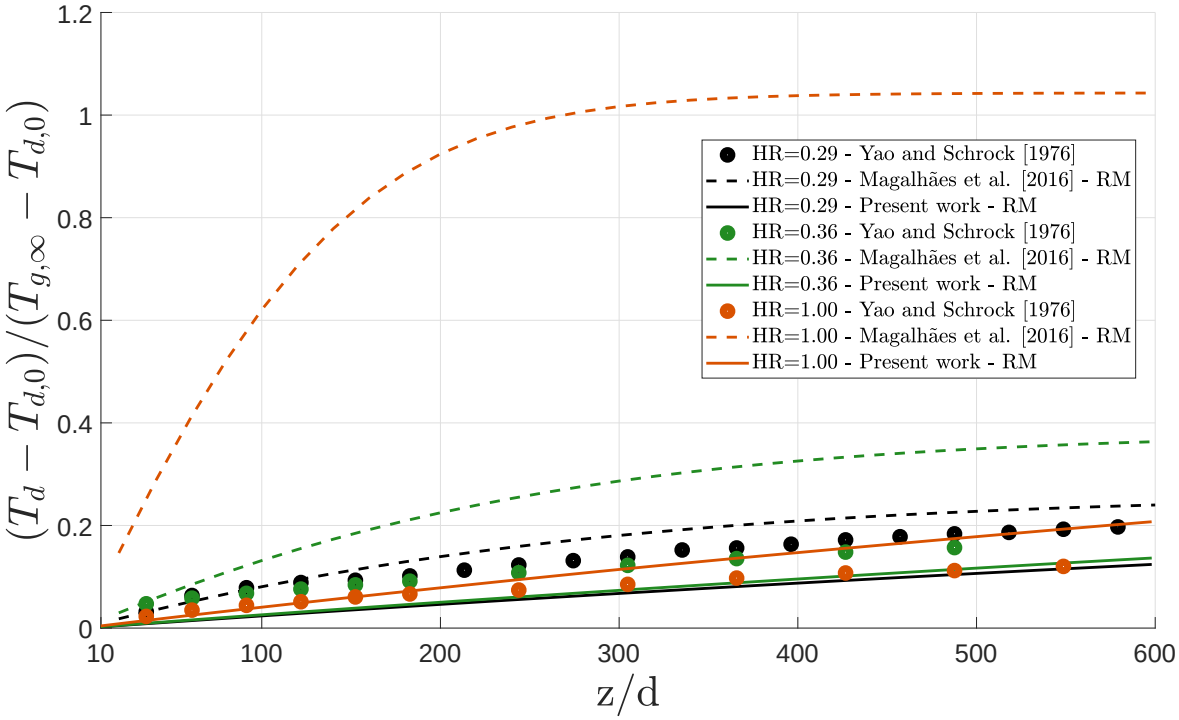

Figure 5.9: Variation on a single water droplet temperature, falling through the air, with a diameter of $5\,\mathrm{mm}$ and a variable air humidity ratio, resorting to the Ranz-Marshall correlation.

Considering a humidity ratio of 0.36, the work developed by Magalhães et al. [2016] shows a good agreement with experimental data up to a falling height of 100 diameters, suggesting that the mutual interaction between the droplet and the surrounding environment does not play a fundamental role up to this point. From that point on, the two-way coupling model resembles the data gathered by Yao and Schrock [1976] in a better way. Thus, it is possible to assume that the mutual iteration has some implication on the final results and, for that reason, has to be accounted for.

Finally, when considering the highest humidity content, 1.00 is possible to see that the one-way coupling methodology fails to predict the experimental results suggesting that the mutual interaction between the droplet and the surrounding environment has to be accounted for. This fact is confirmed since the two-way coupling model precisely predicts the experimental data, up to a falling height of 190 diameters. From that point on, this

model overestimates the phenomenon but still follows the experimental tendency.

Figure 5.10, which uses a correction factor on the Ranz-Marshall correlation, shows that for a humidity ratio of 0.29, the results of the two-way coupling model show close agreement with experimental data up to a falling height of 100 diameters. From that falling height, this method underestimates the cooling phenomenon. Nevertheless, it still resembles the numerical data up to a falling height of 400 diameters. From that point on, the two-way coupling is outperformed by the work carried out by Magalhães et al. [2016] which suggests that the mutual interaction between the droplet and the surrounding environment fades away as the particle falls.

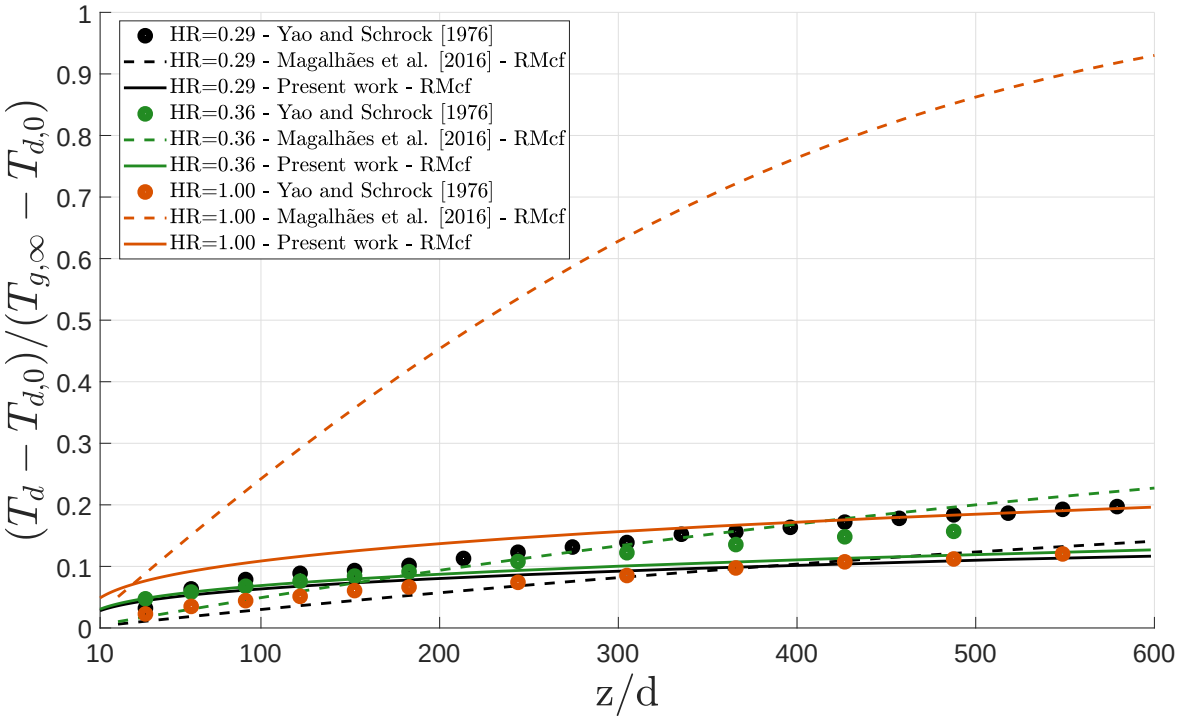

Figure 5.10: Variation on a single water droplet temperature, falling through the air, with a diameter of 5 mm and a variable air humidity ratio, resorting to the Ranz-Marshall correlation with the correction factor.

For a humidity ratio of 0.36, the two-way coupling model predicts the cooling phenomena more accurately up to a falling height of approximately 190 diameters. From that point on, it is the one-way coupling model which shows a closer agreement with the data gathered by Yao and Schrock [1976]. This suggests that the mutual interaction between the particle and the environment has predominance for higher falling heights, and can be neglected for smaller ones.

Finally, considering a humidity ratio of 1.00, the study carried out by Magalhães et al. [2016] fails to predict the phenomenon. Nevertheless, the two-way coupling model follows the experimental data tendency, overestimating the phenomenon for the entire domain.

When comparing the two Ranz-Marshall formulations, using Figures 5.9 and 5.10, it is possible to conclude that for the seventh case, the one-way coupling model, considering the

Ranz-Marshall classical formulation, shows the best agreement with experimental data when compared with other numerical results. This analysis suggests that, for these conditions, the mutual interaction between the particle and the surrounding environment does not play a fundamental role in the phenomenon and the complete mixing model is an acceptable assumption.

For the eighth case, the Ranz-Marshall corrected formulation shows a good agreement with the experimental results, suggesting a transient regime in which distortions and vibrations of the particle play a fundamental role. Nevertheless, for a falling height lower than 190 diameters, the two-way coupling model can resemble experimental data in a better way. From that falling height, the one-way coupling outperforms the previous model. This suggests that the mutual interaction between the droplet and the surrounding environment fades away along the falling height.

Finally, considering the ninth case, the results obtained by Magalhães et al. [2016] are outperformed by the two-way coupling data suggesting that for this humidity content, the mutual interaction between the particle and the surrounding environment plays a fundamental role. Additionally, the complete mixture model is an acceptable assumption for this case, revealing that the influence of vibrations and deformations can be neglected.

5.4.4 Diameter of $6\,\mathrm{mm}$

Table 5.6 summarizes the initial conditions performed on the experimental study carried out by Yao and Schrock [1976], for the cases corresponding to a diameter of $6\,\mathrm{mm}$.

Table 5.6: Initial conditions performed on the experimental study of heat and mass transfer of freely falling droplets, for a $6\,\mathrm{mm}$ diameter water droplet.

Case	Droplet diameter [mm]	Humidity ratio	Initial droplet temperature [K]	Environment temperature [K]
10	6	0.36	313.89	295.29
11	6	0.52	313.81	294.48
12	6	1.00	313.85	296.48

Figure 5.11 corresponds to the temperature profile of a single water droplet, falling through the air, with a diameter of $6\,\mathrm{mm}$ and a variable air humidity ratio, resorting to the Ranz-Marshall correlation.

For a humidity ratio of 0.36, it is seen that the one-way coupling model, for a falling height up to 50 diameters outperforms the results that use the two-way coupling model. However, from that point on, the two-way coupling model shows a close agreement with experimental data. Nevertheless, it is important to notice that the results from Magalhães et al. [2016] overestimate the phenomenon for the rest of the domain in contrast to the two-way coupling data that underestimates it.

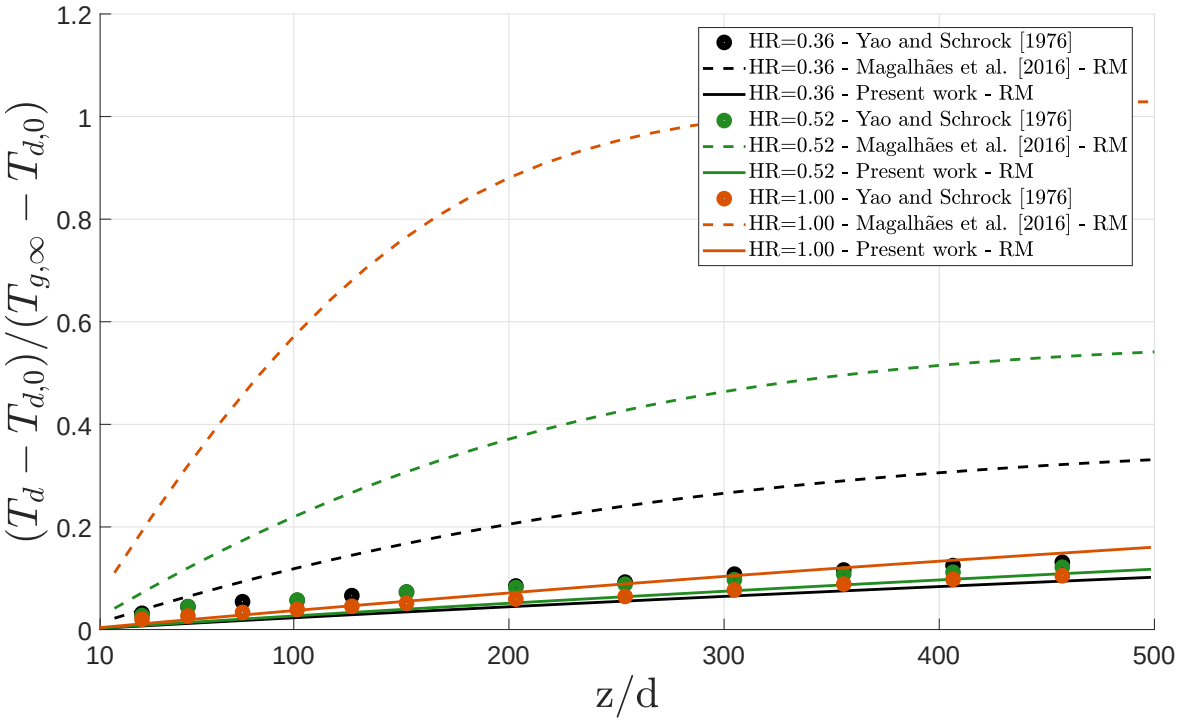

Figure 5.11: Variation on a single water droplet temperature, falling through the air, with a diameter of $6\,\mathrm{mm}$ and a variable air humidity ratio, resorting to the Ranz-Marshall correlation.

Considering a humidity ratio of 0.52, it becomes obvious that the two-way coupling results are in closer agreement with experimental data when compared with the one-way coupling data that does not predict accurately the cooling phenomenon. This suggests that when a complete mixture model is assumed the interaction between the droplet and the surrounding environment has to be taken into account.

Finally, for the highest humidity ratio, 1.00, as it happened previously, the one-way coupling model fails to predict the cooling phenomenon. However, the two-way coupling predicts the phenomenon, precisely, up to a falling height of 150 diameters. From that point on, this model is still reliable but slightly overestimates the phenomenon.

Figure 5.12 represents the temperature profile on a single water droplet, falling through the air, with a diameter of $6\,\mathrm{mm}$ and a variable air humidity ratio, resorting to the Ranz-Marshall correlation with the correction factor.

For a humidity ratio of 0.36, both models are in close agreement compared to experimental data. Even so, the two-way coupling approach has higher accuracy, especially up to a falling height of 160 diameters, where the numerical data follows up, precisely, the data gathered by Yao and Schrock [1976]. From that point on, it is indifferent the model chosen to represent the cooling process since the work performed by Magalhães et al. [2016] overestimates the phenomenon and, the two-way coupling underestimates it but in a similar proportion.

For a humidity ratio of 0.52, the one-way coupling methodology seems to resemble the

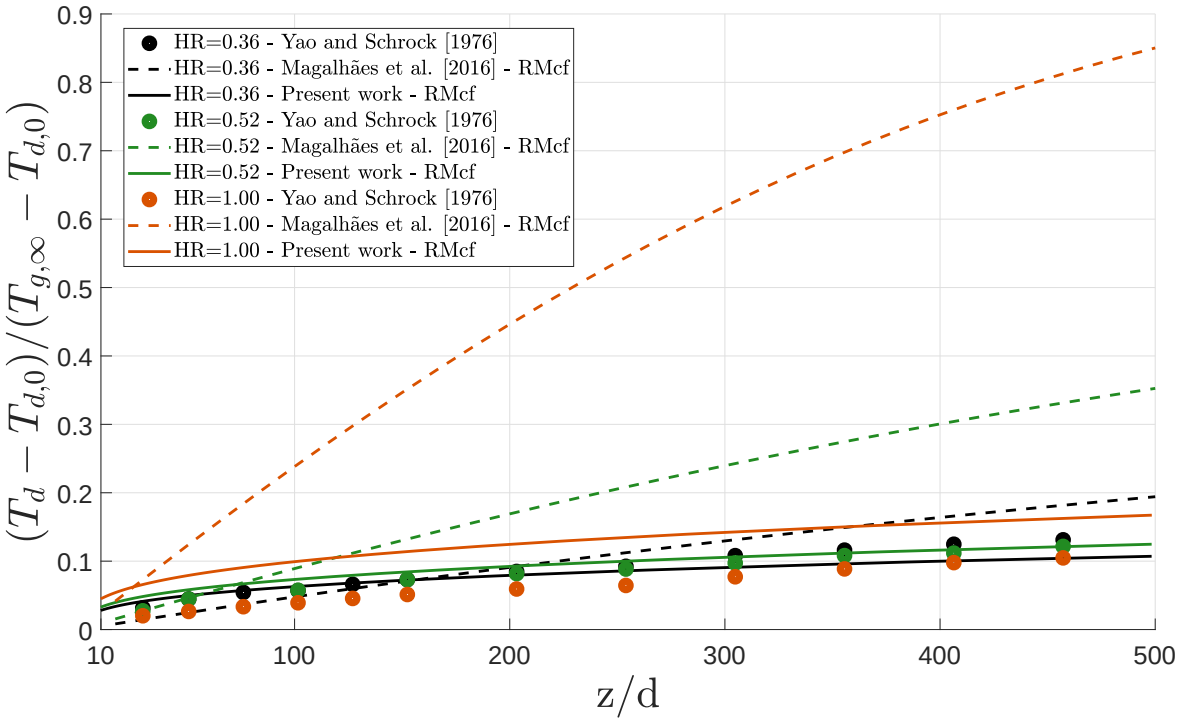

Figure 5.12: Variation on a single water droplet temperature, falling through the air, with a diameter of $6\,\mathrm{mm}$ and a variable air humidity ratio, resorting to the Ranz-Marshall correlation with the correction factor.

experimental data up to a falling height of 70 diameters. However, from that point on, that model largely overestimates the cooling phenomenon whereas, the two-way coupling model maintains the accuracy for the rest of the experimental domain, predicting the phenomenon precisely.

Finally, for a humidity ratio of 1.00, the model developed by Magalhães et al. [2016] fails to predict the phenomenon. Yet, the two-way coupling model can foresee the cooling with accuracy, albeit overestimating it.

To comprehend the influence of the Ranz-Marshall formulation used on predicting experimental data, the numerical results of Figures 5.11 and 5.12 were compared. For the tenth case, examining Table 5.6, the mixing model formulation is the one that has a close agreement with experimental data. Therefore, it is possible to conclude that, for this case, the effects of vibrations and deformations have to be accounted for. The mutual effects between the particle and the surrounding environment are experienced up to a falling height of 160 diameters since up to that height, the two-way coupling model resembles the experimental data in a better way. From that point on, the difference between both models is indistinguishable, suggesting the existence of a transition zone.

When examining the eleventh case, a similar situation occurs. The Ranz-Marshall corrected formulation is the one that resembles the data gathered by Yao and Schrock [1976] in a better way. This suggests that the mixture model assumption works for these conditions. The one-way coupling model has a close agreement with the experimental results up to a falling height

of 70 diameters. From that point on, the mutual interaction between the droplet and the surrounding environment has a significant importance.

Finally, for the twelfth case, both the complete mixture model assumption and the two-way coupling model constitute the option that shows the closest agreement with experimental data. Therefore, for this condition, it can be assumed that the mutual interaction between the particle and the surrounding environment plays an important role in the phenomenon, and the vibrations and distortions can be neglected.

5.5 Influence of a variable droplet diameter with a constant humidity ratio

5.5.1 Humidity ratio of 0.29

Table 5.7 represents the initial conditions performed on the experimental study of heat and mass transfer of freely falling droplets, carried out by Yao and Schrock [1976], considering a humidity ratio of 0.29. As it is seen, case one corresponds to a droplet diameter of 3 mm, and case seven to a droplet diameter of 5 mm.

Table 5.7: Initial conditions performed on the experimental study of heat and mass transfer of freely falling droplets considering a humidity ratio of 0.29.

Case	Droplet diameter [mm]	Humidity ratio	Initial droplet temperature [K]	Environment temperature [K]
1	3	0.29	313.85	296.44
7	5	0.29	313.83	296.03

Figure 5.13 represents the temperature profile of a single water droplet, falling through the air, with an air humidity ratio of 0.29 and a variable droplet diameter, using the Ranz-Marshall correlation on its classical formulation. Figure 5.14 represents the same temperature profile but considering the Ranz-Marshall corrected formulation.

Analyzing Figure 5.13, the numerical results from the one-way coupling have a closer agreement with experimental data when compared with the two-way coupling model. Considering a droplet diameter of 3 mm, the results obtained by Magalhães et al. [2016] have good correspondence with experimental data up to a falling height of 150 diameters and then from 550 diameters up to the end of the domain. Between those distances, the cooling phenomena is overestimated, but these results still outperform the ones obtained by using the two-way coupling model.

Considering a droplet diameter of 5 mm, the one-way coupling methodology follows the experimental data temperature tendency. Up to a falling distance of 120 diameters, this model precisely follows the data gathered by Yao and Schrock [1976]. From that point on, the one-way coupling still shows close proximity with the experimental data but

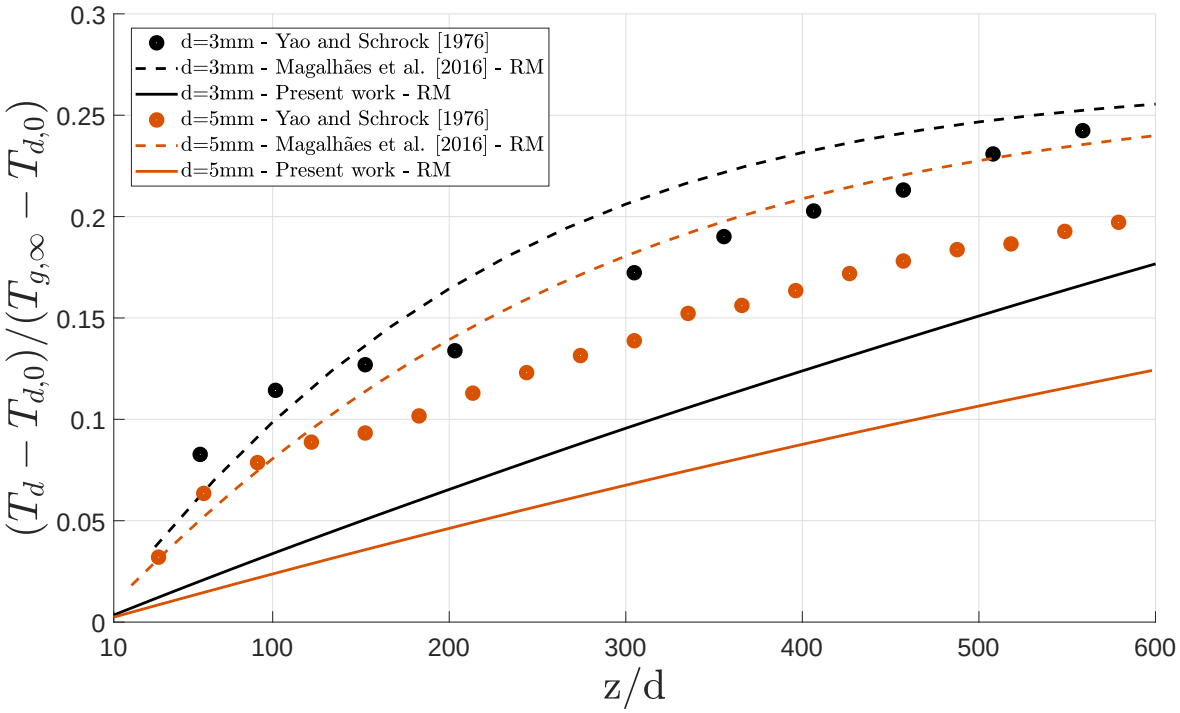

Figure 5.13: Variation on a single water droplet temperature, falling through the air, subjected to a humidity ratio of 0.29 using the classical Ranz-Marshall formulation.

overestimates the cooling phenomenon.

This suggests that when considering a complete mixing model assumption, the mutual interaction between the droplet and the surrounding environment has predominance on small falling heights and as the droplet travels through the domain, that influence fades away. However, for a diameter of $3\,\mathrm{mm}$ it seems that such influence regains predominance as the falling height increases.

Observing Figure 5.14, the numerical data from the one-way coupling model underestimate the cooling phenomenon for both studied diameters. When considering the two-way coupling model, the results show a close agreement with the experimental data up to approximately 50 diameters. However, from that point on, the numerical data diverge from the results gathered by Yao and Schrock [1976] underestimating the phenomenon, for both diameters, for the rest of the domain.

Therefore, when considering a mixing model, it can be assumed that for lower falling heights the mutual influence between the droplet and the surrounding environment plays an important role. However, that influence fades away as the falling height increases.

When comparing the two Ranz-Marshall formulations, using Figures 5.13 and 5.14, the classical formulation shows close agreement when compared to the experimental data, for both numerical studies, suggesting that vibrations and deformations do not have predominance in these cases. Additionally, the one-way coupling model resembles the

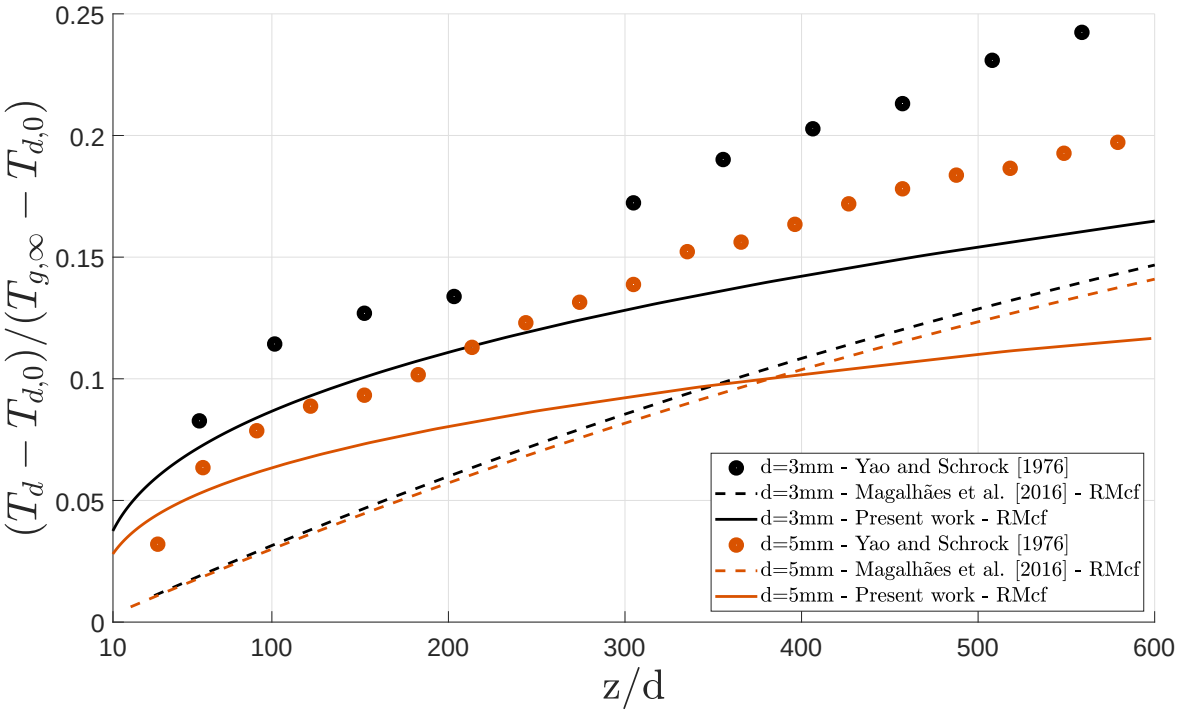

Figure 5.14: Variation on a single water droplet temperature, falling through the air, subjected to a humidity ratio of 0.29 using the Ranz-Marshall correlation with the correction factor.

experimental data in a better way when compared with the two-way coupling model, which indicates that for a humidity ratio of 0.29, the mutual interaction between the droplet and the surrounding environment can be neglected.

5.5.2 Humidity ratio of 0.36

On Table 5.8 are summarized the initial conditions performed, by Yao and Schrock [1976], for the cases corresponding to a humidity ratio of 0.36. Four distinct diameters (3 mm, 4 mm, 5 mm, and 6 mm) were used when considering this air humidity ratio.

Table 5.8: Initial conditions performed on the experimental study of heat and mass transfer of freely falling droplets, considering a humidity ratio of 0.36.

Case	Droplet diameter [mm]	Humidity ratio	Initial droplet temperature [K]	Environment temperature [K]
2	3	0.36	313.88	295.47
4	4	0.36	313.89	295.59
8	5	0.36	313.87	295.71
10	6	0.36	313.89	295.29

Figure 5.15 represents the variation on a single water droplet temperature, falling through the air, subjected to a humidity ratio of 0.36 using the classical Ranz-Marshall formulation. For all the diameters studied, the one-way coupling model is in close agreement with the experimental data up to a falling height of 50 diameters. However, from that falling height on, the numerical results performed by Magalhães et al. [2016] tend to overestimate largely

data gathered experimentally. Nonetheless, the two-way coupling model shows a closer agreement with the obtained by Yao and Schrock [1976]. Even so, this model is not capable of mimicking the experimental data, underestimating the cooling phenomenon.

This suggests that when considering a complete mixing model, the mutual interaction between the particle and the surrounding environment can be neglected for small falling heights but, it becomes predominant as the falling height increases.

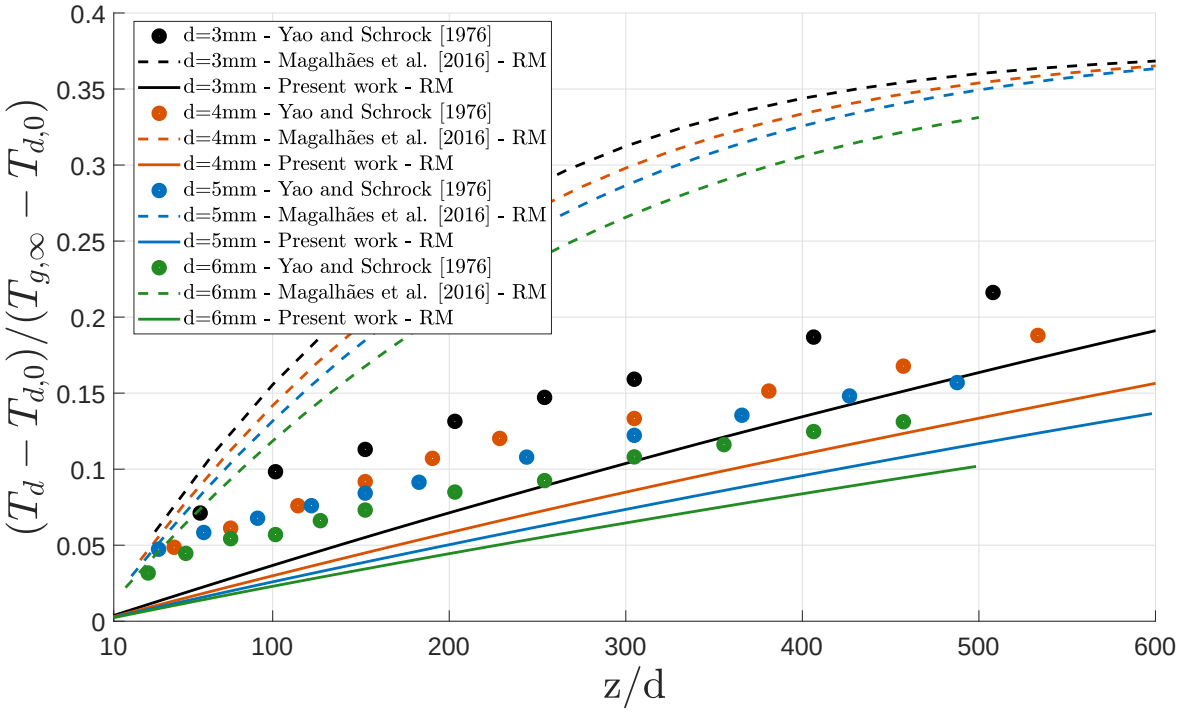

Figure 5.15: Variation on a single water droplet temperature, falling through the air, subjected to a humidity ratio of 0.36 using the classical Ranz-Marshall formulation.

Observing Figure 5.16, which represents the temperature profile, using the Ranz-Marshall corrected formulation, of a single water droplet falling through the air, considering a humidity ratio of 0.36, it is possible to see that for a diameter of $3\,\mathrm{mm}$ the two-way couple model shows close agreement with experimental data up to a falling height of 310 diameters. From that point on, the numerical results presented by Magalhães et al. [2016] predict the experimental data more accurately.

When examining a diameter of $4\,\mathrm{mm}$, a similar situation occurs but, this time, the falling height, in which the change between the two models occurs, is smaller. Up to a falling height of 230 diameters, the two-way coupling model is the one that represents the cooling phenomenon more accurately. From that point on is the one-way coupling model that shows close agreement with experimental data.

For a diameter of $5\,\mathrm{mm}$, the two-way coupling model predicts with more accuracy the experimental results up to a falling height of 190 diameters and, from that point on is the numerical data gathered by Magalhães et al. [2016], which closely represents the

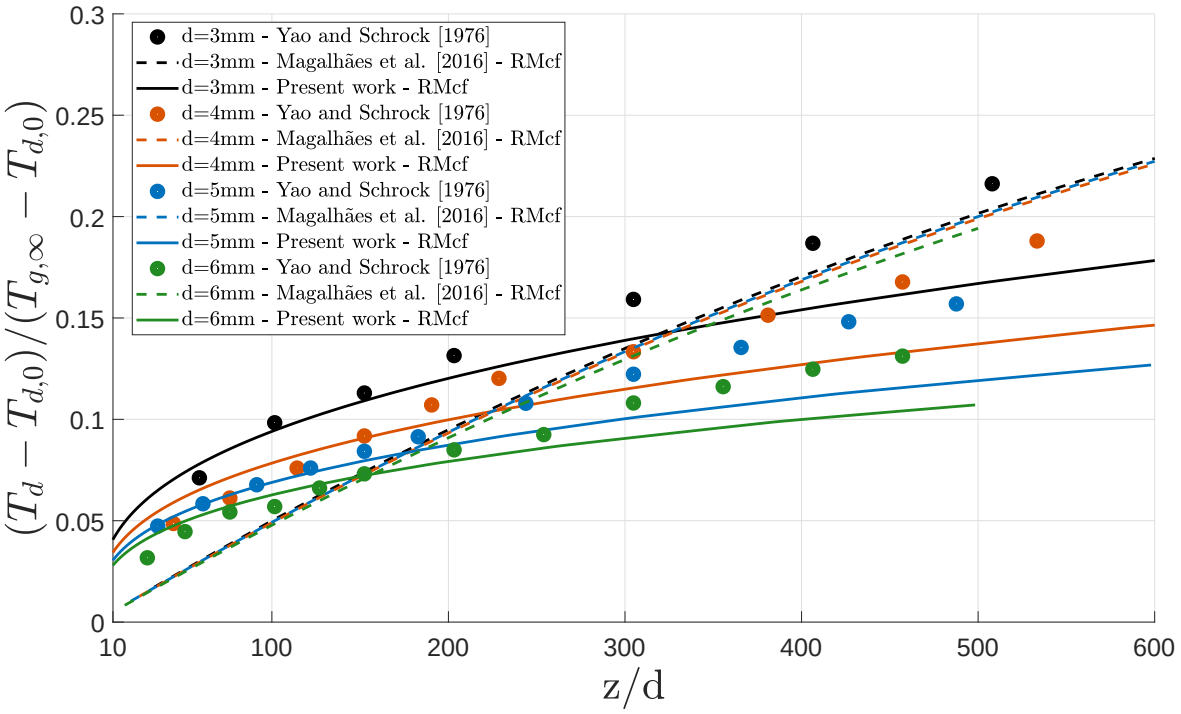

Figure 5.16: Variation on a single water droplet temperature, falling through the air, subjected to a humidity ratio of 0.36 using the Ranz-Marshall correlation with the correction factor.

experimental study performed by Yao and Schrock [1976].

Finally, for a diameter of $6\,\mathrm{mm}$, it is seen that the two-way coupling model is the one that shows the closest agreement with experimental data for the entire domain.

After comparing Figures 5.15 and 5.16, it is possible to state that the assumption of a mixing model is the one that shows better results when compared with the classical formulation for all diameters available. Additionally, it is seen that for a humidity ratio of 0.36 and a droplet diameter of $6\,\mathrm{mm}$ the mutual effect between the particle and the surrounding environment has to be considered for the whole domain. For the remaining diameters, $3\,\mathrm{mm}$, $4\,\mathrm{mm}$, and $5\,\mathrm{mm}$ this mutual influence becomes less predominant as the diameter increases.

5.5.3 Humidity ratio of 0.52

Table 5.9 represents the initial conditions performed on the experimental study of heat and mass transfer of freely falling droplets, carried out by Yao and Schrock [1976], for a humidity ratio of 0.52. As it is seen, case five corresponds to a droplet diameter of $4\,\mathrm{mm}$, while case eleven corresponds to a diameter of $6\,\mathrm{mm}$.

Figure 5.17 represents the temperature profile on a single water droplet, falling through the air, with a humidity ratio of 0.52 and a variable droplet diameter, resorting to the Ranz-Marshall correlation on its classical formulation. Figure 5.18 represents the same temperature profile using instead the Ranz-Marshall corrected formulation.

Table 5.9: Initial conditions performed on the experimental study of heat and mass transfer of freely falling droplets, considering a humidity ratio of 0.52.

Case	Droplet diameter [mm]	Humidity ratio	Initial droplet temperature [K]	Environment temperature [K]
5	4	0.52	313.79	294.48
11	6	0.52	313.81	294.48

Observing Figure 5.17 it is seen that the one-way coupling fails to predict the cooling phenomenon, overestimating it considerably for the entire experimental domain. This consideration is valid for all diameters involved (4 mm and 6 mm). However, the two-way coupling model appears to have a close agreement with experimental data, especially for higher falling heights. For instance, for the fifth case, from a falling height of 400 diameters, the two-way coupling model precisely predicts the cooling phenomenon. For a droplet diameter of 6 mm, this model is not so accurate since it underestimates the phenomenon. However, it still presents great proximity with the data gathered by Yao and Schrock [1976]. This suggests, for a humidity ratio of 0.52, that the mutual influence between the particle and the surrounding environment has to be accounted for.

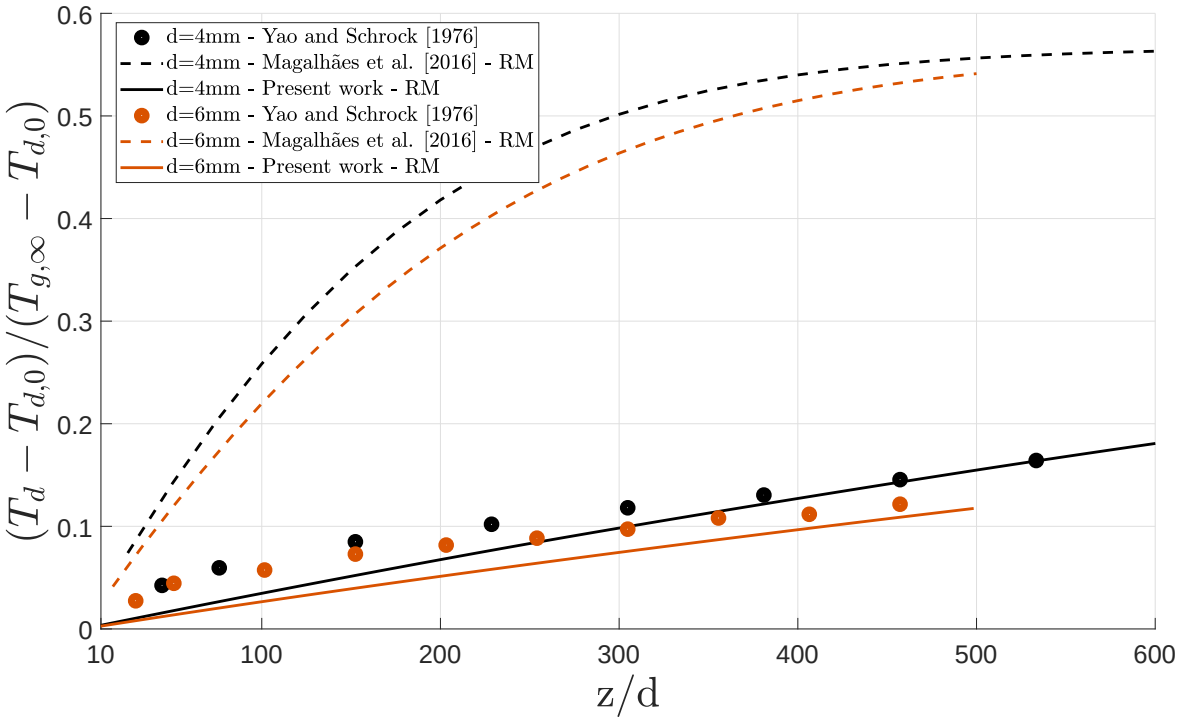

Figure 5.17: Variation on a single water droplet temperature, falling through the air, subjected to a humidity ratio of 0.52 using the Ranz-Marshall correlation.

Figure 5.18 shows that the results obtained using the two-way coupling model have overall proximity with the data gathered by Yao and Schrock [1976]. However, when considering small falling heights up to approximately 70 diameters, the one-way coupling model precisely simulates the cooling phenomenon. From that point on, this methodology fails to predict the phenomenon overestimating it by a large margin. Therefore, when considering

a mixing model assumption, the mutual influence between the droplet and the surrounding environment has to be accounted for large falling heights and can be neglected for smaller ones.

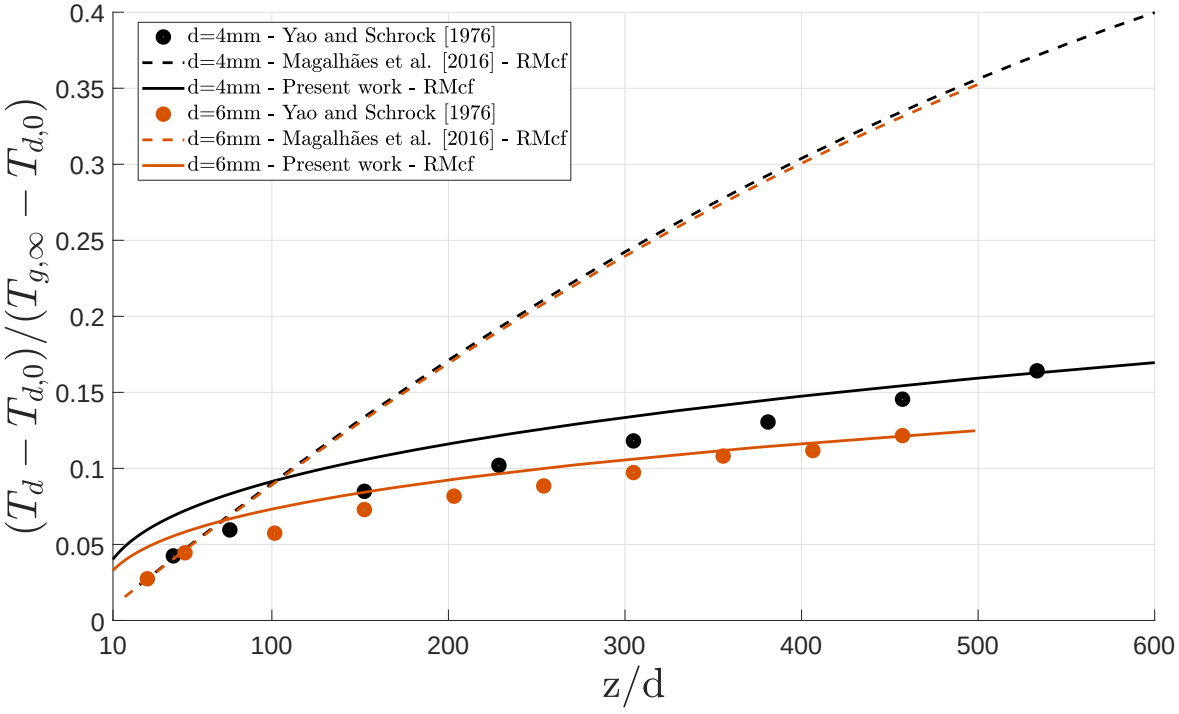

Figure 5.18: Variation on a single water droplet temperature, falling through the air, subjected to a humidity ratio of 0.52 using the Ranz-Marshall correlation with the correction factor.

Comparing Figure 5.17 and Figure 5.18, for a diameter of $4\,\mathrm{mm}$, the one-way coupling methodology, using a mixing model formulation, is the one that predicts the experimental data more accurately up to a falling height of 100 diameters. From that point up to a height of 400 diameters, the experimental data is represented, in a better way, by resorting to the two-way coupling model assuming that the vibrations and deformations still have an important role. For the remaining height, the mutual interaction between the droplet and the surrounding environment still plays an important role, however, is the complete mixing model assumption that presents good proximity with experimental results.

Finally, observing the results obtained for a diameter of $6\,\mathrm{mm}$ is the mixing model that best suits the experimental data. Up to a falling height of 70 diameters, the work performed by Magalhães et al. [2016] shows close agreement with experimental data, and from that point on, the mutual interaction between the droplet and the surrounding environment appears to have an important role since the two-way coupling model is the one who best suits the experimental results.

5.5.4 Humidity ratio of 1.00

Table 5.10 summarizes the initial conditions performed on the experimental study, carried out by Yao and Schrock [1976] for the cases corresponding to a humidity ratio of 1.00. Were examined four distinct cases for this condition, considering four distinct diameters

(3 mm, 4 mm, 5 mm, and 6 mm).

Table 5.10: Initial conditions performed on the experimental study of heat and mass transfer of freely falling droplets, considering a humidity ratio of 1.00.

Case	Droplet diameter [mm]	Humidity ratio	Initial droplet temperature [K]	Environment temperature [K]
3	3	1.00	313.84	296.48
6	4	1.00	313.94	296.48
9	5	1.00	313.89	296.76
12	6	1.00	313.85	296.48

Figure 5.19 represents the variation on a single water droplet temperature, falling through the air, subjected to a humidity ratio of 1.00 using the Ranz-Marshall correlation. It is observed that the one-way coupling model completely fails to predict the cooling phenomenon for all the diameters studied. This suggests that the mutual interaction between the particle and the surrounding environment has to be accounted for.

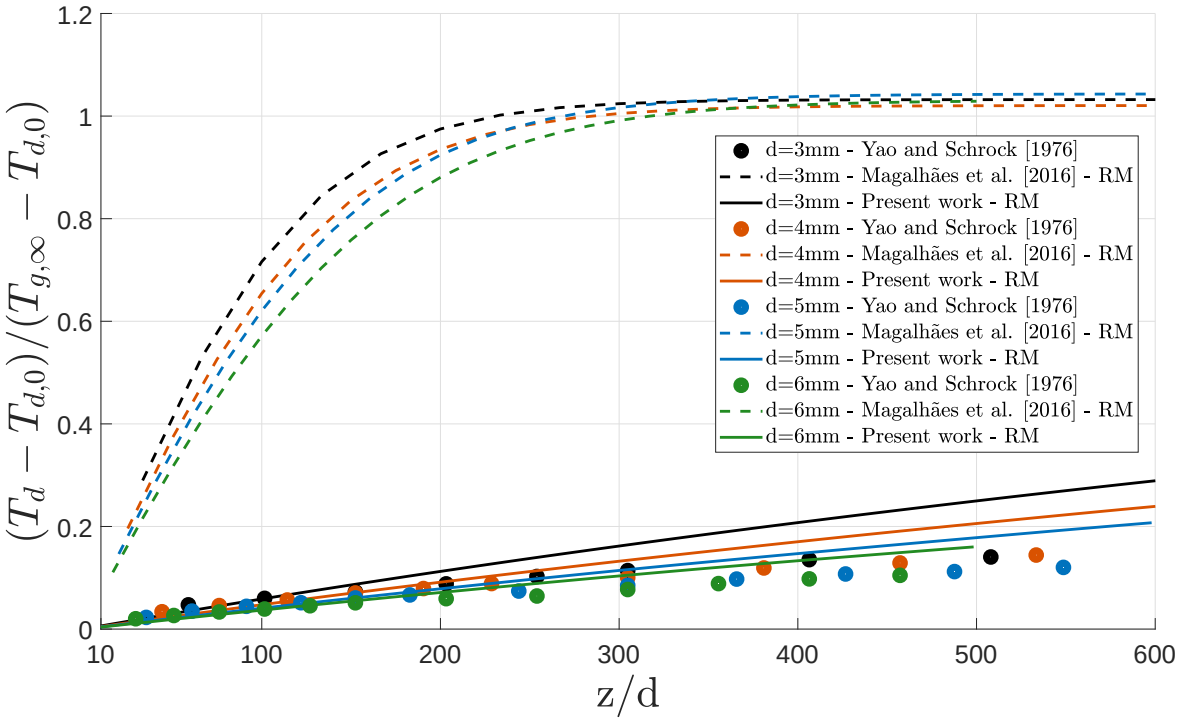

Figure 5.19: Variation on a single water droplet temperature, falling through the air, subjected to a humidity ratio of 1.00 using the Ranz-Marshall correlation.

Due to the wide range of values for the dimensionless temperature, Figure 5.20 is introduced to effectively observe and compare the two-way numerical simulation and the data gathered by Yao and Schrock [1976]. For small falling heights, up to 150 diameters, the two-way coupling model predicts the experimental data available precisely. From that point on, the model overestimates the cooling phenomenon for all diameters studied.

Observing Figure 5.21, which represents the temperature profile of a single droplet

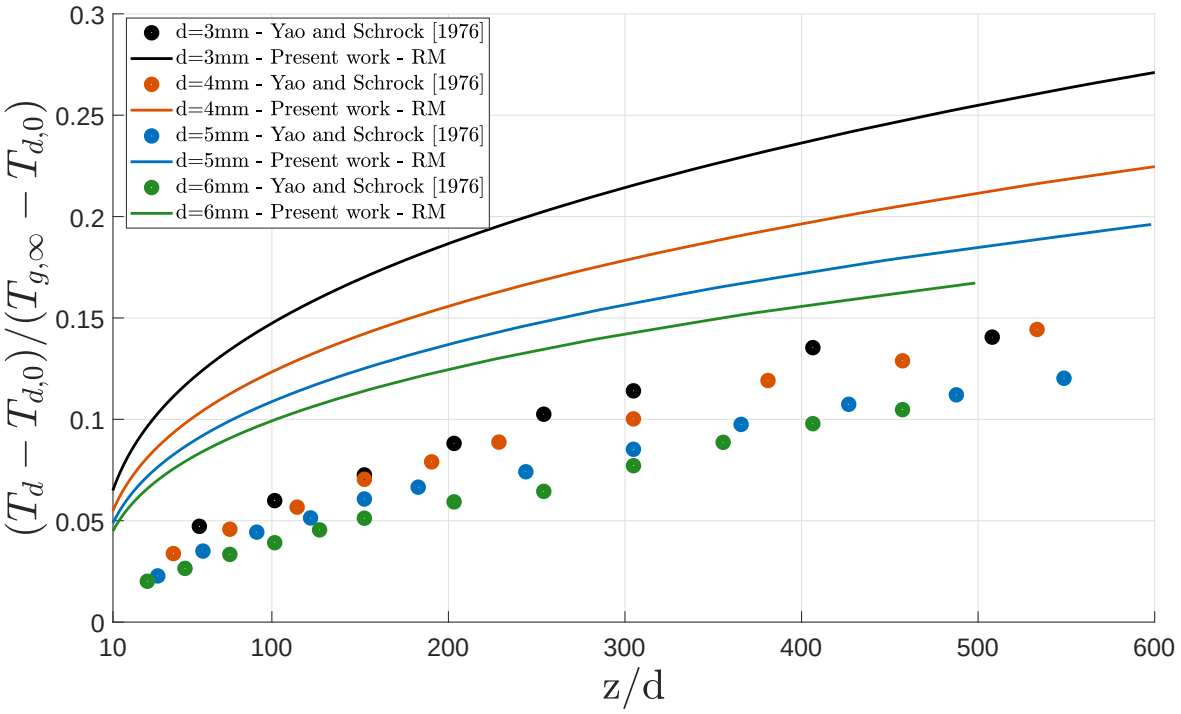

Figure 5.20: Variation on a single water droplet temperature, falling through the air, subjected to a humidity ratio of 1.00 using the Ranz-Marshall correlation, considering only the two-way coupling model results.

temperature, falling through the air, subject to a humidity ratio of 1.00 and using the Ranz-Marshall corrected formulation, it is possible to see, analogously to what happened previously in Figure 5.19, that the one-way coupling model fails on predicting the cooling phenomenon by a large margin. On the other hand, the two-way coupling model results show close agreement with the experimental data. Has it was done previously, due to the wide range of values for the dimensionless temperature, Figure 5.22 introduces a comparison between the two-way coupling methodology and the experimental data. Throughout Figure 5.22, it is possible to determine that the two-way coupling model overestimates the cooling phenomenon for all droplet diameters in the entire domain.

When comparing Figures 5.19 and 5.21, it is possible to see that the two-way coupling model is the one that resembles the numerical data more precisely, suggesting that the mutual interaction between the droplet and the surrounding environment has a predominant impact when considering saturated air.

For a droplet diameter of $3\,\mathrm{mm}$, the complete mixing model has a close agreement with the experimental data up to a falling height of 510 diameters. From that point on, the deformations and vibrations gain importance since the Ranz-Marshall corrected formulation simulates more accurately the cooling phenomenon. It is important to notice that the numerical results overestimate the phenomenon for the entire experimental domain.

Considering a diameter of $4\,\mathrm{mm}$, a similar situation occurs. Up to a falling height of 550,

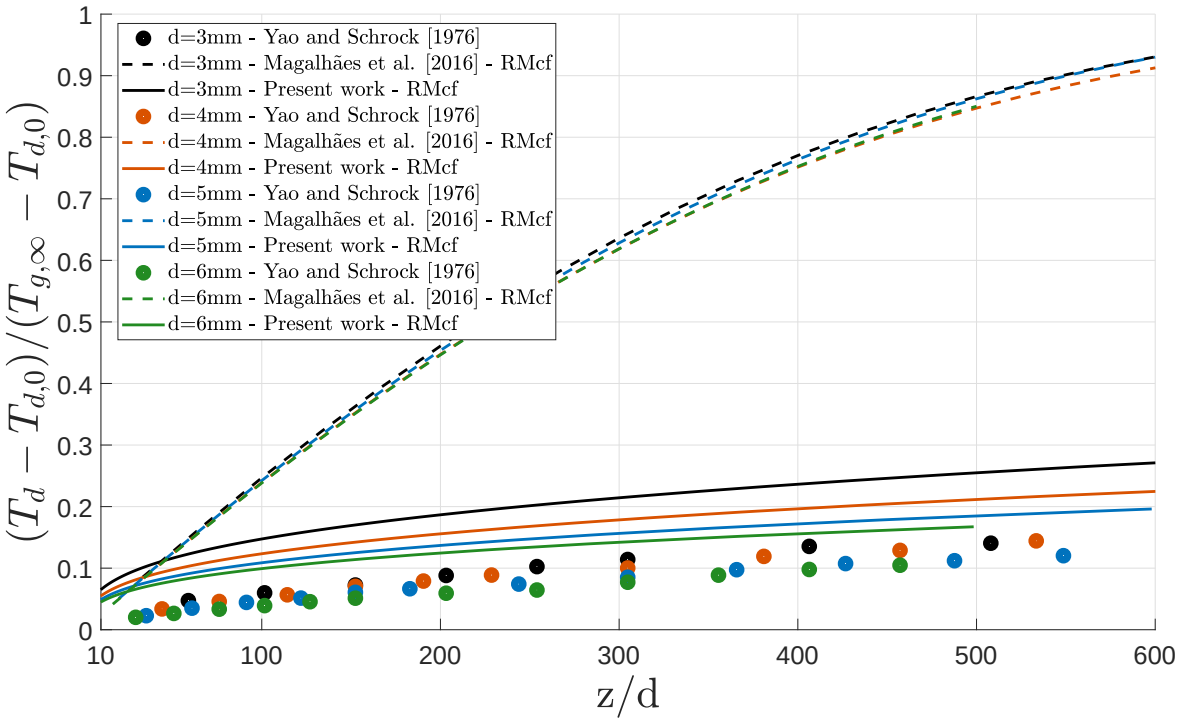

Figure 5.21: Variation on a single water droplet temperature, falling through the air, subjected to a humidity ratio of 1.00 using the Ranz-Marshall correlation with the correction factor.

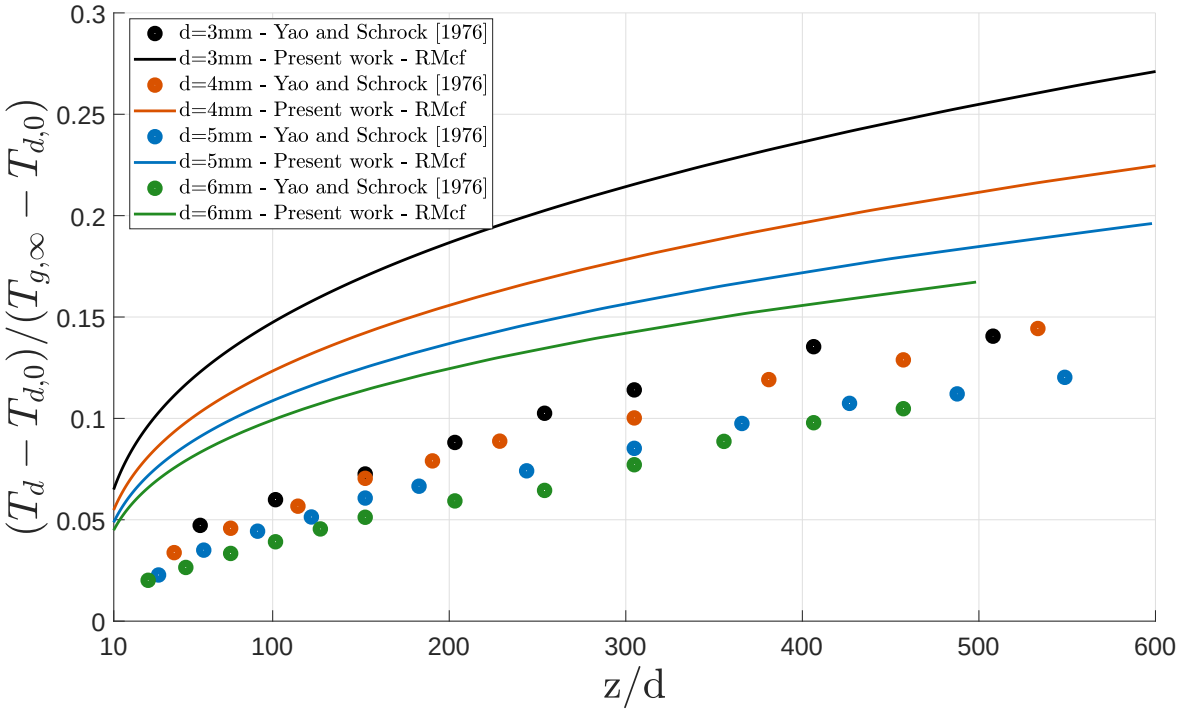

Figure 5.22: Variation on a single water droplet temperature, falling through the air, subjected to a humidity ratio of 1.00 using the Ranz-Marshall correlation with the correction factor, considering only the two-way coupling model results.

the complete mixing model assumption shows better results when compared to the mixing model assumption. However, from that point on, it becomes clear that the vibrations and deformations become predominant.

Finally, for the diameters of $5\,\mathrm{mm}$ and $6\,\mathrm{mm}$, the complete mixing model is the one that shows the best agreement with experimental data, and therefore, it is concluded that for these two diameters, the cooling phenomenon vibrations and deformations can be neglected.

5.6 Summary

To comprehend the influence of the assumptions made in Chapter 4, the results presented previously were compiled in Tables 5.11 and 5.12, representing a systematization of the numerical results that best suit the experimental data for the cooling phenomenon. The presence of a check-mark on the table cells indicates that the considered combination of models is the one that predicts the experimental data, for the entire domain, in a better way.

For instance, regarding Section 5.5, where different diameters were analyzed maintaining constant the air humidity ratio it is possible to say that as the humidity ratio increases the two-way coupling simulations tend to predict the phenomenon more accurately, independently of the Ranz-Marshall formulation that was chosen or the diameter. For higher humidity content, the mutual interaction between the droplet and the surrounding environment becomes predominant.

Additionally, for a humidity ratio of 0.29 and 1.00 the Ranz-Marshall classical formulation can resemble the experimental data for the entire domain or a big portion of the domain. This indicates that the complete mixing assumption is acceptable for these conditions meaning that vibrations and deformations do not have a considerable influence on both regimes. However, when considering an intermediate level of humidity, 0.36 and 0.56, it seems that the complete mixing model does not predict the phenomenon accurately enough, suggesting that the steady-state hypothesis is not appropriate.

These affirmations are sustained by analyzing Tables 5.11 and 5.12, which demonstrate that for a humidity ratio of 0.29, all diameters show close agreement with experimental data when resorting to the model implemented by Magalhães et al. [2016] and to the Ranz-Marshall classical formulation. Nevertheless, for a diameter of $3\,\mathrm{mm}$ and up to a falling distance of 50 diameters, the two-way coupling combined with the mixing model assumption predicts the cooling phenomenon in a better way. However, since the one-way coupling model considering a complete mixing model also shows close accuracy with experimental data for this portion of the computational domain, it is safe to say that this model predicts the experimental results in these conditions.

For a humidity ratio of 0.36, the experimental data is predicted by combining both coupling models. For this humidity content, the one-way coupling still exerts influence, especially

for a diameter of $5\,\mathrm{mm}$. Considering a diameter of $6\,\mathrm{mm}$, it is seen that in relation to the data gathered by Yao and Schrock [1976], the two-way coupling data shows better accuracy, however, the results of Magalhães et al. [2016] are also in close agreement with experimental data. The mixing model assumption is the one that works the best for this regime.

Considering a humidity ratio of 0.52 similarly to the previous regime, the experimental data can be approached by resorting to a combination of both models. However, the influence of the one-way coupling model fades away with the increase of the falling height and the two-way coupling model resembles the experimental data in a better way, especially for a diameter of $6\,\mathrm{mm}$. Considering the formulations used to obtain the convective heat transfer coefficients, with exception for a diameter of $4\,\mathrm{mm}$ and only for a falling height higher than 400 diameters, is the mixing model assumption that has the closest agreement with experimental data.

Finally, for the highest humidity ratio studied, 1.00, the two-way coupling model is the one that resembles the experimental data, for the entire experimental domain, in a better way. The complete mixing assumption is the one that best suits the experimental data for the entire domain, as it happens when considering a droplet diameter of $5\,\mathrm{mm}$ and $6\,\mathrm{mm}$ or a considerable portion of the domain, as it occurs for a droplet diameter of $3\,\mathrm{mm}$ and $4\,\mathrm{mm}$.

The same conclusions are drawn when analyzing different air humidity ratios maintaining constant the droplet diameters. As seen previously, this comparison was made in Section 5.4.

Table 5.11: Systematization of the numerical results that best suit the experimental data gathered by Yao and Schrock [1976], comparing the Ranz-Marshall formulations with the droplet diameters and the coupling models with the air humidity ratios.

		3 mm		4 mm		5 mm		6 mm	
		RM	RMcf	RM	RMcf	RM	RMcf	RM	RMcf
0.29	OW	$z > 80d$		-	-	✓		-	-
	TW		$z < 80d$	-	-			-	-
0.36	OW		$z > 310d$		$z > 230d$		$z > 190d$		
	TW		$z < 310d$		$z < 230d$		$z < 190d$		✓
0.52	OW	-	-		$z < 100d$	-	-		$z < 70d$
	TW	-	-	$z > 400d$	$z > 100d$ $z < 400d$	-	-		$z > 70d$
1.00	OW								
	TW	$z < 510d$	$z > 510d$	$z < 550d$	$z > 550d$	✓		✓	

Table 5.12: Systematization of the numerical results that best suit the experimental data gathered by Yao and Schrock [1976], comparing the coupling models with the diameters and the Ranz-Marshall formulations with the air humidity ratios.

		3 mm		4 mm		5 mm		6 mm	
		OW	TW	OW	TW	OW	TW	OW	TW
0.29	RM	$z > 80d$		-	-	✓		-	-
	RMcf		$z < 80d$	-	-			-	-
0.36	RM								
	RMcf	$z > 310d$	$z < 310d$	$z > 230d$	$z < 230d$	$z > 190d$	$z < 190d$		✓
0.52	RM	-	-		$z > 400d$	-	-		
	RMcf	-	-	$z < 100d$	$z > 100d$ $z < 400d$	-	-	$z < 70d$	$z > 70d$
1.00	RM		$z < 510d$		$z < 550d$		✓		✓
	RMcf		$z > 510d$		$z > 550d$				

Chapter 6

Four-stage freezing modeling analysis

To understand how the results presented in Chapter 5 can be integrated on a full-scale four-stage freezing model, it is important to consider that they only correspond to a segment of the first stage of this model. Therefore, it is essential to contextualize these results and present the overall freezing process. In this way, after performing the studies presented in Chapter 5, where the cooling of water droplets resorting to two distinct coupling methodologies is analyzed and subsequently compared to experimental data gathered by Yao and Schrock [1976], a complete analytical study on a full-scale four-stage freezing model was performed and further compared with experimental data collected by Hindmarsh et al. [2003]. These results are presented in Section 6.1. Section 6.2 sums up the content presented.

6.1 Four-stage freezing results

The study performed by Hindmarsh et al. [2003] presents a simple experimental and numerical method to study the temperature transition of freezing water droplets. To experimentally obtain the data for the temperature profile of a supercooling water droplet, the particle was suspended on a thermocouple in a cold air stream while the temperature at the thermocouple tip was being recorded.

Therefore, the data gathered by Hindmarsh et al. [2003] suits the purpose of validating an analytical model considering a full four-stage freezing process, according to what was presented in Chapter 4. The initial conditions used match the ones simulated experimentally by Hindmarsh et al. [2003]. Table 6.1 presents those initial conditions performed on the experimental analysis of the temperature transition of a suspended freezing water droplet.

Figure 6.1 shows the comparison between the experimental analysis of the temperature transition for a suspended freezing water droplet and the analytical model used to predict that phenomenon, resorting to the initial conditions that were summarized in Table 6.1. Moreover, Figure 6.1 also presents the solid mass fraction line representing the fraction between the liquid mass and the solid mass. Therefore, for a value of 1, the droplet is completely solidified and for a value of 0 is completely liquid. To calculate the convective heat and mass transfer coefficients was used the Ranz-Marshall correlation.

Figure 6.1 allows to conclude that, generically, this model can predict the temperature

Table 6.1: Initial conditions from the experimental analysis of the temperature transition of a suspended freezing water droplet performed by Hindmarsh et al. [2003].

Property	Value
Diameter [mm]	1.56
Initial droplet temperature [K]	280.35
Environment temperature [K]	254.15
Nucleation temperature [K]	254.75
Freezing temperature [K]	273.15
Air velocity [$\mathrm{m\,s^{-1}}$]	0.42
Prandtl number [−]	0.72

profile of a freezing water droplet since the analytical predictions show close agreement with the experimental data gathered by Hindmarsh et al. [2003]. On the first stage, also called supercooling stage, the computational model precisely replicates the experimental data overlapping it during this phase. However, the analytical predictions state that the droplet nucleation temperature, which corresponds to the finishing of the first stage, is met at $29.5\,\mathrm{s}$ yet, when considering the experimental data, this stage only finishes $28\,\mathrm{s}$ after the initial moment.

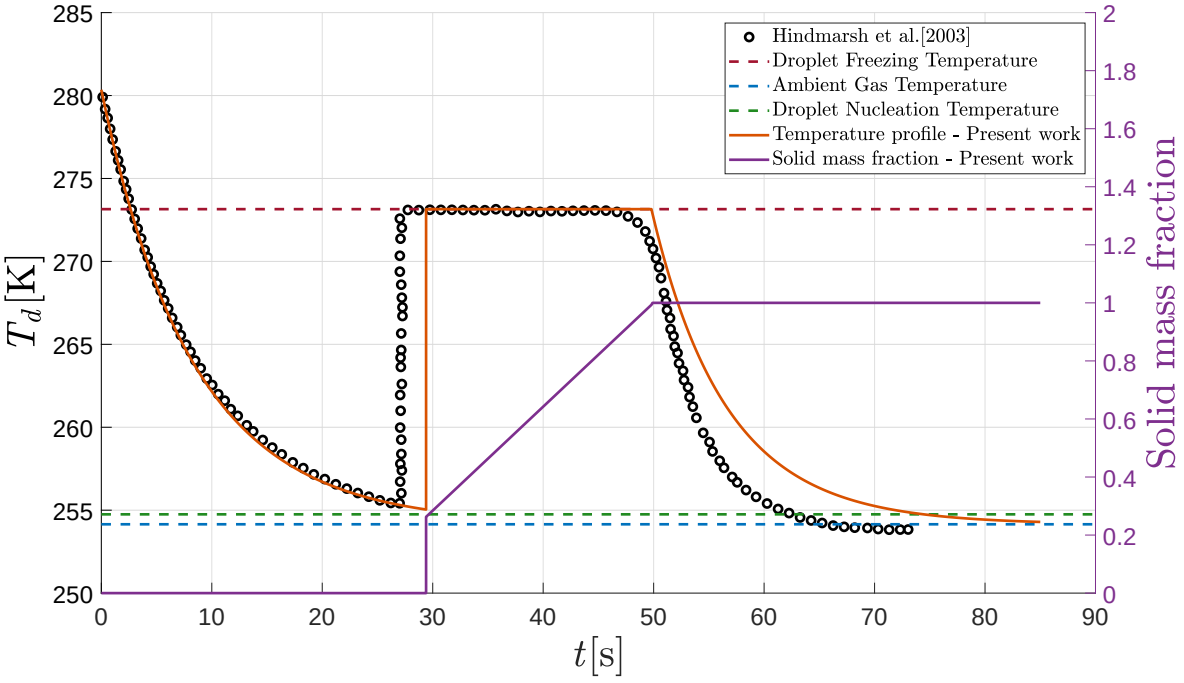

Figure 6.1: Comparison between the experimental analysis of the temperature transition for a suspended freezing water droplet, performed by Hindmarsh et al. [2003], and the analytical predictions when considering a four-stage physical model.

At nucleation, recalescence occurs, the latent heat released from crystallization raises the droplet temperature to the equilibrium freezing temperature, the phase-change temperature. As seen in Chapter 4, the recalescence stage is assumed to occur instantaneously, and the instant used, in which this stage occurs, is the last one from the supercooling stage. This

assumption is compliant with the data gathered by Hindmarsh et al. [2003]. However, since the first phase had a delay of $1.5\,\mathrm{s}$, in relation to the experimental data, the recalescence is shifted to the right that amount of time, as it is seen in Figure 6.1.

The third stage, or solidification stage, is characterized by the droplet temperature remaining at the equilibrium freezing temperature until the particle is completely frozen. The numerical predictions accurately simulate the data gathered by Hindmarsh et al. [2003] although, due to the delay obtained computationally on the first stage, and widespread to the second stage, the results for this phase are displaced when compared with the experimental ones. The experimental results predict that the solidification stage finishes $48.5\,\mathrm{s}$ after the beginning of the experiment. The analytical results indicate that the third stage finishes $49.8\,\mathrm{s}$ after the initial moment. Considering those facts, the delay inherited from the first phase, which was $1.5\,\mathrm{s}$, is increased by $0.3\,\mathrm{s}$ in the third phase.

Lastly, considering the solid stage, the analytical model does not precisely replicate the experimental data. However, it still shows close agreement with the data gathered by Hindmarsh et al. [2003]. The experimental data indicate that the freezing phenomenon ends $74.6\,\mathrm{s}$ after the initial moment. In contrast, the analytical model suggests that the total freezing time is $85\,\mathrm{s}$. This difference is justified, eventually, due to the delay accumulated in the last three phases. Additionally, the transition between the third and fourth phases is not so drastic, experimentally, as it is suggested analytically. This is a consequence of the physical and mathematical models stated in Chapter 4 that fail to predict the transition.

6.2 Summary

The analytical results predict a total freezing time for a suspended water droplet subjected to the airflow, of $85\,\mathrm{s}$. On the other hand, the experimental data gathered by Hindmarsh et al. [2003] demonstrated that, for the initial conditions shown in Table 6.1, this time was of $74.6\,\mathrm{s}$. As introduced previously, these differences are attributed mainly to the accumulation of time delays between all distinct phases, especially between the third and fourth stages. Two main reasons are suggested to explain the differences between the experimental and computational data:

- The heat flux through the thermocouple was not considered on the actual simulations what possibly contributed to differences between the predictions and the experimental data;

- The physical interpolations used on numerical predictions can induce errors. These errors are then carried from the first phase to the subsequent ones.

Nevertheless, from the available data and the analysis that was made, it is possible to conclude that the current model is capable of predicting the supercooling freezing of water droplets, however, some adjustments are required.

Chapter 7

Conclusions

This chapter presents the conclusions of this work and is divided into two distinct sections. Section 7.1 shows the final remarks of this study and summarizes what was achieved. Section 7.2 gives an insight about the future work considering the remarks which were presented and the state-of-the-art.

7.1 Final remarks

This work aimed to study the cooling of water droplets, with different diameters and air humidity ratios, through the readaptation of a pre-existent in-house computational tool, for the purpose. After understanding the capabilities of the existing tool, the mathematical models, which accounted for the evaporation of liquid-fuel droplets, were changed. For the physics of liquid water droplets under a cooling process, a simple heat balance model was used for solving the internal energy balance of the droplet.

As a consequence of those changes, a two-way coupling computational tool that successfully evaluates the temperature profile of a cooling water droplet in a humid air environment was obtained. To guarantee the ability of this computational tool on predicting the cooling phenomenon, the numerical results of this study were contextualized with experimental data available in the literature. Furthermore, to evaluate the effect of taking into account the mutual interaction between droplets and the surrounding environment, considering distinct droplet diameters and air humidity ratios, the results were also compared with a one-way coupling numerical study.

It was concluded that predictions resorting to the two-way coupling model are in close proximity with experimental data, for any diameter, when considering high humidity ratios. However, these predictions failed to replicate the data obtained experimentally for lower humidity ratios, where the one-way coupling had greater proximity. Therefore, it is suitable to interpret that, for high humidity content, the mutual interaction between the droplet and the surrounding environment becomes predominant and needs to be accounted for. When considering low humidity content, this mutual interaction can be neglected, since the one-way coupling resembles the experimental data in a better way.

Moreover, it was possible to conclude that the complete mixing model is an acceptable assumption when considering low or high humidity ratios (0.29 and 1.00) since the results obtained when resorting to the Ranz-Marshall classical formulation tend to predict the

cooling phenomenon, for any diameter, more accurately. This fact indicates a steady-state regime for these conditions. On the other hand, when considering an intermediate level of humidity (0.36 and 0.56), it seemed that the complete mixing model could not predict the phenomenon accurately enough, since the Ranz-Marshall corrected formulation simulated the phenomenon more accurately, suggesting that the mixing model assumption is acceptable for these conditions.

All in all, it can be concluded that the droplet vibrations and deformations have to be accounted for when considering intermediate levels of humidity and can be neglected for high and low humidity content of the air. The mutual interaction between the droplet and the surrounding environment can be neglected when considering low humidity ratios and has to be considered for high humidity ratios.

Additionally, to context the results previously presented, a full-scale four-stage analytical model was implemented and compared with experimental data available in the literature. It was concluded that this model was capable of predicting the supercooling freezing of water droplets considering specific conditions. However, some adjustments are required since the total freezing time is overestimated relatively to what was seen experimentally, indicating that the analytical model underestimates the cooling phenomenon. Furthermore, it was seen that the transition between the third and fourth stages of the supercooling process was not accurately represented in the analytical study, suggesting a non-linearity on the crystallization kinetics.

7.2 Future work

The natural step after simulating the cooling of water droplets, using a readapted computational tool, is to implement a numerical full-scale supercooling process, as was shown in the analytical model developed. However, the conclusions of this work revealed certain aspects that require attention.

This work assumes a complete mixing model, and, consequently, the droplets are considered as material points that have the same temperature in their entire volume. However, when comparing the two correlations used, it was possible to see that in some regimes that assumption does not predict the cooling phenomenon accurately. Additionally, it was seen that the mutual interaction between the particles and the surrounding environment also needs to be considered in certain regimes. This strongly indicates that the internal heat gradients inside the droplets play a fundamental role and, for that reason, it is recommendable, when considering future works, to verify this situation by analyzing the Biot number. As a consequence of considering a mixing model hypothesis, it is necessary to approach the crystallization kinetics phenomenon differently since the crystal growth rate, the dynamic propagation of phase front, and the interface velocity, which were not accounted for in the presented models, need to be considered.

Concerning the analytical four-stage model, accounting for the heat flux through the thermocouple would ensure that this term does not have significant importance on the final calculations and, for that reason, can be neglected. A validation of this model resorting to others experimental and numerical studies available in the literature that consider other droplet fluid or surrounding environment would empower the conclusions of this work and expand our knowledge about the phenomenon. A detailed study about the influence of the recalescence stage, considering a noninstantaneous phase (dendritic growth) and mathematically modeling it, should be considered. Additionally, in this work, was assumed that the nucleation is homogeneous and, for that reason, it occurs spontaneously. When considering future works, a heterogeneous approach, that accounts for the presence of impurities and external contacts would benefit the overall accuracy of the model, especially in the second stage. This work also revealed that the transition between the third and fourth stages of the process needs to be studied and modeled differently since it does not represent the experimental data.

Knowing that the final aim is to obtain a computational tool capable of simulating different icing formation regimes, for distinct lifting surfaces, and evaluate their impact on the aerodynamic performance of that surface, it can be concluded that only a small fraction of this objective was achieved. Therefore, to continue this work, it is now required to develop a full-scale numerical freezing model and add a collision and accretion model to predict how ice affects the aerodynamic performance of a lifting surface.

Bibliography

S. Akhtar, M. Xu, and A. P. Sasmito. Development and validation of a semi-analytical framework for droplet freezing with heterogeneous nucleation and non-linear interface kinetics. *International Journal of Heat and Mass Transfer*, page 120734, 2020. doi: https://doi.org/10.1016/j.ijheatmasstransfer.2020.120734. 0017-9310. 21

V. Alexiades and A. D. Solomon. *Mathematical Modeling of Melting and Freezing Processes*. Hemisphere Publishing Corporation, 1993. ISBN 1-56032-125-3. xiii, 7, 8, 9, 20, 46

J. Barata and A. Silva. Numerical study of impinging droplets through a crossflow. In *40th Thermophysics Conference*. AIAA, 2008. doi: https://arc.aiaa.org/doi/abs/10.2514/6.2008-3923. 4

J. Barata, A. Cometti, and A. Silva. Numerical simulation of an array of droplets through a crossflow. In *40th AIAA Aerospace Sciences Meeting and Exhibit*. AIAA, 2002. doi: https://arc.aiaa.org/doi/abs/10.2514/6.2002-872. 4

H. Beaugendre, F. Morency, and W. G. Habashi. FENSAP-ICE's Three-Dimensional In-Flight Ice Accretion Module: ICE3D. *Journal of Aircraft*, 40(2):239–247, 2003. doi: https://doi.org/10.2514/2.3113. 24

C. W. Beckett, W. S. Benedict, and J. Hilsenrath. *Tables of thermal properties of gases, comprising tables of thermodynamic and transport properties of air, argon, carbon dioxide, carbon monoxide, hydrogen, nitrogen, oxygen and steam*. National Bureau of Standards. Washington, DC, 1955. 109

T. L. Bergman, A. S. Lavine, F. P. Incropera, and D. P. Dewitt. *Fundamentals of Heat and Mass Transfer*. John Wiley & Sons, Incorporated, seventh edition, 2011. ISBN 978-1-118-13725-3. 58

D. R. Bilodeau, W. G. Habashi, M. Fossati, and G. S. Baruzzi. Eulerian modeling of supercooled large droplet splashing and bouncing. *Journal of Aircraft*, 52(5):1611–1624, 2015. doi: https://doi.org/10.2514/1.C033023. 18

J. Blake, D. Thompson, D. Raps, and T. Strobl. Simulating the freezing of supercooled water droplets impacting a cooled substrate. *AIAA Journal*, 53(7):1725–1739, 2015. doi: https://doi.org/10.2514/1.J053391. 18

D. T. Bowden. Effect of pneumatic de-icers and ice formations on aerodynamic characteristics of an airfoil. Tech Report 3564, NACA - National Advisory Committee for Aeronautics, February 1956. 17

M. Bragg, T. Basar, W. Perkins, M. Selig, P. Voulgaris, J. Melody, and N. Sarter. Smart icing systems for aircraft icing safety. In *40th AIAA Aerospace Sciences Meeting and Exhibit*. AIAA, 2002. doi: https://doi.org/10.2514/6.2002-813. xiii, 15

T. Brahimi, P. Tran, and I. Paraschivoiu. Numerical Simulation and Thermodynamic Analysis of Ice Accretion on Aircraft Wings. Tech Report C.D.T C159, Centre de Development Technologique de Ecole Polytechnique de Montreal, Montréal, QC, Canada, May 1994. 24

M. Brunetti, S. Chatterton, N. Toscani, M. Mauri, M. S. Carmeli, and F. Castelli-Dezza. Wireless power transfer withtemperature monitoring interface forhelicopter rotor blade ice protection. In *AIAA Propulsion and Energy 2020 Forum*. AIAA, 2020. doi: https://doi.org/10.2514/6.2020-3569. 16

F. Caliskan and C. Hajiyev. A review of in-flight detection and identification of aircraft icing and reconfigurable control. *Progress in Aerospace Sciences*, 60:12–34, 2013. doi: https://doi.org/10.1016/j.paerosci.2012.11.001. 0376-0421. 2

Y. Cao and K. Chen. Helicopter icing. *The Aeronautical Journal*, 114(1152):83–90, 2010. doi: https://doi.org/10.1017/S0001924000003559. 14, 22

Y. Cao, Q. Zhang, and J. Sheridan. Numerical simulation of rime ice accretions on an aerofoil using an Eulerian method. *The Aeronautical Journal*, 112(1131):243–249, 2008. doi: https://doi.org/10.1017/S0001924000002189. 18

Y. Cao, J. Huang, Z. Xu, and J. Yin. Insight into rime ice accretion on an aircraft wing and corresponding effects on aerodynamic performance. *The Aeronautical Journal*, 120 (1229):1101–1122, 2016. doi: https://doi.org/10.1017/aer.2016.49. 18

Y. Cao, W. Tan, and Z. Wu. Aircraft icing: An ongoing threat to aviation safety. *Aerospace Science and Technology*, 75:353–385, 2018. doi: https://doi.org/10.1016/j.ast.2017.12.028. 1270-9638. 4, 10, 11, 12, 23

T. Carroll and Wm. H. McAvoy. *The formation of ice upon exposed parts of an airplane in flight*. NACA - National Advisory Committee for Aeronautics, July 1928. 16

T. Carroll and Wm. H. McAvoy. *The formation of ice upon airplanes in flight*. NACA - National Advisory Committee for Aeronautics, August 1929. 16

K. H. Chen and G. J. Trezek. The effect of heat transfer coefficient, local wet bulb temperature and droplet size distribution function on the thermal performance of sprays. *Journal of Heat Transfer*, 99(3):381–385, 1977. doi: https://doi.org/10.1115/1.3450706. 0022-1481. 20

C. T. Crowe, J. D. Schwarzkopf, M. Sommerfeld, and Y.Tsuji. *Multiphase Flows with Droplets and Particles*. CRC Press, second edition, 2011. ISBN 978-1439840504. doi: https://doi.org/10.1201/b11103. 34

D. R. Dickinson and W. R. Marshall Jr. The rates of evaporation of sprays. *American Institute of Chemical Engineers Journal*, 14(4):541–552, 1968. doi: https://doi.org/10.1002/aic.690140404. 20

G. L. Dillingham. *GAO-10-441T - Aviation safety - Preliminary information on aircraft icing and winter operations*. GAO - United States Government Accountability Office, February 2010. 3

E. R. G. Eckert and R. M. Drake. *Heat and mass transfer*. McGraw-Hill Inc., 1959. ISBN 978-0-07-018924-9. 55

S. Elghobashi. On predicting particle-laden turbulent flows. *Applied Scientific Research*, 52 (4):309–329, 1994. doi: https://doi.org/10.1007/BF00936835. 1573-1987. 20

M. Epstein and H. K. Fauske. Kinetic and heat transfer-controlled solidification of highly supercooled droplets. *International Journal of Heat and Mass Transfer*, 36(12):2987–2995, 1993. doi: https://doi.org/10.1016/0017-9310(93)90028-5. 0017-9310. 20, 47

D. G. Fahrenheit. Experimenta & observationes de congelatione aquæ in vacuo factæ. *Philosophical Transactions of the Royal Society of London*, 33(382):78–84, 1724. doi: https://royalsocietypublishing.org/doi/pdf/10.1098/rstl.1724.0016. 19

O. Fakorede, Z. Feger, H. Ibrahim, A. Ilinca, J. Perron, and C. Masson. Ice protection systems for wind turbines in cold climate: characteristics, comparisons and analysis. *Renewable and Sustainable Energy Reviews*, 65:662–675, 2016. doi: https://doi.org/10.1016/j.rser.2016.06.080. 1364-0321. 1

G. Fortin, J.-L. Laforte, and A. Beisswenger. Prediction of Ice Shapes on NACA0012 2D Airfoil. In *FAA In-flight Icing / Ground De-icing International Conference & Exhibition*. SAE International, 2003. doi: https://doi.org/10.4271/2003-01-2154. 24

G. Fortin, J.-L. Laforte, and A. Ilinca. Heat and mass transfer during ice accretion on aircraft wings with an improved roughness model. *International Journal of Thermal Sciences*, 45 (6):595–606, 2006. doi: https://doi.org/10.1016/j.ijthermalsci.2005.07.006. 1290-0729. 18

R. W. Gent. TRAJICE2 — A combined water droplet trajectory and ice accretion prediction program for aerofoils. Tech Report 90054, RAE - Royal Aircraft Establishment, 1990. 24

G. Gouesbet and A. Berlemont. Eulerian and Lagrangian approaches for predicting the behaviour of discrete particles in turbulent flows. *Progress in Energy and Combustion Science*, 25(2):133–159, 1999. doi: https://doi.org/10.1016/S0360-1285(98)00018-5. 0360-1285. xvii, 20, 26, 31, 38

S. D. Green. A study of U.S. inflight icing accidents and incidents, 1978 to 2002. In *44th AIAA Aerospace Sciences Meeting and Exhibit*. AIAA, 2006. doi: https://doi.org/10.2514/6.2006-82. 3

S. D. Green. *DOT/FAA/TC-14/44 - The icemaster database and an analysis of aircraft aerodynamic icing accidents and incidents*. Federal Aviation Administration William J. Hughes Technical Center Aviation Research Division, June 2015. xiii, 3

V. H. Grey and U. H. von Glahn. Effect of ice and frost formations on drag of NACA 65(1)-212 airfoil for various modes of thermal ice protection. Tech Report 2962, NACA - National Advisory Committee for Aeronautics, June 1953. 17

S. C. Gupta. *The Classical Stefan Problem - Basic Concepts, Modelling and Analysis with Quasi-Analytical Solutions and Methods*. Elsevier, second edition, 2017. ISBN 978-0-444-63581-5. doi: https://doi.org/10.1016/C2017-0-02306-6. 7, 8, 21

O. Gurevich, S. Smetanin, and M. Trifonov. Analysis of the impact of control methods on turbofan performance in ice crystal conditions. In *AIAA Propulsion and Energy 2020 Forum*. AIAA, 2020. doi: https://doi.org/10.2514/6.2020-3682. 12, 19

R. J. Hansman, K. S. Breuer, D. Hazan, A. Reehorst, and M. Vargas. Close-up analysis of aircraft ice accretion. In *31st Aerospace Sciences Meeting and Exhibit*. AIAA, 1993. doi: https://doi.org/10.2514/6.1993-29. 18

J. K. Hardy. Protection of aircraft against ice. *The Journal of the Royal Aeronautical Society*, 51(435):271–305, 1947. doi: https://doi.org/10.1017/S0368393100108375. 17

T. Hedde and D. Guffond. ONERA three-dimensional icing model. *AIAA Journal*, 33(6): 1038–1045, 1995. doi: https://doi.org/10.2514/3.12795. 24

J. P. Hindmarsh, A. B. Russell, and X. D. Chen. Experimental and numerical analysis of the temperature transition of a suspended freezing water droplet. *International Journal of Heat and Mass Transfer*, 46(7):1199–1213, 2003. doi: https://doi.org/10.1016/S0017-9310(02)00399-X. 0017-9310. xv, xvii, 21, 47, 58, 91, 92, 93, 109

J. P. Hindmarsh, A. B. Russell, and X. D. Chen. Fundamentals of the spray freezing of foods—microstructure of frozen droplets. *Journal of Food Engineering*, 78(1):136–150, 2007. doi: https://doi.org/10.1016/j.jfoodeng.2005.09.011. 0260-8774. 21

C. Hirsch. *Numerical Computation of Internal and External Flows - The Fundamentals of Computational Fluid Dynamics*. Butterworth-Heinemann, second edition, 2007. ISBN 978-0-7506-6594-0. doi: https://doi.org/10.1016/B978-0-7506-6594-0.X5037-1. 40

K. Hossain, V. Sharma, M. Bragg, and P. Voulgaris. Envelope protection and control adaptation in icing encounters. In *41st Aerospace Sciences Meeting and Exhibit*. AIAA, 2003. doi: https://doi.org/10.2514/6.2003-25. 15, 18

X. Huang, N. Tepylo, V. Pommier-Budinger, M. Budinger, E. Bonaccurso, P. Villedieu, and L. Bennani. A survey of icephobic coatings and their potential use in a hybrid coating/active ice protection system for aerospace applications. *Progress in Aerospace Sciences*, 105:74–97, 2019. doi: https://doi.org/10.1016/j.paerosci.2019.01.002. 0376-0421. 12, 16

R. R. Hughes and E. R. Gilliland. The mechanics of drops. *Chemical Engineering Progress*, 48:497–504, 1952. 19

Z. A. Janjua, B. Turnbull, S. Hibberd, and K.-S. Choi. Mixed ice accretion on aircraft wings. *Physics of Fluids*, 30(2):027101, 2018. doi: https://doi.org/10.1063/1.5007301. 21

S. M. Jones, M. S. Reveley, J. K. Evans, and F. A. Barrientos. *NASA/TM-2008–215107 - Subsonic aircraft safety icing study*. NASA - National Aeronautics and Space Administration, 2008. 3

E. E. Khalil and M. Sobhi. CFD simulation of thermal and energy performance for a display cabinet refrigerator containing a phase change material (PCM). In *AIAA Propulsion and Energy 2020 Forum*. AIAA, 2020. doi: https://doi.org/10.2514/6.2020-3946. 1

R. J. Kind, M. G. Potapczuk, A. Feo, C. Golia, and A. D. Shah. Experimental and computational simulation of in-flight icing phenomena. *Progress in Aerospace Sciences*, 34(5):257–345, 1998. doi: https://doi.org/10.1016/S0376-0421(98)80001-8. 0376-0421. 18, 23

E. J. Langham and B. J. Mason. The heterogeneous and homogeneous nucleation of supercooled water. *Proceedings of the Royal Society of London. Series A. Mathematical and Physical Sciences*, 247(1251):493–504, 1958. doi: 10.1098/rspa.1958.0207. 20

B. E. Launder and D. B. Spalding. The numerical computation of turbulent flows. *Computer Methods in Applied Mechanics and Engineering*, 3(2):269–289, 1974. doi: https://doi.org/10.1016/0045-7825(74)90029-2. 0045-7825. xvii, 29, 31

A. H. Lefebvre and V. G. McDonell. *Atomization and Sprays*. CRC Press, second edition, April 2017. ISBN 978-1-49873-625-1. doi: https://doi.org/10.1201/9781315120911. 54

B. P. Leonard. A stable and accurate convective modelling procedure based on quadratic upstream interpolation. *Computer Methods in Applied Mechanics and Engineering*, 19 (1):59–98, 1979. doi: https://doi.org/10.1016/0045-7825(79)90034-3. 0045-7825. 40

P. J. Linstrom and W. G. Mallard, editors. *NIST Chemistry WebBook, NIST Standard Reference Database Number 69, checked on 8th March 2021*. National Institute of Standards and Technology, Gaithersburg MD, 20899. 109

T. Liu, K. Qu, J. Cai, and S. Pan. A three-dimensional aircraft ice accretion model based on the numerical solution of the unsteady Stefan problem. *Aerospace Science and Technology*, 93:105328, 2019. doi: https://doi.org/10.1016/j.ast.2019.105328. 1270-9638. 18

E. P. Lozowski, J. R. Stallabrass, and P. F. Hearty. The icing of an unheated, nonrotating cylinder. Part I: A simulation model. *Journal of Applied Meteorology and Climatology*, 22(12):2053–2062, 1983a. doi: 10.1175/1520-0450(1983)022<2053:TIOAUN>2.0.CO;2. 17

E. P. Lozowski, J. R. Stallabrass, and P. F. Hearty. The icing of an unheated, nonrotating cylinder. Part II. Icing wind tunnel experiments. *Journal of Applied Meteorology and Climatology*, 22(12):2063–2074, 1983b. doi: 10.1175/1520-0450(1983)022<2063:tioaun>2.0.co;2. 17

C. D. MacArthur. Numerical simulation of airfoil ice accretion. In *21st Aerospace Sciences Meeting*. AIAA, 1983. doi: https://doi.org/10.2514/6.1983-112. 17

L. B. Magalhães, J. M. Barata, and A. R. Silva. Numerical study of freezing droplets. In *CEM 2016 - Mechanical Engineering Conference*, 2016. 59, 60, 61, 63, 64, 66, 68, 69, 70, 71, 72, 73, 74, 75, 76, 78, 79, 82, 86, 87

B. J. Mason. The supercooling and nucleation of water. *Advances in Physics*, 7(26):221–234, 1958. doi: https://doi.org/10.1080/00018735800101237. 20

F. J. McQuillan, J. R. Culham, and M. M. Yovanovich. Properties of dry air at one atmosphere. *Microelectronics Heat Transfer Lab - University of Waterloo*, 1984. 109

Z. Meng and P. Zhang. Dynamic propagation of ice-water phase front in a supercooled water droplet. *International Journal of Heat and Mass Transfer*, 152:119468, 2020. doi: https://doi.org/10.1016/j.ijheatmasstransfer.2020.119468. 0017-9310. xiii, 1, 21, 48

B. L. Messinger. Equilibrium temperature of an unheated icing surface as a function of air speed. *Journal of the Aeronautical Sciences*, 20(1):29–42, 1953. doi: https://doi.org/10.2514/8.2520. 19

G. Mingione, V. Brandi, B. Esposito, G. Mingione, V. Brandi, and B. Esposito. Ice accretion prediction on multi-element airfoils. In *35th Aerospace Sciences Meeting and Exhibit*. AIAA, 1997. doi: 10.2514/6.1997-177. 24

O. Miyawaki, T. Abe, and T. Yano. A numerical model to describe freezing of foods when supercooling occurs. *Journal of Food Engineering*, 9(2):143–151, 1989. doi: https://doi.org/10.1016/0260-8774(89)90011-3. 0260-8774. 20, 47

B. J. Murray, S. L. Broadley, and G. J. Morris. Supercooling of water droplets in jet aviation fuel. *Fuel*, 90(1):433–435, 2011. doi: https://doi.org/10.1016/j.fuel.2010.08.018. 0016-2361. 1

T. G. Myers, M. G. Hennessy, and M. Calvo-Schwarzwälder. The Stefan problem with variable thermophysical properties and phase change temperature. *International Journal of Heat and Mass Transfer*, 149:118975, 2020. doi: https://doi.org/10.1016/j.ijheatmasstransfer.2019.118975. 0017-9310. 21

H. Noth and W. Polte. The formation of ice on airplanes. Tech Report 786, NACA - National Advisory Committee for Aeronautics, February 1936. 16

NTSB. Factual report aviation - FTW95FA129. Tech Report FTW95FA129, National Transportation Safety Board, November 1995. 18

NTSB. In-flight icing encounter and loss of control simmons airlines, d.b.a American Eagle Flight 4184 Avions de Transport Regional (ATR) Model 72-212, N401AM Roselawn, Indiana October 31, 1994. Tech Report DCA95MA001, National Transportation Safety Board, July 1996. 18

NTSB. In-flight icing encounter and uncontrolled collision with terrain Comair Flight 3272 Embraer EMB-120RT, N265 Camonroe, Michigan January 9, 1997. Tech Report DCA97MA017, National Transportation Safety Board, November 1998. 18

NTSB. Factual report aviation - DCA01MA031. Tech Report DCA01MA031, National Transportation Safety Board, December 2002. 18

W. Olsen and E. Walker. Experimental evidence for modifying the current physical model for ice accretion on aircraft surfaces. Technical Report 87184, National Aeronautics and Space Administration, 1986. 17

O. Parent and A. Ilinca. Anti-icing and de-icing techniques for wind turbines: Critical review. *Cold Regions Science and Technology*, 65(1):88–96, 2011. doi: https://doi.org/10.1016/j.coldregions.2010.01.005. 0165-232X. 10

S. V. Patankar and D. B. Spalding. A calculation procedure for heat, mass and momentum transfer in three-dimensional parabolic flows. *International Journal of Heat and Mass Transfer*, 15(10):1787–1806, 1972. doi: https://doi.org/10.1016/0017-9310(72)90054-3. 0017-9310. 41

W. E. Ranz and W. R. Marshall. Evaporation from drops: Part 1. *Chemical Engineering Progress*, 48(3):141–146, 1952a. 0360-7275. 19, 20, 53

W. E. Ranz and W. R. Marshall. Evaporation from drops: Part 2. *Chemical Engineering Progress*, 48(4):173–180, 1952b. 0360-7275. 19, 20, 53

C. Rodrigues, J. Barata, and A. Silva. Modeling of droplet deformation and breakup. *Journal of Propulsion and Power*, 32(3):698–706, 2016. doi: https://doi.org/10.2514/1.B35819. 5

C. Rodrigues, J. Barata, and A. Silva. Modeling of evaporating sprays impinging onto solid surfaces. *Journal of Thermophysics and Heat Transfer*, 31(1):109–119, 2017. doi: https://doi.org/10.2514/1.T4733. 5

G. A. Ruff and B. M. Berkowitz. Users Manual for the NASA Lewis Ice Accretion Prediction Code (LEWICE). Tech Report 185129, NASA - National Aeronautics and Space Administration, May 1990. 24

E. M. Samuelsen and R. G. Graversen. Weather situation during observed ship-icing events off the coast of Northern Norway and the Svalbard archipelago. *Weather and Climate Extremes*, 24:100200, 2019. doi: https://doi.org/10.1016/j.wace.2019.100200. 2212-0947. 1, 21

J. S. Shirolkar, C. F. M. Coimbra, and M. Queiroz McQuay. Fundamental aspects of modeling turbulent particle dispersion in dilute flows. *Progress in Energy and Combustion Science*, 22(4):363–399, 1996. doi: https://doi.org/10.1016/S0360-1285(96)00006-8. 0360-1285. 20, 27, 31, 33, 35, 38

M. Sommerfeld. Analysis of isothermal and evaporating turbulent sprays by phase-Doppler anemometry and numerical calculations. *International Journal of Heat and Fluid Flow*, 19(2):173–186, 1998. doi: https://doi.org/10.1016/S0142-727X(97)10022-4. 0142-727X. xvii, 31, 38

C. Son and T. Kim. Development of an icing simulation code for rotating wind turbines. *Journal of Wind Engineering and Industrial Aerodynamics*, 203:104239, 2020. doi: https://doi.org/10.1016/j.jweia.2020.104239. 0167-6105. 22

S. J. Stebbins, E. Loth, A. P. Broeren, and M. Potapczuk. Review of computational methods

for aerodynamic analysis of iced lifting surfaces. *Progress in Aerospace Sciences*, 111: 100583, 2019. doi: https://doi.org/10.1016/j.paerosci.2019.100583. 0376-0421. xiii, 11, 13, 14, 19

T. Strobl, S. Storm, and S. Ameduri. Synergic effects of passive and active ice protection systems. In A. Concilio, I. Dimino, L. Lecce, and R. Pecora, editors, *Morphing Wing Technologies*, chapter 26, pages 841–864. Butterworth-Heinemann, 2018. ISBN 978-0-08-100964-2. doi: https://doi.org/10.1016/B978-0-08-100964-2.00026-5. 16

M. Strub, O. Jabbour, F. Strub, and J. P. Bédécarrats. Experimental study and modelling of the crystallization of a water droplet. *International Journal of Refrigeration*, 26(1): 59–68, 2003. doi: https://doi.org/10.1016/S0140-7007(02)00021-X. 0140-7007. 21

S. Tabakova, F. Feuillebois, and S. Radev. Freezing of a suspended supercooled droplet with a heat transfer mixed condition on its outer surface. *AIP Conference Proceedings*, 1186 (1):240–247, 2009. doi: https://doi.org/10.1063/1.3265335. 21

F. X. Tanner. *Droplet freezing and solidification*, chapter 16, pages 327–338. Springer U.S., Boston, MA, 2011. ISBN 978-1-4419-7264-4. doi: https://doi.org/10.1007/978-1-4419-7264-4_16. 21, 45, 47

G. I. Taylor. Diffusion by continuous movements. *Proceedings of the London Mathematical Society*, s2-20(1):196–212, 1922. doi: https://doi.org/10.1112/plms/s2-20.1.196. 19

L. H. Thomas. *Elliptic problems in linear differential equations over a network*. Watson Sci. Comput. Lab Report, Columbia University, New York, 1949. 43

Y. S. Touloukian and D. P. DeWitt. *Thermophysical properties of matter*. Purdue University. Thermophysical Properties Research Center., 1970. 109

H. K. Versteeg and W. Malalasekera. *An Introduction to Computational Fluid Dynamics*. Pearson Education Limited, second edition, 2007. ISBN 978-0-13-127498-3. xiii, 41

J. Wallace and P. Hobbs. *Atmospheric Science - An Introductory Survey*. Academic Press, second edition, February 2006. ISBN 978-0-127-32951-2. doi: https://doi.org/10.1016/C2009-0-00034-8. 55

T. Wang, Y. Lü, L. Ai, Y. Zhou, and M. Chen. Dendritic growth model involving interface kinetics for supercooled water. *Langmuir*, 35(15):5162–5167, 2019. doi: https://doi.org/10.1021/acs.langmuir.9b00214. xiii, 49

S. Wanning, R. Süverkrüp, and A. Lamprecht. Pharmaceutical spray freeze drying. *International Journal of Pharmaceutics*, 488(1):136–153, 2015. doi: https://doi.org/10.

1016/j.ijpharm.2015.04.053. 0378-5173. 22

A. A. Yancheshme, A. Allahdini, K. Maghsoudi, R. Jafari, and G. Momen. Potential anti-icing applications of encapsulated phase change material–embedded coatings; a review. *Journal of Energy Storage*, 31:101638, 2020. doi: https://doi.org/10.1016/j.est.2020.101638. 2352-152X. 1

S.-C. Yao and V. E. Schrock. Heat and mass transfer from freely falling drops. *American Society of Mechanical Engineers*, 98(1):120–126, 1976. doi: https://doi.org/10.1115/1.3450453. xvii, 20, 50, 53, 59, 60, 61, 63, 64, 65, 66, 67, 68, 69, 70, 71, 72, 73, 74, 75, 76, 77, 78, 79, 80, 81, 82, 83, 87, 88, 89, 91

J. P. Zarling. Heat and mass transfer from freely falling drops at low temperatures. Technical Report 18, Cold Regions Research and Engineering Laboratory, Hanover, New Hampshire, USA, August 1980. 20

D. Zeppetelli and W. G. Habashi. In-flight icing risk management through Computational Fluid Dynamics - icing analysis. *Journal of Aircraft*, 49(2):611–621, 2012. doi: https://doi.org/10.2514/1.C031609. xiii, 2, 3

C. Zhang and H. Liu. Effect of drop size on the impact thermodynamics for supercooled large droplet in aircraft icing. *Physics of Fluids*, 28(6):062107, 2016. doi: https://doi.org/10.1063/1.4953411. 10, 19, 21

Appendix A

Physical properties interpolations

To obtain the numerical results presented in Chapters 5 and 6, distinct thermophysical properties of dry air and water (liquid and solid states) were necessary. These properties were obtained resorting to equations available in the literature and, when those equations did not exist, through interpolations from available data.

Several correlations were developed by McQuillan et al. [1984] to compute the thermodynamic and transport properties of dry air at atmospheric pressure for the temperature range between $200\,\mathrm{K}$ up to $400\,\mathrm{K}$ resorting to Beckett et al. [1955] for the specific mass and heat and using the studies performed by Touloukian and DeWitt [1970] for the thermal conductivity and dynamic viscosity. To obtain these correlations, a non-linear squares algorithm, which combines the Gauss method, also known as Taylor series, and the method of steepest descent, was used being possible to conclude that all correlations deviate by less than 0.15% from the tabulated values. Table A.1 summarizes the thermophysical properties for dry air at atmospheric pressure.

Table A.1: Thermophysical properties of dry air for a temperature range between $200\,\mathrm{K}$ and $400\,\mathrm{K}$ at 1 atm.

Physical Property	Expression
ρ_a	$\frac{351.99}{T_d} + \frac{344.84}{T_d^2}$
$c_{p,a}$	$1030.5 - 0.19975 \times T_d + 3.9734 \times 10^{-4} \times T_d^2$
μ_a	$\frac{1.4592 \times 10^{-6} \times T_d^{1.5}}{T_d + 109.10}$
λ_a	$\frac{2.3340 \times 10^{-3} \times T_d^{1.5}}{164.54 + T_d}$

For the liquid water, the thermophysical properties were obtained by resorting to a fourth degree polynomial interpolation considering a table of values obtained by Linstrom and Mallard. These interpolations are valid for the temperature range between $273.16\,\mathrm{K}$ up to $335.16\,\mathrm{K}$ at one atmosphere of pressure. The increment of temperature for each thermophysical property was $0.5\,\mathrm{K}$, to reduce the error associated with the interpolation methodology.

Relatively to ice, the thermophysical properties used are the same that were used by Hindmarsh et al. [2003]. Therefore, Table A.3 represents the thermophysical properties

of water in the solid state at atmospheric pressure.

Table A.2: Thermophysical properties of liquid water for a temperature range between $273.16\,\mathrm{K}$ and $335.16\,\mathrm{K}$ at 1 atm.

Physical Property	Expression
ρ_l	$-262.987 \times 10^{-9} \times T_d^4 + 346.724 \times 10^{-6} \times T_d^3 - 174.665 \times 10^{-3} \times T_d^2 + 39.312 \times T_d - 2.308 \times 10^3$
$c_{p,l}$	$7.102 \times 10^{-6} \times T_d^4 - 9.046 \times 10^{-3} \times T_d^3 + 4.329 \times T_d^2 - 922.290 \times T_d + 77.978 \times 10^{-3}$
μ_l	$85.400 \times 10^{-12} \times T_d^4 - 109.444 \times 10^{-9} \times T_d^3 + 52.733 \times 10^{-6} \times T_d^2 - 11.331 \times 10^{-3} \times T_d + 917.688 \times 10^{-3}$
λ_l	$1.119 \times 10^{-9} \times T_d^4 - 1.423 \times 10^{-6} \times T_d^3 + 667.769 \times 10^{-6} \times T_d^2 - 135.571 \times 10^{-3} \times T_d + 10.544$

Table A.3: Thermophysical properties of ice at 1 atm.

Physical Property	Expression
ρ_s	$-0.163 \times T_d + 961.4$
$c_{p,s}$	$7.178 \times T_d + 141$
L_{ph}	333×10^3
λ_s	$-0.011 \times T_d + 5.22$